



Department of AERONAUTICS and ASTRONAUTICS  
STANFORD UNIVERSITY

RALPH A. KUIPER

INTERFEROMETRIC STUDY OF THE  
NONEQUILIBRIUM SHOCK REFLECTION PROCESS  
AND THERMAL LAYER IN IONIZING ARGON

SUBMITTED BY D. BERSHADER

FACILITY FORM 602	N 68-37052	
	(ACCESSION NUMBER)	(THRU)
	144 (PAGES)	1 (CODE)
	CR-97252 (NASA CR OR TMX OR AD NUMBER)	25 (CATEGORY)

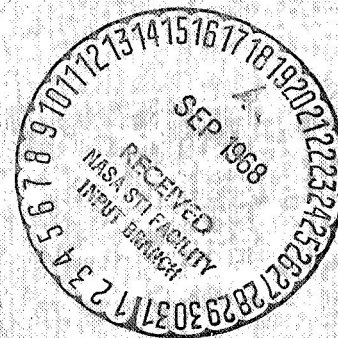
GPO PRICE \$ \_\_\_\_\_

CSFTI PRICE(S) \$ \_\_\_\_\_

Hard copy (HC) \_\_\_\_\_

Microfiche (MF) \_\_\_\_\_

ff 653 July 65



AUGUST  
1968

Supported by the  
National Aeronautics and Space Administration  
Grant NGR 05-020-091

SUDAAR  
NO. 353

Department of Aeronautics and Astronautics  
Stanford University  
Stanford, California

INTERFEROMETRIC STUDY OF THE NONEQUILIBRIUM  
SHOCK REFLECTION PROCESS AND THERMAL LAYER  
IN IONIZING ARGON

by

Ralph A. Kuiper

SUDAAR No. 353  
August 1968

This research was sponsored by the National Aeronautics and Space  
Administration under Research Grant NGR-05-020-091

## ABSTRACT

Two-wavelength, time resolved interferograms provide measurements of the time history of the thermodynamic properties behind the reflected shock wave in ionizing argon. The streak interferograms also provide an informative flow visualization of the shock reflection process including the nonequilibrium wave interactions resulting from the onset of ionization behind both the incident and reflected shocks. The experimentally determined equilibrium thermodynamic properties behind the reflected shock are found to be consistently greater than those predicted from the usual constant reflected shock speed theory. Argon ionization relaxation times obtained from the interferograms are correlated and compared with previous measurements over a range of shock speeds from 2.9 to 5.5 km/sec. The origin and nature of the observed nonequilibrium phenomena in the reflected shock structure are discussed in detail while the quantitative results provide the basis for experiments aimed at spatially resolving the ionized thermal layer formed on the shock-tube end-wall.

Density and electron concentration profiles are obtained in the ionized, end-wall boundary layer from two-wavelength snapshot interferograms. Upon comparison, it is found that the experimental electron concentrations remain considerably higher in the boundary layer than predicted by theory. The discrepancy is attributed primarily to nonequilibrium effects which are not accounted for in the theoretical treatment. From a comparison of theory and preliminary boundary layer experiments when no ionization is present, a value of  $\nu = .75$  for the temperature exponent is obtained when the thermal conductivity for neutral argon is assumed proportional to  $T^\nu$ .

## ACKNOWLEDGMENTS

The author expresses his appreciation to Professor Daniel Bershader for his guidance and support during the course of this investigation.

Gratitude is also extended to Dr. Russell Duff for arranging the loan from Lawrence Radiation Laboratory of the initial model of the proportional time delay unit which was used in most of these experiments.

The comments of Professors Donald Baganoff and I-Dee Chang who read the text are also appreciated.

The author is also grateful to Dr. Stellan Knöös for supplying his computer program for the ionized, boundary-layer calculations.

This research was supported by the National Aeronautics and Space Administration Grant NGR-05-020-091.



## TABLE OF CONTENTS

	<u>Page</u>
ACKNOWLEDGMENTS . . . . .	iii
TABLE OF CONTENTS . . . . .	iv
LIST OF ILLUSTRATIONS . . . . .	v
NOMENCLATURE . . . . .	viii
I. INTRODUCTION . . . . .	1
II. EXPERIMENTAL EQUIPMENT AND TECHNIQUES . . . . .	8
2.1 Shock Tube Facility and Instrumentation . . . . .	8
2.2 Associated Electronic Equipment . . . . .	12
2.3 Associated Optical Equipment . . . . .	14
2.4 Interferometric Measurements in Ionized Gases . . . . .	18
2.5 Thermal Boundary Layer Technique . . . . .	20
2.6 Shock Reflection Study . . . . .	21
III. END-WALL BOUNDARY LAYER WITHOUT IONIZATION . . . . .	24
3.1 Theoretical Calculations . . . . .	24
3.2 Experimental Results . . . . .	27
3.3 Sources of Error . . . . .	31
IV. THE SHOCK REFLECTION PROCESS IN IONIZING ARGON . . . . .	36
4.1 Description of the Reflection Process . . . . .	37
4.2 Comparison with Other Gases . . . . .	58
4.3 Time History of Thermodynamic Properties . . . . .	61
4.3.1 Approach to Ionization Equilibrium . . . . .	62
4.3.2 Thermodynamic Properties . . . . .	67
V. IONIZED BOUNDARY LAYER RESULTS . . . . .	90
5.1 Theoretical . . . . .	90
5.2 Experimental Results . . . . .	95
5.3 Discussion of Results . . . . .	103
VI. SUMMARY AND CONCLUSION . . . . .	108
REFERENCES . . . . .	111
APPENDIX A. EFFECT OF REFRACTION AND WINDOW BOUNDARY LAYER ON INTERFEROMETRIC MEASUREMENTS . . . . .	114
APPENDIX B. CALCULATION OF REFLECTED SHOCK EQUILIB- RIUM PROPERTIES . . . . .	128

## LIST OF ILLUSTRATIONS

<u>Figure</u>	<u>Page</u>
1. Comparison of incident shock speed measurement from streak interferograms with side wall measurements . . . . .	13
2. Schematic of experimental apparatus . . . . .	15
3. Photographs of test equipment and optical apparatus . . . . .	16
4. Flow and no-flow un-ionized boundary layer interferograms of run 714 for two wavelengths . . . . .	29
5. Comparison of experimental temperature profile with theory for un-ionized boundary layer . . . . .	30
6. Un-ionized boundary layer profile from reference 10 . . . . .	34
7. Streak interferogram and x-t diagram of shock reflection process with no ionization (argon) . . . . .	38
8. Streak interferogram and x-t diagram of shock reflection process with ionization behind reflected shock (argon) . . . . .	40
9. Comparison of expansion wave front speed with acoustic speed in region 5F (argon) . . . . .	43
10. Snapshot interferogram showing expansion wave behind the reflected shock (argon) . . . . .	44
11. Comparison of measured reflected speed $U_{F5E}$ with "quasi-steady" theory (argon) . . . . .	46
12. Regular and infinite fringe streak interferogram of reflection process with ionization behind incident shock (argon) . . . . .	49
13. Distance vs. time (x-t) diagram of shock reflection process with ionization behind incident shock ( $M = 12.7$ , $P_1 = 5$ torr, argon) . . . . .	50
14. Oscillogram of pressure history measurement on shock tube end-wall for ionizing argon . . . . .	53
15. Snapshot interferogram showing reflected shock bifurcation in ionized argon . . . . .	55
16. Schematic diagram illustrating onset and propagation of reflected shock bifurcation (argon). . . . .	57
17. A series of streak interferograms in argon for $P_1 = 2$ torr and increasing Mach number . . . . .	59

<u>Figure</u>		<u>Page</u>
18.	Streak interferograms of the shock reflection process in a) xenon, b) nitrogen, and c) carbon dioxide . . . . .	60
19.	Ionization-relaxation particle times behind incident and reflected shocks in argon . . . . .	64
20.	Ionization-relaxation laboratory times behind incident and reflected shocks in argon . . . . .	68
21.	Streak interferograms of shock reflection process extending to 100 microseconds after reflection (argon). . . . .	69
22.	Measured and theoretical fringe shifts from initial conditions to frozen reflected shock conditions . . . . .	71
23.	Measured fringe shifts from initial conditions to reflected shock equilibrium conditions. . . . .	72
24.	Measured fringe shifts from initial conditions to reflected shock conditions at 100 microseconds after reflection . . . .	73
25.	Measured electron concentrations in the frozen reflected shock region 5F (argon) . . . . .	75
26.	Comparison of measured and theoretical frozen reflected shock speed $U_{5F}$ (argon) . . . . .	76
27.	Reflected shock mass densities at equilibrium in region 5E. .	77
28.	Reflected shock electron concentrations at equilibrium in region 5E . . . . .	78
29.	Reflected shock pressures at equilibrium in region 5E . . .	80
30.	Reflected shock temperatures at equilibrium in region 5E .	81
31.	Reflected shock densities at 100 microseconds after reflection . . . . .	85
32.	Reflected shock electron concentrations at 100 microseconds after reflection. . . . .	86
33.	Reflected shock pressures at 100 microseconds after reflection . . . . .	87
34.	Reflected shock temperatures at 100 microseconds after reflection . . . . .	88
35.	Time history of argon thermodynamic properties in re- flected shock region . . . . .	89
36.	Snapshot interferograms of ionized end-wall boundary layer in argon . . . . .	96

<u>Figure</u>		<u>Page</u>
37.	Measured fringe shifts at two wavelengths in ionized argon boundary layer . . . . .	98
38.	End-wall boundary layer profile of density and electron concentration in ionized argon . . . . .	100
39.	End-wall boundary layer profile of density and electron concentration in ionized argon . . . . .	101
40.	End-wall boundary layer profile of density and electron concentration in ionized argon . . . . .	102
41.	Theoretical fringe shift error in end-wall boundary layer measurements . . . . .	124
42.	Equilibrium reflected shock temperature ratios from "quasi-steady" theory using various corrections to ionization potential (argon) . . . . .	133
43.	Equilibrium reflected shock electron concentrations from "quasi-steady" theory using various corrections to ionization potential (argon) . . . . .	134

## NOMENCLATURE

$A(\lambda)$	Coefficient in refractivity expression (Eqn. 2.4)
$B(\lambda)$	Coefficient in refractivity expression (Eqn. 2.4)
$D$	Diffusion coefficient
$E_1$	First excited state of neutral atom
$H$	Nondimensional enthalpy ratio
$I$	Ionization potential
$K$	Thermal conductivity
$L$	Test section width, focal length ( ) <sub>f</sub>
$M_s$	Mach number of incident shock
MZI	Mach Zehnder Interferometer
$N$	Order of interference
$R$	Argon gas constant
$S$	Fringe shift
$T$	Gas temperature
$U$	Shock speed
$V_w$	Camera writing speed
$a$	Speed of sound
$c$	Speed of light in vacuum
$e$	Electronic charge, internal energy
$h$	Debye length, enthalpy
$k$	Boltzmann constant
$m$	Particle mass
$n$	Number density or concentration
$p$	Gas pressure
$t$	Time after shock reflection, window thickness
$x, y$	Distance from shock-tube end-wall

## GREEK SYMBOLS

$\alpha$	Degree of ionization
----------	----------------------

$\gamma$	Ratio of specific heats
$\epsilon_0$	Vacuum permittivity
$\eta$	Similarity variable, density ratio across incident shock
$\theta$	Nondimensional temperature ratio
$\lambda$	Wavelength of light, mean free path
$\mu$	Index of refraction
$\nu$	Temperature exponent for thermal conductivity
$\rho$	Gas density
$\tau$	Ionization relaxation time
$\psi$	Optical path length
$\zeta$	Ratio of reflected shock density to initial density

#### SUBSCRIPTS

1	Initial shock tube conditions
2	Conditions behind incident shock wave
3,5	Conditions behind reflected shock wave
A	Argon atom
E	Equilibrium
F	Frozen
L	Laboratory reference frame
S	Incident shock
e	Electron
w	Wall conditions
$\infty$	Edge of boundary layer



# I

## INTRODUCTION

A considerable amount of theoretical work has been done on the prediction of heat transfer and variation of transport and thermodynamic properties through ionized boundary layers. These theoretical efforts have not always adequately accounted for the coupling between the boundary layer structure and the thermodynamic and fluid dynamic variations of the "free stream." Unfortunately, the same may often be said of the empirical work that has been reported on this subject. Accordingly, the boundary layer investigation presented here is concerned with experimentally determining the structure and properties of the flow field external to the boundary layer as well as the detailed structure of the boundary layer itself. This work is part of what has been a continuing effort in the Stanford Aerophysics Laboratory to investigate the transport properties of high temperature ionized gases -- in this case, the thermal conductivity of an argon plasma.

In the present experiments, two-wavelength interferometry is applied to the problem of spatially resolving the distribution of thermodynamic properties in an ionized argon thermal boundary layer. The thermal layer considered in these experiments is the thin transition region ( $\sim 2\text{mm}$ ) between a cold wall and an adjacent high temperature ( $\sim 10^4\text{K}$ ), high pressure ( $\sim 1\text{atm}$ ) plasma ( $\alpha \sim .1$ ). This situation is produced in a conventional combustion driven shock tube when an incident strong shock wave undergoes reflection from the end-plate of the closed test section. Because the test gas or plasma between the wall and the reflected shock wave is essentially stagnant because of the constraining influence of the end-wall, there are no fluid shear stresses acting in

the boundary layer development. It would thus appear that the boundary layer measurements could be compared with a less complex theory than that for a flat plate parallel to an ionized stream. However, in ionizing monatomic gases as well as in chemically and vibrationally relaxing gases, the shock reflection process itself is considerably more complex than implied above. It may then be asked to what extent these complications couple with the experimental and theoretical boundary layer analyses.

In an attempt to answer this rather broad question, two-wavelength, time-resolved interferometry was applied to investigate the shock reflection process and the history of the thermodynamic state of the gas in the reflected shock region. These results represent a major portion of this report because of their possible influence on boundary layer structure and heat transfer, radiation, and chemical and electronic reaction rate studies in the reflected shock region, studies which have been and still are underway in many laboratories. The need for experimental determination of the state of the doubly shocked, end-wall gas has already been indicated in the work of Camac and Feinberg<sup>(1)</sup>, Smith<sup>(2)</sup>, and Baganoff<sup>(3)</sup> in connection with studies involving the reflected shock structure, i. e., on the transitional processes from the initial to final equilibrium states.

For what may be termed relatively mild conditions ( $M < 7$ ,  $P_1 \leq 10$  torr), the shock reflection process in argon is straightforward, and the thermodynamic properties behind the reflected shock computed from simple, one dimensional theory for constant specific heats may be assumed to prevail for times exceeding 300 microseconds after reflection. However, for incident shock speeds and initial pressures high enough to yield significant ionization, the thermodynamics and fluid dynamics of the reflection process are severely complicated by non-equilibrium wave interactions. The observed interactions result from the

reflection of the incident shock into its own relaxation region and from the suddenness of the thermodynamic changes associated with ionization equilibrium behind both the incident and reflected shocks. The abruptness of these changes is characteristic of the rare gases.<sup>(4, 5, 6)</sup> The streak interferograms obtained in this study show these interactions clearly and yield quantitative data on the electron and heavy particle number densities in the reflected region. That information may then be related to the pressure and temperature by assuming an equation of state for the ionized gas.

At this point, a brief description of the reflection process in ionizing argon and some of the preceding work in this area may assist in introducing the details which are discussed below. When the incident shock wave passes through the initially stationary gas, the translational degrees of freedom of the argon atoms are fully excited after only a few collisions, and the gas is set into a uniform motion in the direction of shock propagation. The velocity and density of the gas immediately behind the shock are the so called "frozen" values calculated from the shock jump conditions and the caloric and thermal equations of state for an ideal gas with constant specific heats. The shocked gas remains close to these frozen conditions for some time after shock passage; however, due to their statistical imbalance with the translational degrees of freedom, the internal degrees of freedom gradually become excited until enough electrons and excited atoms have been produced to cause a cascading of the ionization process. A relaxation time  $\tau_{2L}$  may then be defined to characterize this approach to equilibrium where the subscript 2L refers to conditions behind the incident shock observed from a stationary laboratory position. The interferograms of Wong and Bershader<sup>(5)</sup> for argon illustrate clearly the sharp character of the changes near the onset of equilibrium behind the incident shock. A contrasting case is

that of vibrationally relaxing gases where equilibration is much more continuous in nature. (See for example the interferograms of ref. 7 behind the incident shock and refs. 8 and 9 behind the reflected shock.) When the frozen translational shock reflects from the end-wall, the properties of the gas in the reflected shock region are again initially determinable from the conservation equations for a nonreacting gas. It will be shown later, however, that immediately behind the frozen shock, there are a measureable number of electrons present so the term "frozen" is not strictly applicable. In any case, a phenomenon similar to that occurring behind the incident shock takes place, and after a relaxation time  $\tau_5$ , the gas achieves ionization equilibrium rather suddenly. Because the pressure is so much higher, however,  $\tau_5$  is considerably less than  $\tau_{2L}$ . A reflected ionization front propagates away from the end-wall at a speed which is slightly less than the reflected translational shock speed.

The reflected ionization front effectively reduces the gas temperature by a factor as high as 3 (in these experiments); this is primarily due to the absorption of translational internal energy by the ionization process. As a result, the density increases considerably, and in order to support this density increase, an expansion wave system originating at the point of equilibration next to the wall propagates at the acoustic speed into the initially quiescent gas between the wall and translational shock. The front of this expansion wave then overtakes and decelerates the reflected shock. An additional decrease in the reflected shock speed results from the density increase associated with the equilibration in region 2.

The results of Wong and Bershader<sup>(5)</sup> behind the incident shock show that approximately 80% of the change in density and pressure from the frozen

to the equilibrium values takes place within the last 20% of the total relaxation time. In accordance with analagous shock-shock interactions, this steep density gradient is transmitted through the reflected shock and toward the wall while the reflected shock itself is transmitted through the density gradient into the equilibrium region behind the incident shock. Upon reaching the wall where it is seen as a pressure increase, the interaction wave is forced to reflect because of the velocity constraint, and it eventually rejoins and coalesces with the transmitted reflected shock. The coalesced wave continues to move away from the wall at an approximately constant speed. A considerable number of details of the reflection process have not been included here since the intention has been merely to introduce its complexity and some of the terminology which will be used in the later discussion.

Camac and Feinberg<sup>(1)</sup> and Smith<sup>(2)</sup> considered the reflection process in ionizing argon and xenon respectively on the basis of heat transfer and pressure measurements on the shock tube end-wall. Because of this, they were limited to observation of phenomena which occurred at or propagated to the wall. Despite this, however, Camac and Feinberg accurately predicted the presence of an expansion wave emanating from the first equilibrium point ( $\tau_5$ ) at the wall. Their hypothesis that an additional shock should occur between the wall and reflected ionization front has not been verified, at least for the conditions encountered in the present experiments. Although the xenon, end-wall, pressure measurements of Smith did not appear to corroborate the expansion wave hypothesis, they did suggest that the ionization process acts as a heat sink to slow the reflected wave. This would reasonably explain why in the stronger shock cases of this study in argon the expansion wave is "washed out" and the shock decelerates noticeably immediately after reflection. Several experiments in

xenon were also made in this investigation and the pertinent points of comparison will be discussed in chapter IV.

A point of interest to the present studies is that Camac and Feinberg's heat-transfer measurements showed no change when the reflected shock gas attained equilibrium. However, a significant increase in signal was observed when the interaction wave arrived at the wall. This would in some measure support the belief that if boundary layer measurements can be made at conditions and times  $t$  after reflection such that  $\tau_5 \ll t \leq \tau_{2L}$ , then the effect of the finite time to achieve an ionized "free stream" could be neglected in the theoretical boundary layer development. The ionized boundary layer measurements reported here were made with this thought in mind. Experimentally, the properties at the edge of the boundary layer, or "free stream" were measured, and the resulting experimental profiles (all at  $t = 100 \mu\text{sec.}$ ) are assumed independent of the starting process.

The interferometric technique used here to resolve the ionized boundary layer is similar to that used by Bunting<sup>(10)</sup> for low temperature or un-ionized boundary layers. In order to "calibrate" the present measurements and, in effect, reevaluate the approach, several experiments were conducted at low temperatures with modifications in the experimental apparatus. A description of the techniques and the present results are given in Chapter III. The temperature dependence of the argon thermal conductivity  $K_A$  found here agrees quite well with the semi-theoretical results of Amdur and Mason<sup>(11)</sup> who found that  $K_A \propto T^{.75}$ . The boundary layer profiles for the ionized freestream are presented in Chapter V where they are compared with the theoretical predictions of Kn88s.<sup>(12)</sup> Significant discrepancies are found between the theoretical and



experimental electron concentration profiles, and the possible sources of these discrepancies are discussed.

Most of the experimental apparatus and techniques are described in Chapter II, in order to assist in clarifying the subject matter that follows and to discuss some of the experimental problems which might otherwise tend to confuse the reader. Two appendices are included to present the analyses used to determine the effect of refractive errors on the experimental boundary layer profiles and the theoretical reflected shock properties. In the latter case, a comparison is made of several approaches which could be used to account for electro-static effects on the lowering of the ionization potential and truncation of the partition functions. Because of its internal consistency and the satisfying of certain restrictive conditions, the Debye-Hückel theory is applied in conjunction with the modified Saha equation to compare theory and experiment and to determine the equilibrium pressures and temperatures from the measured electron concentrations and mass densities.

## II

### EXPERIMENTAL EQUIPMENT AND TECHNIQUES

Shock tubes provide a relatively inexpensive and simple means of producing high enthalpy gases which may be used in heat transfer and gaskinetic studies. They are particularly useful in reaction rate studies because the resulting incident shock wave raises the temperature and density of the initially quiescent gas by factors of the order  $(\gamma - 1)M^2/2$  and  $(\gamma + 1)/(\gamma - 1)$  in time intervals that are on the order of one-tenth of the corresponding relaxation times for vibrational or chemical equilibration. Even more severe conditions may be attained for similar studies by allowing the initially produced shock wave to reflect from the closed end of the shock tube, thereby heating the gas twice. As already mentioned, this was the manner in which the shock tube was applied to produce the high temperature plasmas of interest in this investigation. This chapter presents a description of the equipment and experimental techniques used in the present study; however, no attempt will be made to provide the theoretical basis of shock tube operation since many references already exist on this subject.<sup>(13, 14)</sup> The optical methods are also treated briefly, and only the equations necessary to understand the interferograms and data reduction are presented.

2.1 Shock Tube Facility and Instrumentation. The Stanford Aerophysics shock tube used in the present investigation is a square cross-section, extruded aluminum tube that is 6.7 meters long from the diaphragm section to the end-plate and has a test section width of  $L = 5\text{cm}$ . The square cross-section is particularly convenient for interferometric studies since the data can then be reduced on the basis of a one-dimensional analysis. The driver section is

stainless steel with a 7.6cm I.D. and 3.8cm walls and can be operated as a pressure drive or combustion drive (spark plug ignition) with a 70% helium diluted  $H_2 - O_2$  stoichiometric mixture.

Half-hard aluminum sheet (2024-T3) .032 inches thick and machine scribed on the driven side was used for diaphragm material between the driver and test section. Bursting is then caused by the high pressure in the driver. By using this material, rather than a softer aluminum, and by carefully scribing the diaphragms, pitting of the quartz test section windows from aluminum deposition was considerably reduced. The "life time" of the relatively expensive quartz windows was further extended by removing the aluminum deposits with potassium hydroxide solution. Less expensive glass windows were completely unsatisfactory since they tended to develop "flakey" surfaces at the strong shock conditions.

Schlieren grade quartz windows approximately 2 3/4 inches in diameter and 3/4 inch thick were mounted in stainless steel holders providing a field of view approximately 2 1/4 inches in diameter. The end wall, made from a solid brass plug, then formed a chord of approximately 1 inch in the field of view. Windows closely matching those in the test section were used in the compensating leg of the MZI. In performing the boundary layer experiments, it is very important that the vertical fringes formed by the MZI be uniformly spaced. To insure this, the windows were iteratively rotated to compensate for wedge effects until broad horizontal fringes were straight and parallel at all points in the field of view.

Two 1/16 inch I.D. brass tubes 5cm long were mounted in holes drilled horizontally through the brass plug parallel to the end-wall surface. Before inserting these tubes in the holes, they were fitted with internal cross wires

(.004 inch D.) located so that they would be at  $2/3$  the distance across the test section width from the light-inlet window. . The actual distance between the cross wires and end-wall surface was then measured with an optical comparator to an accuracy of .0025mm. Knowing this distance and the photographic magnification allows one to determine accurately the location of the end-wall relative to the fringes in the boundary-layer, snapshot interferograms.

The initial test section conditions are very important in shock tube studies involving nonequilibrium chemistry because the approach to equilibrium as well as the equilibrium properties are dependent on these conditions and are not simply functions of the ratio of frozen specific heats and Mach number. The impurity level in the test gas is also of concern since it has been shown in reference 4 that impurities can significantly affect the equilibration rates behind the incident shock. In the optical studies reported here, the initial pressure also provides the reference level for the measured density change so that errors in  $P_1$  are directly reflected in errors in the measured properties behind the reflected shock.

These remarks assume added significance when it is noted that, for reasons described below, it was necessary to take streak interferograms for each of two wavelengths on separate runs and cross plot the results. Furthermore, because of the attendant water vapor left in the tube after combustion driven test runs, the level of impurities could be quite large and, equally important, nonuniform from run to run. To improve this situation, the shock tube was cleaned after every run and evacuated to less than 1 micron hg (CVC Pirani Vac. Gauge) before filling with argon for the next run. The ensuing pressure rise before filling, , primarily due to outgassing, was .2 to .4 micron/minute which for five minutes between filling and firing resulted in impurity levels of

approximately two to three micron hg partial pressure. It should be noted that Pirani gauges are sensitive to the type of gas; in particular, the gauge is less sensitive to higher molecular weight impurities such as cleaning solvents. The above figures are therefore somewhat questionable. The actual argon gas used in the experiments was .99995 Linde reagent grade argon. For the low Mach number boundary layer tests and the time resolved shots in xenon, the tube was pressure driven and evacuated to  $10^{-5}$  Torr (CEC Ionization Gauge) for each shot with a measured leak rate of less than .1 micron/minute.

The initial pressures of 2, 5, and 10 Torr were measured on a Wallace and Tiernan 0-20 Torr pressure gauge. The gauge was checked against two different McLeod gauges with no measureable differences noted and was rechecked at several intervals in the experimental program. The excellent repeatability of the calibration curves even at the low end of the scale and the very slight scatter in measured fringe shifts across the incident shock leads to an assumed uncertainty in initial pressure of less than .04 Torr. The initial temperatures were obtained from room temperature measurements and were probably accurate to  $1^{\circ}\text{C}$ .

The test section has three shock detector transducer mounts located at equal intervals of 125 mm, the last one being 135 mm from the end wall. The first shock detector is used to trigger an oscilloscope which displays the output of the second and third. The shock speed is thus measured from the known distance and measured time. The uncertainty in the shock speed measurement is approximately 1.5% .

For the weaker shocks ( $M < 9$ ) the output, on the order of several millivolts, from platinum thin film heat gauge shock detectors was amplified

(gain $\sim$ 800) and fed to a dual beam oscilloscope. For the stronger shocks, barium titanate piezo-electric pressure transducers (sensitivity .45 mv/torr) were used as shock detectors. The outputs which were typically fractions of a volt were amplified (gain $\sim$ 40) to supply adequate triggering voltages.

In these experiments, the streak interferograms also provided a measure of the shock speed. By knowing the writing speed and magnification, the slope of the trajectory of the incident shock wave could be measured to give the shock speed. The accuracy of this technique was estimated to be the same as for the side wall transducers, and excellent agreement was found between the two methods as shown in Figure 1.

2.2 Associated Electronic Equipment. The oscillogram shock speed measurements just described were taken on a Type 555 dual beam Tektronix oscilloscope. Another Tektronix scope, Type 551, was used to measure the times relative to shock position at which the light source was actually triggered. The time bases for these scopes was calibrated with a Tektronix type 180-A Time Mark Generator.

A transistorized Proportional Time Delay unit built from a design provided by the Livermore Electronic Design Department\* proved to be an invaluable tool for performing these experiments. The unit provides a reliable and simple to operate method of timing or triggering other instrumentation when the shock wave is at a desired location. The signals from two shock detectors separated by a distance  $x$  provide the two input triggers for the unit, which in turn provides an output voltage pulse at some preadjusted fraction of the time  $x/U_s$ . For a constant shock speed this fraction reduces to the ratio of the distance between the second detector and desired shock position to

---

\*Lawrence Radiation Laboratory, Livermore, California. Courtesy of Dr. Russell Duff.



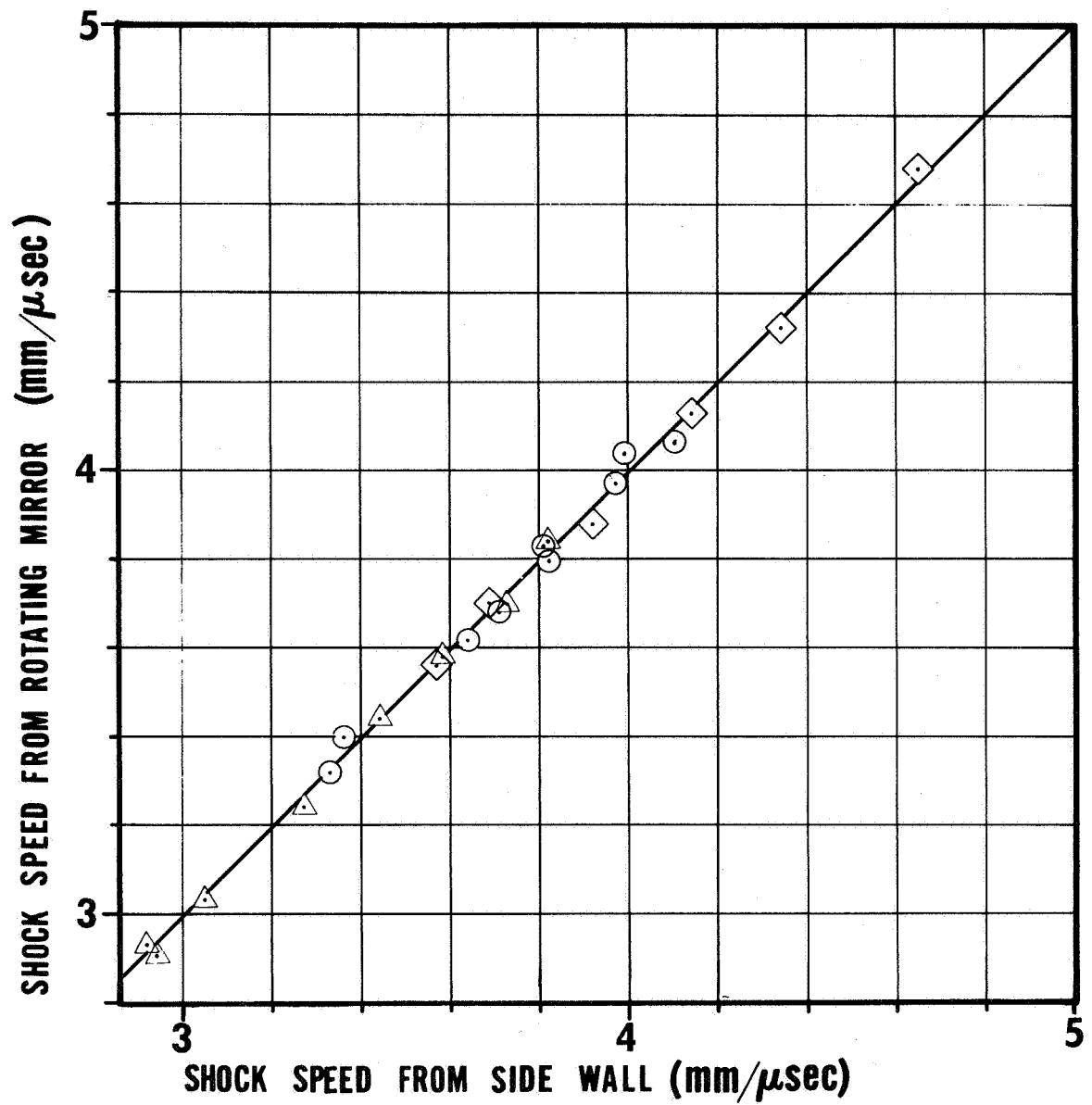


Figure 1. Comparison of incident shock speed measurement from streak interferograms with side wall measurements.

the distance between the first and second detector. The output signal, for example, was then used to provide a time zero reference for the boundary layer tests corresponding to shock incidence at the end wall. An Abtronics Model 200 two channel time delay unit was triggered with the proportional delay unit to provide the necessary triggering voltage and additional delay for the light source. Figure 2 is a block diagram of all the electronic triggering equipment and sequencing. The location of the optical equipment discussed in the next section is also shown in the figure.

2.3 Associated Optical Equipment. In addition to the shock tube, the basic diagnostic tool used in these experiments is a Mach-Zehnder interferometer. The theory and operation of interferometers is described in many references of which 15, 16, and 17 are a few. Only the points necessary for an understanding of the present measurements will be discussed here. The MZI in the Stanford Aerophysics Laboratory is of standard rectangular design and can be adjusted in what is commonly called the Kinder system wherein the fringe spacing and orientation may be changed without affecting the fringe focus. Figure 3 is a photograph showing the interferometer in its operating position along with the light source and other optical equipment.

Although standard mercury and tungsten lamps are used for adjusting the MZI, the actual test conditions are recorded with an exploding wire light source. A 2 mil half inch tungsten wire was enclosed in a housing for which a .015 x .25 inch vertical slit was the only outlet. A 7.5 uf capacitor charged to 20 kv was discharged through the wire when a sealed spark gap switch was broken down by a 15 kv pulse from a trigger unit. This trigger unit was initiated by a 50 volt pulse from the two-channel time delay unit. From photo multiplier

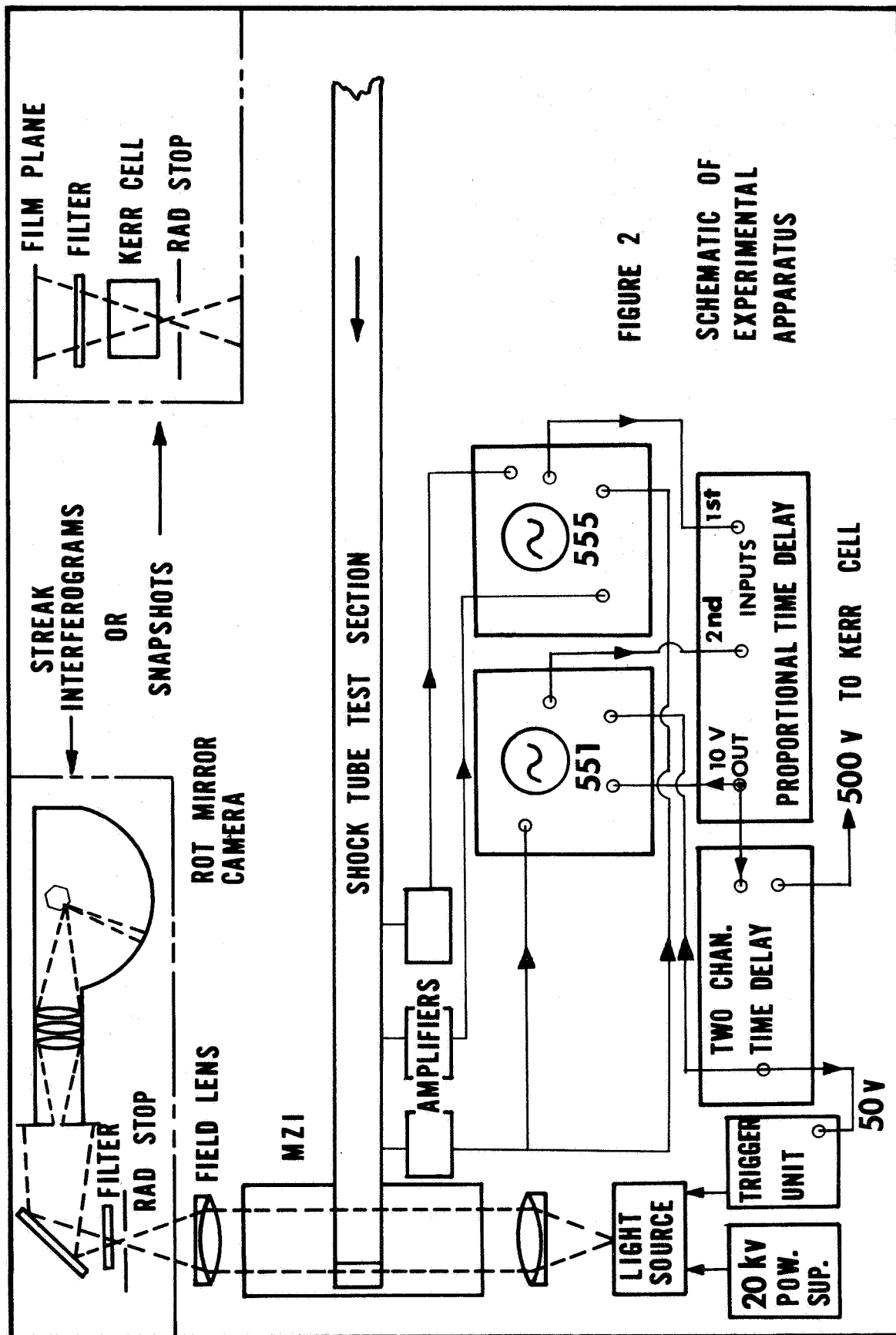
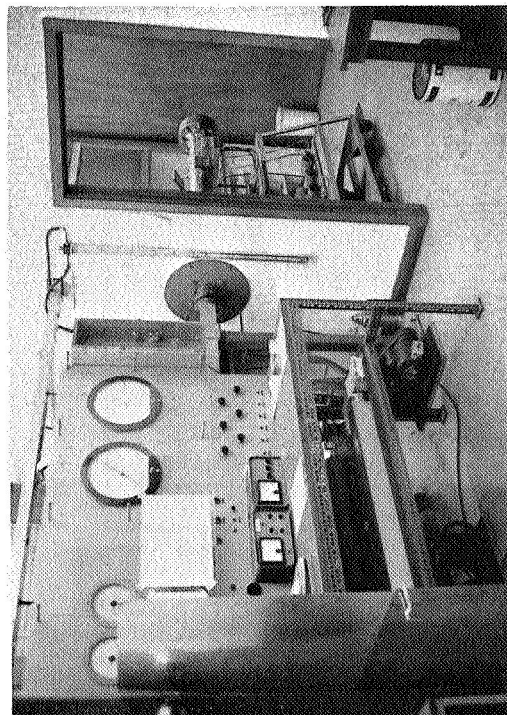
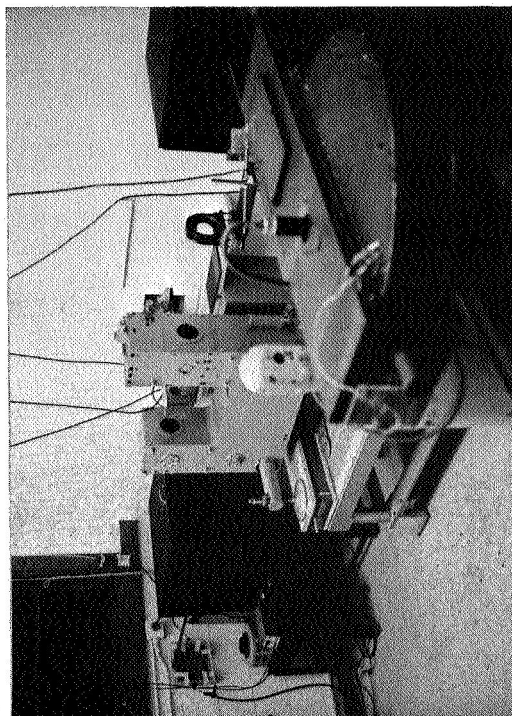


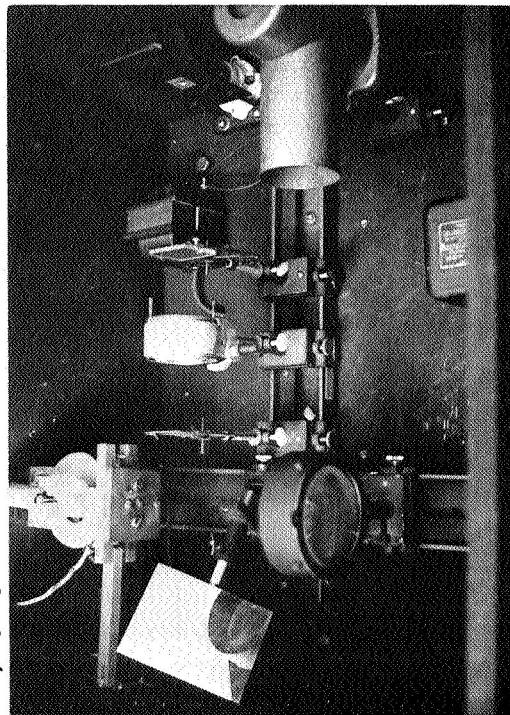
FIGURE 2  
SCHEMATIC OF  
EXPERIMENTAL  
APPARATUS



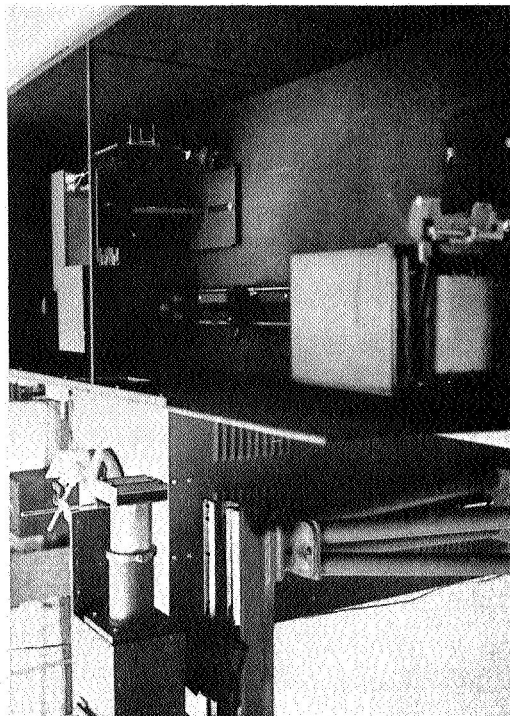
**a) SHOCK TUBE AND CONTROL PANEL**



**b) INTERFEROMETER AND TEST LAYOUT**



**c) LIGHT SOURCES**



**d) CAMERA SYSTEM**

**Figure 3.** Photographs of test equipment and optical apparatus.

measurements, it was determined that the light intensity emitted through the slit reached a peak in  $2.0 \mu$ -sec and had a brightness temperature of approximately  $40,000^\circ\text{K}$ . The intensity remained high enough to adequately expose the streak interferograms for over  $50 \mu$  sec. Attempts to increase the intensity by flowing argon through the wire cavity met with little success. The light source collimating lens was a four inch diameter cemented doublet achromat with a ten inch focal length. It is noted that achromatic lenses are used throughout because of the requirement for simultaneous focusing at two widely separated wavelengths.

The boundary layer snapshots were recorded on Polaroid-3000 4 x 5 prints, with a  $2 \mu$ -sec Kerr-cell shutter providing the time resolution. A single achromatic field lens ( $d = 5 \text{ in.}$ ,  $L_f = 24 \text{ in.}$ ) was also used as a camera lens with a radiation stop near its focal point. The two wavelengths were provided by a  $4530 \text{ \AA}$  ( $90 \text{ \AA}$  width, 53% peak) interference filter and a  $5720 \text{ \AA}$  ( $200 \text{ \AA}$ , width, 70% peak) laminated broad band pass combination filter. The necessity for the broad band width of the long wavelength filter is dictated by the low light source intensity at the longer wavelength. For the rotating mirror records, a  $4500 \text{ \AA}$  ( $100 \text{ \AA}$  width, 50% peak) interference filter was used in place of the  $4530 \text{ \AA}$  filter. A high degree of confidence in the wavelength values just given was established by transmission measurements, by observing the proportionality of fringe width to wavelength, and by further observing that the measured fringe shifts across the incident shock agreed very well with the theoretical values. It is certainly possible that a combination of errors could have produced this last result; however, it is not very likely. These points are mentioned because an accurate determination of the effective wavelengths is critical to interferogram evaluation.

The streak interferograms are obtained with a rotating mirror camera which sweeps its unmagnified slit image along a stationary two foot length of film (Kodak 2475 Recording Film 1600 ASA). The camera's hexagonal polished steel mirror (faces flat to 1/2 wave length) is driven by a gas turbine at speeds slightly over 700 rps as measured on a calibrated Berkeley EPUT counter. The writing speed, which was found to be invariant with position on the film plane, was calibrated versus rps by using a photomultiplier to measure the traversal time of the slit image leading edge across a known distance in the film plane. The deviation of the calibration points about a straight line fit extrapolated through zero was less than .01mm/ $\mu$  sec for a slit width of .75 mm and writing speeds of about 2.70 mm/ $\mu$  sec used in these experiments. The uncertainty in slope of the shock trajectory on the film records was taken as .5 and 1 degree respectively for incident and reflected shocks. This gave shock speed uncertainties of approximately 1.3 and 2.5% .

2.4 Interferometric Measurements In Ionized Gases. When no disturbance is present in the test section beam of the adjusted interferometer, a uniformly spaced fringe pattern results. The order of interference or fringe number at the point x,y(z along optical axis) on the image plane is given by

$$N(x,y) = \frac{1}{\lambda} [\psi_1 - \psi_2] \quad (2.1)$$

Here,  $\psi_1$  and  $\psi_2$  are respectively the optical path lengths from the source to the image plane through the test beam and compensating beam and are defined by

$$\psi = \int \mu ds \quad (2.2)$$

where  $\mu$  is the phase index of refraction and  $ds$  the elemental geometric



path length along a ray trajectory.

If a disturbance in refractivity  $(\mu-1)$  takes place in the test beam of the interferometer, the fringe number at the point  $x, y$  of the image plane will have some value different from the undisturbed value given above. If optical imperfections and refractivity gradients are neglected, all contributions to  $\Delta N(x, y)$  except those in the test section cancel and the change in order of interference at  $(x, y)$ , or the "fringe shift", is given simply by

$$S(x, y) = \frac{L}{\lambda} \Delta(\mu-1) \quad (2.3)$$

where  $L$  is the test section width and  $\Delta(\mu-1)$  is the change in refractivity in the test section from some reference condition. The application of this equation to plasma diagnostics arises from the highly dispersive nature of the electron refractivity which to a very good approximation depends on wavelength squared.

For a weakly interacting mixture of gases, the refractivity is given by the sum of the individual refractivities over all species. This assumption can be shown to be true for most plasmas, excluding stellar interiors.<sup>(18)</sup> For a singly ionized argon plasma and assuming charge neutrality, one can write for the refractivity<sup>(5)</sup> (in MKS Units)

$$\begin{aligned} (\mu-1) &= \frac{(\mu_A-1)_0}{\rho_0} \left[ \rho - n_e m_A \left( 1 - \frac{a^+}{a^0} + \frac{1}{m_e a^0} \left( \frac{e^2 \lambda^2}{\epsilon_0 16 \pi^3 c^2} \right) \right) \right] \\ &= A(\lambda) [\rho - n_e B(\lambda)] \end{aligned} \quad (2.4)$$

where  $a^+/a^0$ , the ratio of ion to neutral polarizabilities, is .67<sup>(18)</sup> and  $a^0$  and  $(\mu_A-1)_0$  are weak functions of wavelength and are related by  $(\mu_A-1)_0 = 2\pi a^0 \rho_0$ . It is readily apparent that if one can measure the change in the order of interferences,  $S$ , for each of two wavelengths at a position  $(x, y)$  in the flow field relative to what it would be for the uniform initial conditions, then

there would result two algebraic equations for the two unknowns  $\rho$  and  $n_e$ .

The question of the extent of refraction of light rays or wave fronts due to density, or refractivity, gradients in the test section and the resulting effect on the measured fringe shift is considered separately in Appendix A. This phenomena is particularly important in the experimental resolution of the end-wall thermal layer.

2.5 Thermal Boundary Layer Technique. The boundary layer experiments are performed by taking magnified snapshot interferograms with very narrow fringes, approximately five per mm, adjacent and parallel to the end wall. This orientation and spacing provides the optimum spatial resolution of the boundary layer when the interferometer is adjusted so that the fringes move away from the wall for an increase in density or refractivity. In these experiments, the field of view is split in half by the two optical filters to simultaneously obtain fringe shifts at two wavelengths (4530 Å and 5720 Å). As implied in the previous section, the fringe shifts are measured relative to the uniform conditions outside the boundary layer where the fringes are uniformly spaced. In practice, this is accomplished by measuring with a traveling microscope the distances of the numbered maxima and minima of fringe intensities from the previously described cross-wires which are a known distance from the wall. The fringe shifts in the boundary layer are then determined by the fringe number displacement from a least squares straight line fit through the points outside the boundary layer on fringe number vs distance plane. This technique of "locating the end-wall" represents an important modification of the approach used in previous experiments of this type where in the position of the end-wall relative to the fringes was essentially determined from its apparent position in a "no flow"

photograph. Using the present technique and estimating the uncertainty in magnification to be .5% for a nominal value of 2.24, the end-wall could be located relative to the fringe profile to within .016 mm (actual distance).

In order to align the test section light beam with the end plate of the shock tube, the technique given by Howes and Buchels<sup>(17)</sup> was used. According to the authors, the possible residual misalignment of their procedure should be less than .1 of the maximum misalignment due to the deviation from perfect collimation of the finite light source which is  $\omega \sim d/2L_f \sim .015/2(10) = .00075$  rad. The method depends on the formation of spurious fringes due to reflection from the surface and single edge diffraction patterns from the inlet and exit edges of the end-wall.

In the present boundary-layer studies, the object plane in the test section at which the fringes are focused is located two thirds of the width from the entrance window of the light beam. This choice is a result of the analyses in references 19 and 20 where it is shown that first order refraction errors are minimized when the fringes are focused at this plane.

In the un-ionized boundary layer experiments, snapshots of 2  $\mu$ sec duration were taken at 300  $\mu$ sec after initial shock reflection, while for the ionized boundary layer, they were taken at 100  $\mu$ sec after reflection. The method of experimentally determining the thermodynamic properties at the boundary layer edge for the latter case is described in Chapter IV. For the un-ionized case, they were assumed to be given by the theoretical frozen reflected shock conditions.

2.6 Shock Reflection Study. In this portion of the investigation, the rotating mirror camera described previously was used to obtain time-resolved, two-

wavelength interferograms. This was accomplished by orienting the fringes perpendicular to the shock tube axis, while, with the use of mirrors, the camera slit was oriented parallel to the tube axis. With the fringes and the test section focused on the camera slit and no disturbance present in the test section, a sweep of the slit image along the film plane will produce a series of light and dark fringes parallel to the direction of travel. The optics are adjusted so that the end wall forms one edge of the interferogram and so that the magnification is one to one. The field of view was limited to roughly 25 mm from the wall.

As the incident shock wave propagates into the field of view, the fringes behind the shock will be shifted relative to those in the initial test gas. Since the writing speed on the film is constant, the streak interferogram will show the shock as a straight line inclined toward the wall and across which the fringes have shifted an amount corresponding to the density jump across the shock. When the shock reflects from the end-wall, a similar trajectory is seen on the film emanating from the point of reflection, only inclined at a smaller angle to the wall depicting its lower speed. In most of the interferograms of the present study, the interferometer is adjusted so that the fringes shift away from the wall for an increase in refractivity or density. For the usual adjustment, since the electronic contribution is negative, the fringes will shift toward the wall when the electron concentration becomes adequate (see equation 2.4).

As noted above, it was not possible to take streak interferograms simultaneously at two wavelengths. A simple consideration of the geometry will assure the reader that in order to do so, completely separate records for each wavelength would be required, hence dictating use of another camera

or a major modification of the present camera. Cost prohibited the first of these alternatives while the loss in intensity through what would have been a necessary beam splitter precluded the second. The task was accomplished by making a series of shots at each of the three initial pressures for one of the wavelengths and plotting the resulting fringe shifts versus Mach number. This procedure was repeated for the second wavelength. The fringe shift for each of the two wavelengths at a given pressure and Mach number could then be read from these curves. As noted earlier, this is one of the primary reasons that consistent if not high purity initial conditions were necessary. The data reduction procedure will be made clear in Chapter IV where the fringe shift versus Mach number curves are presented.

In order to obtain the fringe shifts at 100 microseconds after reflection, (recall light source duration  $\sim 50 \mu\text{sec}$ ), it was necessary to repeat the above experiments with the light source triggered at  $40 \mu\text{sec}$  after reflection. The proportional delay unit provided a pulse for the two-channel time delay unit when the incident shock hit the wall; the two-channel delay then triggered the light source  $40 \mu\text{sec}$  afterwards. Since fringe contrast is poor after  $50 \mu\text{sec}$ , it was necessary to extrapolate these fringe shifts to  $100 \mu\text{sec}$  after reflection. As conditions at these longer times do not change rapidly, the error in extrapolating is estimated to be little more than .1 fringe.

### III

#### END WALL BOUNDARY LAYER WITHOUT IONIZATION

For the experimental conditions of concern in this chapter ( $M_s < 7$ ,  $P_1 \leq 10$  torr), the state of the gas in the reflected shock region may be determined accurately by the simple one dimensional theory which assumes constant specific heats and a constant reflected shock speed. Included in this ideal situation is the formation of a thin, thermal boundary layer between the cold shock-tube end-wall and the high temperature, but un-ionized, argon. This boundary layer which grows in thickness with the square root of time after reflection was studied with an interferometric technique similar to that used by Bunting<sup>(10)</sup> and which was to be subsequently applied to the investigation of the end-wall boundary layer in partially ionized argon. The experiments reported in this chapter thus serve to reexamine the technique and the previous results and in so doing to act as a calibration for the ionized boundary-layer experiments reported in Chapter V.

3.1 Theoretical Calculations. The un-ionized boundary layer on the shock-tube end-wall for a monatomic gas can be analyzed in a straightforward manner by assuming that the thermal conductivity is proportional to the local gas temperature raised to some exponent  $\nu$ , i. e.,  $K \propto T^\nu$ . This assumption is rather common, and for argon, the generally accepted value of  $\nu = .75$  is due to the work of Amdur and Mason.<sup>(11)</sup> Their result was obtained from calculations based on an exponent-six interparticle force potential at "low and intermediate" temperatures and an inverse power potential at "high" temperatures. The relevant constants in the potential were determined from beam experiments separately valid in three regimes of interparticle spacing-

Because these regimes overlapped, the results obtained for the thermal conductivity by substitution of the potentials into standard kinetic theory equations were smoothed between each regime. The value of  $\nu = .75$  in  $K_A \propto T^\nu$  correlates their results very well from 1000 to 15000°K and produces a value of thermal conductivity very close to the value of  $3.97 \times 10^{-5}$  cal/cm-sec-°K at 0°K given in reference 21.

In order to evaluate experimentally the temperature dependence, the measured temperature profiles from the interferograms described in the previous chapter are compared with profiles obtained from the theory described below. This comparison was accomplished by determining the mean and r.m.s. deviations between the two profiles at various values of the exponent  $\nu$  and plotting the results versus  $\nu$ . The value of  $\nu$  reported for any particular run then is the one for which the r.m.s. deviation is a minimum. It may be argued that the appropriate procedure would have been to compute a theoretical fringe number profile for a given value of  $\nu$  with the free stream fringe spacing determined from a no-flow interferogram and then make the statistical comparison in this plane. The primary argument for this approach is that no decision is necessary in the data reduction procedure as to which fringes are to be included in the boundary layer and which ones are to be used for determining the straight line for the free stream. However, for all the experiments reported here, there were enough fringes available to provide from twenty to thirty points for the straight line fit and approximately four or five data points in the outer portion of the boundary layer which show no fringe shift: i. e., no density change from the freestream. This fact justified proceeding in the simpler manner originally described for extracting a value of  $\nu$  from the data.

The shock tube end-wall thermal layer in the presence of an un-ionized gas is governed by the following equations:<sup>(10)</sup>

$$\frac{\partial \rho}{\partial t} + \frac{\partial (\rho v)}{\partial y} = 0$$

$$\rho \frac{\partial h}{\partial t} + \rho v \frac{\partial h}{\partial y} = \frac{\partial}{\partial y} \left( K_A \frac{\partial T}{\partial y} \right) \quad (3.1)$$

where it is assumed that the pressure is constant through the boundary layer and where  $\rho$  is the mass density,  $h$  the enthalpy per unit mass,  $v$  the velocity normal to the wall,  $T$  the temperature,  $K_A$  the thermal conductivity,  $y$  the distance normal to the wall, and  $t$  the time after reflection. With the similarity parameter

$$\eta = \left( \frac{\rho_\infty C_{p\infty}}{2 K_{A\infty} t} \right)^{1/2} \int_0^y \frac{\rho}{\rho_\infty} dy \quad (3.2)$$

$dh = c_p dT$ ,  $C_p = \text{constant}$ , and the assumed temperature dependence for the thermal conductivity

$$K_A = K_{Aw} (T/T_w)^\nu \quad (3.3)$$

this equation is reduced to the single ordinary differential equation

$$\Theta'' + (\nu-1) \frac{T_\infty - T_w}{T} (\Theta')^2 + \left( \frac{T_\infty}{T} \right)^{\nu-1} \eta \Theta' = 0 \quad (3.4)$$



where the subscripts  $\infty$  and  $w$  refer to conditions in the free stream and at the wall respectively and the primes denote differentiation with respect to  $\eta$ .

The boundary conditions are taken as

$$\begin{aligned} \theta = 0 \quad \text{at} \quad \eta = 0 \\ \theta \rightarrow 1 \quad \text{as} \quad \eta \rightarrow \infty \end{aligned} \quad \theta \equiv \frac{T - T_w}{T_\infty - T_w} \quad (3.5)$$

The numerical procedure used in solving the above equation is discussed in reference 10 along with comparisons to the results of other authors. (22)

3.2 Experimental Results. The method of obtaining the fringe shifts,  $S$ , in the boundary layer was described in Chapter II. From these fringe shifts, the density profile can be readily obtained from the simple equation

$$\frac{\rho}{\rho_\infty} = \frac{S\lambda\rho_0}{L(\mu_A - 1)_0\rho_\infty} + 1 \quad (3.6)$$

where  $\rho_\infty$ , the density in the undisturbed region, is obtained from the solution to the reflected shock equations for a perfect gas and a known Mach number and initial density. Because the pressure is assumed constant in the boundary layer, the temperature may be obtained from the density measurements and the perfect gas equation.

All of the interferograms in these experiments were taken at 300  $\mu$  sec after reflection. That the thermodynamic properties in the undisturbed gas for the range of conditions considered here are given by the theoretical values and that they prevail for over 300  $\mu$  sec after reflection is substantiated in the following chapter and in references 23 and 24.

Four runs were made in this series at conditions where ionization could be completely neglected, as just mentioned. Table I below summarizes the results by listing the initial conditions, the freestream temperature and the resulting value of the temperature exponent  $\nu$  for each of the two wavelengths. The mean value obtained for  $\nu$  is .75 with a .011 r. m. s. deviation of the mean. For reasons which will be explained shortly, this value differs from  $\nu = .668$  reported in reference 10.

TABLE I

Summary of results of measurements of argon thermal conductivity  $k = k_{\text{wall}} (T/T_{\text{wall}})^{\nu}$ , for  $k_w = 4.25 \times 10^{-5}$  cal/cm-sec- $^{\circ}$ K,  $T_w = 297^{\circ}$  K, time after shock reflection 300  $\mu$ sec

RUN NO.	MACH NO.	INITIAL PRESSURE (Torr)	FREE STREAM TEMP. ( $^{\circ}$ K)	WAVE-LENGTH ( $\text{\AA}$ )	POWER LAW EXPONENT ( $\nu$ )
710	3.52	5	2883	4530	.775
				5720	.715
712	3.26	10	2486	4530	.750
				5720	.788
713	6.40	5	9183	4530	.702
				5720	.758
714	4.98	5	5625	4530	.732
				5720	.799

To further exhibit the data, figure 4 shows a "no flow" and "flow" interferogram at each of the two wavelengths for RUN 714 and figure 5 presents the results for this run in the form of a  $\Theta$  versus distance plane with the theoretical curve superimposed. It is believed that the data sample here is too small to draw any major conclusions concerning the relative behavior of the results for each of the two wavelengths; although, the apparent difference

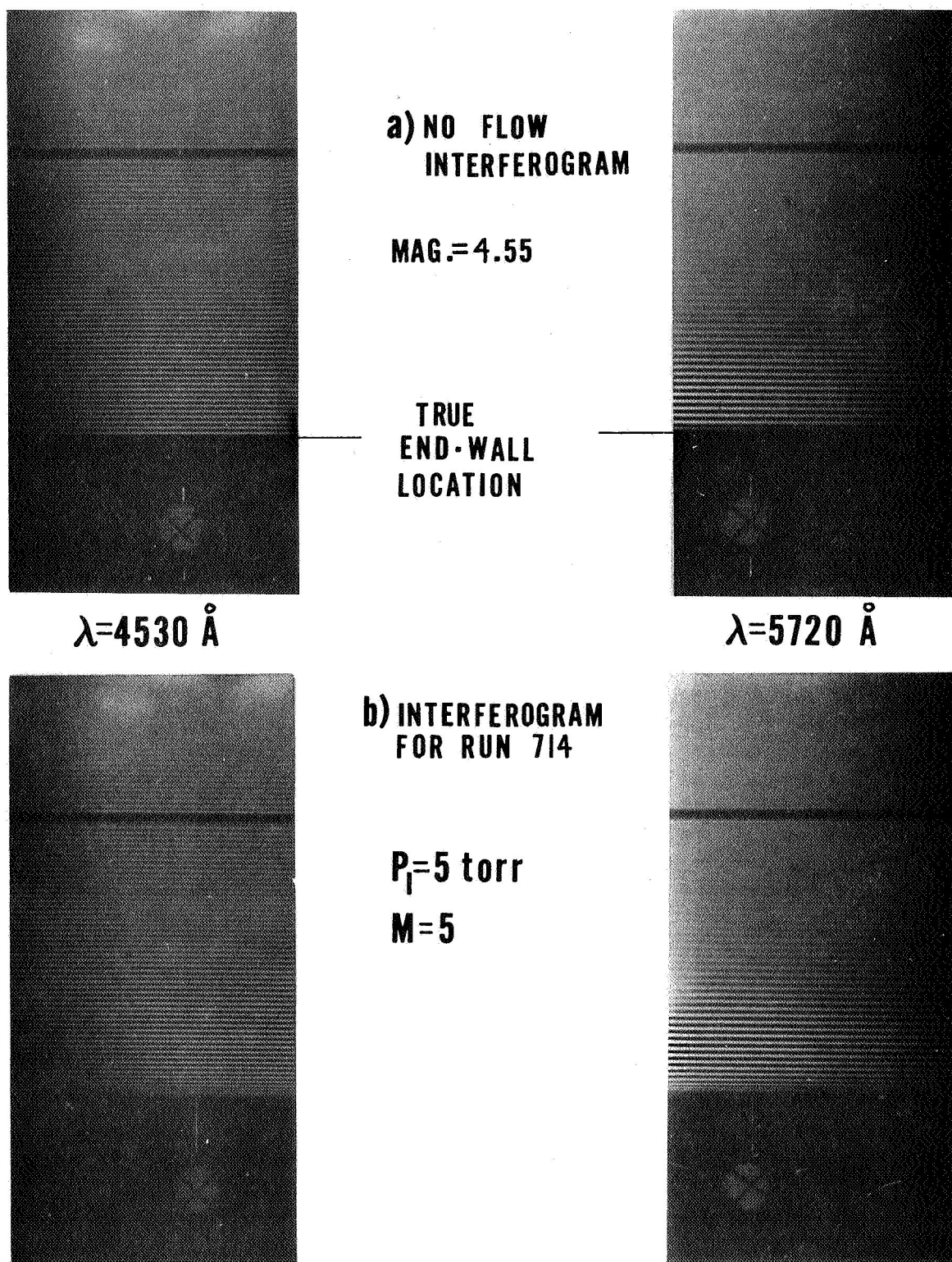


Figure 4. Flow and no-flow un-ionized boundary layer interferograms of run 714 for two wavelengths.

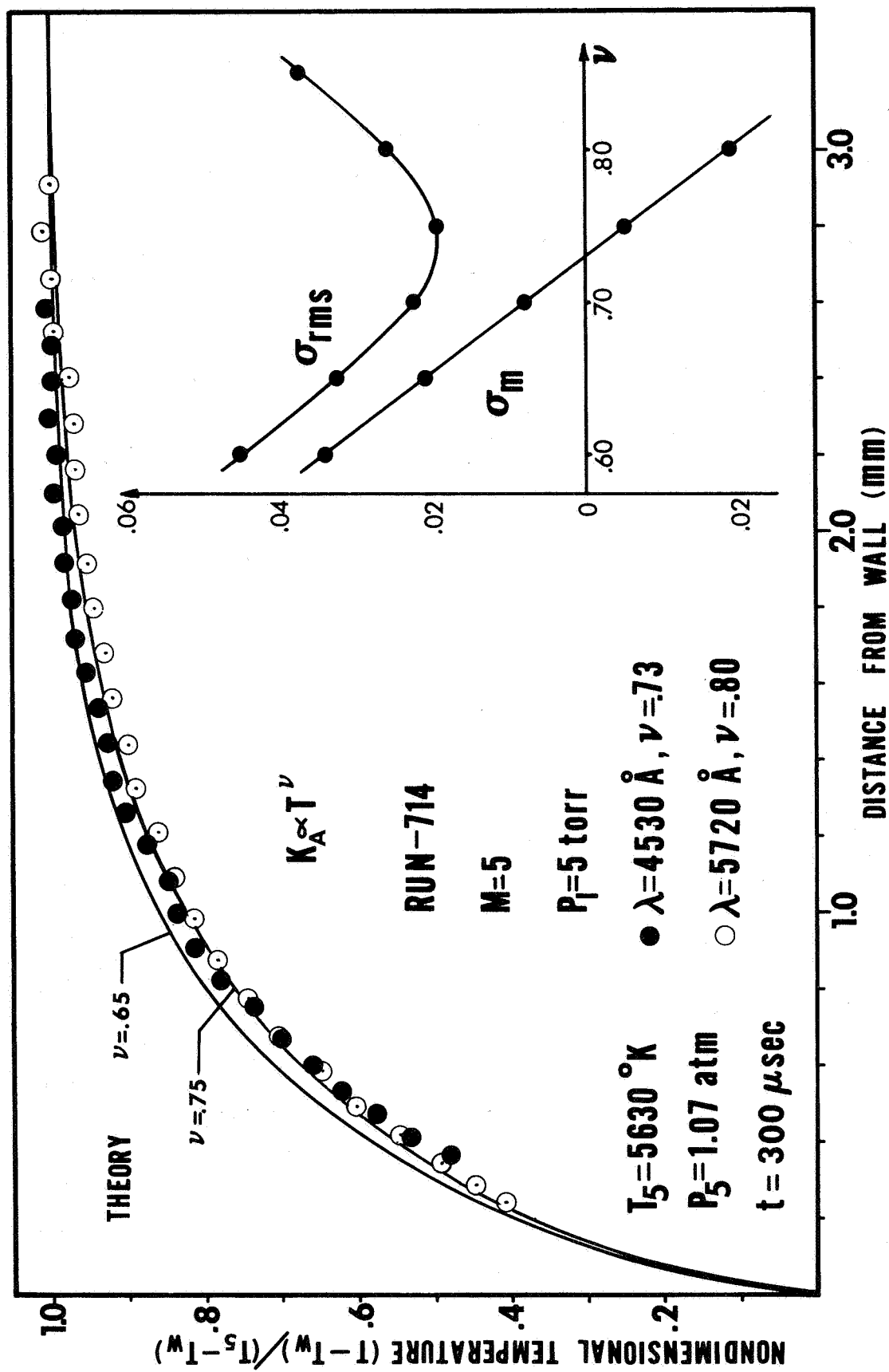


Figure 5. Comparison of experimental temperature profile with theory for un-ionized boundary layer.

in shapes of the experimental profiles shown in the figure 5 was typical. This observed behavior can be attributed partially to a combination of errors in pertinent measured quantities such as magnification and end-wall location. The subplot shown in figure 5 is an example of the method described above by which one obtains the best value of  $\nu$  from the data. The r.m.s. deviation of the experimental data from the theory using various values of  $\nu$  is plotted versus  $\nu$ , and the value yielding the minimum r.m.s. deviation is selected.

From these results, although admittedly a small sampling, it would appear that the results of Amdur and Mason are validated, hence supporting the interparticle force potentials used in their analyses. This conclusion agrees more closely with references 1, 25, and 26 than with the work of Bunting<sup>(10)</sup> ( $\nu = .668 \pm .02$ ) whose basic technique is essentially applied in the present investigation. For reasons which have already been suggested and which are more fully described in the following section, Bunting's<sup>(10)</sup> results and preliminary results of this author can be shown to be in accord with present value of  $\nu$ . The number of data points collected with the technique used here can thus be taken as considerably more than those shown in Table 1. Moreover, this fact implies that the small scatter in the values of  $\nu$  associated with this method ( $\pm .05$ ) is retained, in comparison, for example, to the heat transfer measurements of Camac and Feinberg<sup>(1)</sup> who reported  $\nu = .76 \pm .03$  for a large number of runs with a scatter of  $\pm .15$ .

3.3 Sources of Error. To evaluate the sensitivity of this approach properly, one should determine the parameter  $d\nu/d$  (profile) which would indicate for example, how much a uniform displacement of the experimentally determined boundary-layer profile would change the resulting value of  $\nu$ .

Although a general analytic expression for this parameter would be difficult if not impossible to obtain, certain qualitative comments are possible. Of particular interest is the fact that only a small translation of the profile away from the wall is necessary to increase significantly the value of  $\nu$  obtained from the comparison with the theoretical profile. It can also be noted that the sensitivity increases as the data extends more deeply into the boundary layer. It was found from an examination of all the available data that an approximate value for the above parameter with regard to a shift of the profile relative to the wall is larger than  $1 \text{ mm}^{-1}$ ; that is to say, for a .1 mm shift in the experimental data, the value of  $\nu$  will change by .10.

Now, it should be clear why an accurate location of the end-wall relative to the profile is very critical in the data reduction. In the previous experiments of the present author and in Bunting's experiments<sup>(10)</sup>, a systematic error was incurred because the end-wall position relative to a reference was located by its apparent position in a no-flow photograph and not by a separate and precise measurement as described for the present case in Chapter II. The systemic error incurred by the former technique results from the single edge diffraction pattern formed by the parallel light and the edge of the end-wall. The geometric shadow of the surface is thus masked by the "central" or first dark fringe of the diffraction pattern (see for example reference 27, page 370.) and the apparent position of the wall will thus be too far into the boundary layer profile. That is an experimental profile such as that shown in figure 5 would be incorrectly "located" closer to the wall. Placing the crosswire references in the end wall as described in Chapter II allows a completely independent measure of the location. Previously a wire mounted outside the test section was used as the reference in the interferograms. Thus any uncertainties which

may have been associated with this fact are avoided because the cross wires used here as the reference are in the plane of focus. From measurements of photographs such as figure 4, it was found that the error incurred was on the order of .06 mm. This means that the resulting value of  $\mathcal{V}$  would be approximately .06 too low. By considering figure 6, for example, which was taken directly from reference 10, one can readily see that if the experimental profile is shifted .06 mm farther away from the wall, the best theoretical fit would be provided by the profile for  $\mathcal{V} \cong .75$ .

In examining other sources of error, it was found that a +2% error in the measured Mach number produced a -1.4% error in  $\mathcal{V}$ , while such things as a slight cooling of the free stream gas from its assumed constant temperature had a negligible effect. In performing optical experiments in the presence of density or refractivity gradients, the possibility of errors in the measured fringe shift exists due to refraction of the light rays traversing the test section normal to these gradients. References 10, 19, and 20 all give analyses to determine the magnitude of this error, and in each reference it is assumed that the light ray trajectories and index of refraction can be expressed as power series in terms of the ray displacement. In the present analysis, the theoretical boundary layer solution in conjunction with Fermat's principle was used to solve for the light ray trajectory (assuming a point light source). The results were then used in the appropriate equations to find the magnitude of possible fringe shift error in the measured profiles. The details and results of the analysis are given in Appendix A. The magnitude of the possible fringe shift error is of the order of .01 fringe, close to the wall, relative to the fringe shift one would measure if there were no refraction. This is larger than the results of reference 10, but still less than the assumed reading error of .05

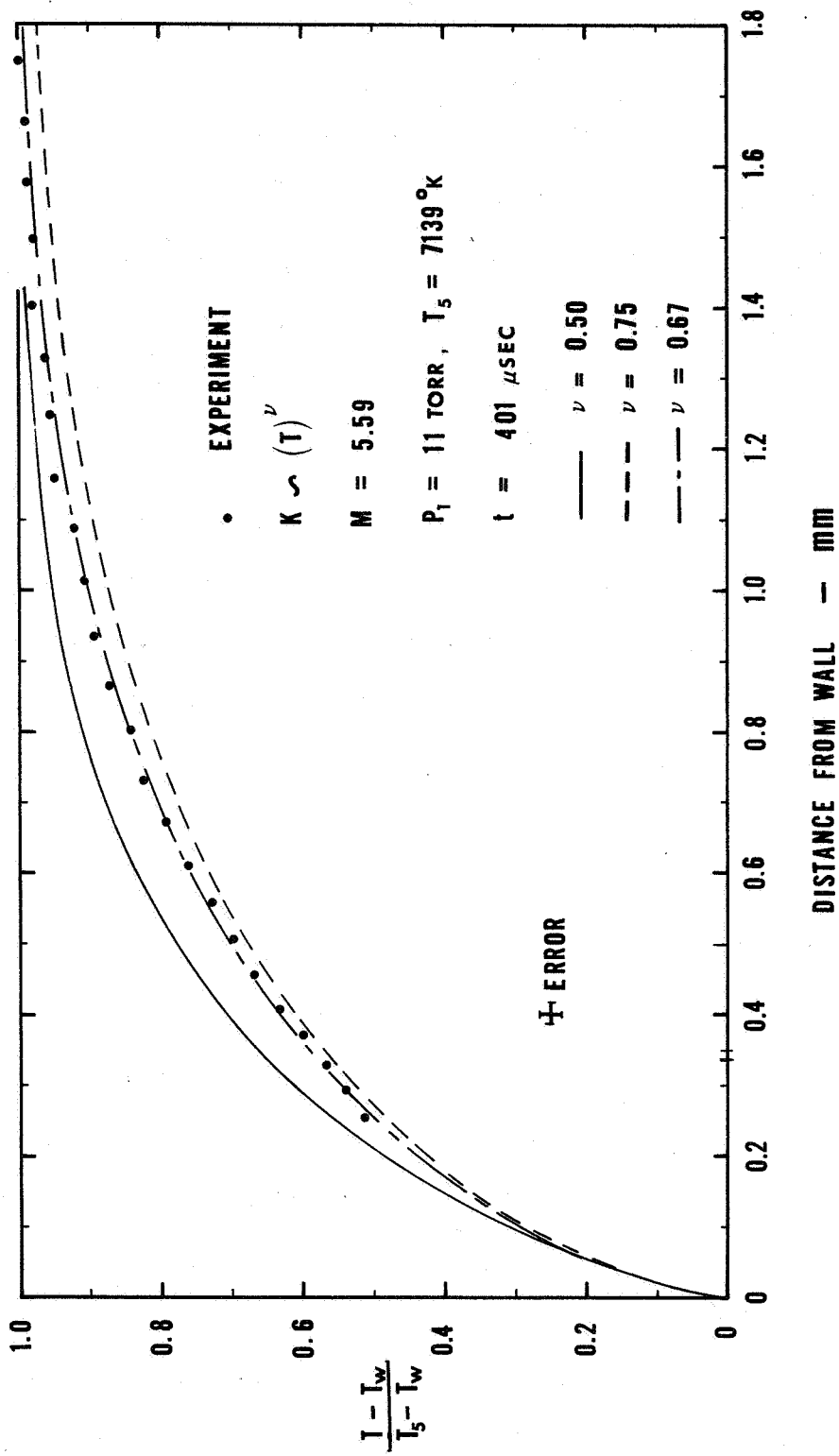


Figure 6. Un-ionized boundary layer profile from reference 10.



fringe.

The present technique for making measurements of the end-wall boundary layer without ionization appears to be established adequately enough to justify proceeding to ionized boundary layer measurements. This contention is based on the excellent agreement observed between the present temperature dependence of argon thermal conductivity and that found by other investigations employing heat transfer measurements. In addition, the present investigation is supported by the results obtained via beam experiments in conjunction with kinetic theory (Amdur and Mason<sup>11</sup>). The ionized boundary-layer experiments were performed, and the results are discussed in Chapter V. Before proceeding to those results, however, the complications arising from the wave interactions occurring in the shock reflection process for ionizing argon will be considered.

#### IV

### THE SHOCK REFLECTION PROCESS IN IONIZING ARGON

As indicated in the introduction, the shock reflection process in an ionizing argon gas is considerably more complicated than that which yielded the test conditions discussed in the preceding chapter. In this chapter the various interactions as observed in streak interferograms are discussed in some detail, and wherever appropriate, comparisons with previous investigations are given. In subsequent sections the qualitative results for argon are compared with other gases, and the measured time histories of the thermodynamic properties, including the approach to equilibrium, in the reflected shock region are presented. The notation used here to designate various regions of the flow field and wave interactions differs only slightly from that introduced by Smith<sup>(2)</sup> and will be explained in terms of a so called x-t (distance vs time) diagram of the reflected shock structure. As explained in Chapter II, the streak interferograms presented here are, in fact, experimentally determined x-t diagrams.

All of the streak interferograms shown here were taken with the interferometer adjusted so that an increase in refractivity causes the fringes to shift to the left or away from the wall. Therefore, when the density increases across the incident shock, the fringes shift to the left, but when an adequate number of electrons are produced or the density decreases, the refractivity decreases and the fringes will shift toward the wall (see equation 2.4). Furthermore, all the photographs are positive prints so that dark areas are unexposed and vice versa. Consequently, in the cases where radiation from the test gas is significant, the fringes will appear faded or overexposed. In addition, the reader should ignore the bands of high and low intensity distributed along the time axis since these are

caused by "ringing" in the exploding wire light source. In the following discussions, as many interferograms as practical will be shown.

4.1 Description of the Reflection Process. To begin the discussion, figure 7 is presented as an example of an interferogram and an x-t diagram for the reflection process at what has been termed "mild" conditions. The incident shock appears in the lower portion of the photo as a break in the fringes along a line inclined to the wall. Across this line the fringes shift away from the wall by an amount corresponding to the density jump across the shock, the value of the initial density and the particular wavelength being used. The reflected shock leaves the wall with a constant speed which is less than the speed of the incident shock; it is therefore inclined at a smaller angle to the wall. It is mentioned here that the point at which the reflected shock appears to leave the wall is taken as the zero point for the time scale.

The slope of the so called particle paths at any point in the x-t diagram of figure 7 represents the fluid velocity at that point in the flow field; hence, behind the reflected shock, it has zero slope with respect to the wall. In connection with the assumption made in the last chapter regarding the existence and constancy of the theoretical conditions in the reflected shock region, it is noted that the fringes after reflection remain straight and parallel to the wall. Furthermore, the measured fringe shifts from the conditions in 1 to 2F and from 1 to 5F agree exactly with the theoretical fringe shifts based on perfect gas calculations for  $\gamma = 5/3$ . In section 4.3.1, it is also shown that relaxation times for conditions similar to those of figure 7 are on the order of hundreds of microseconds.

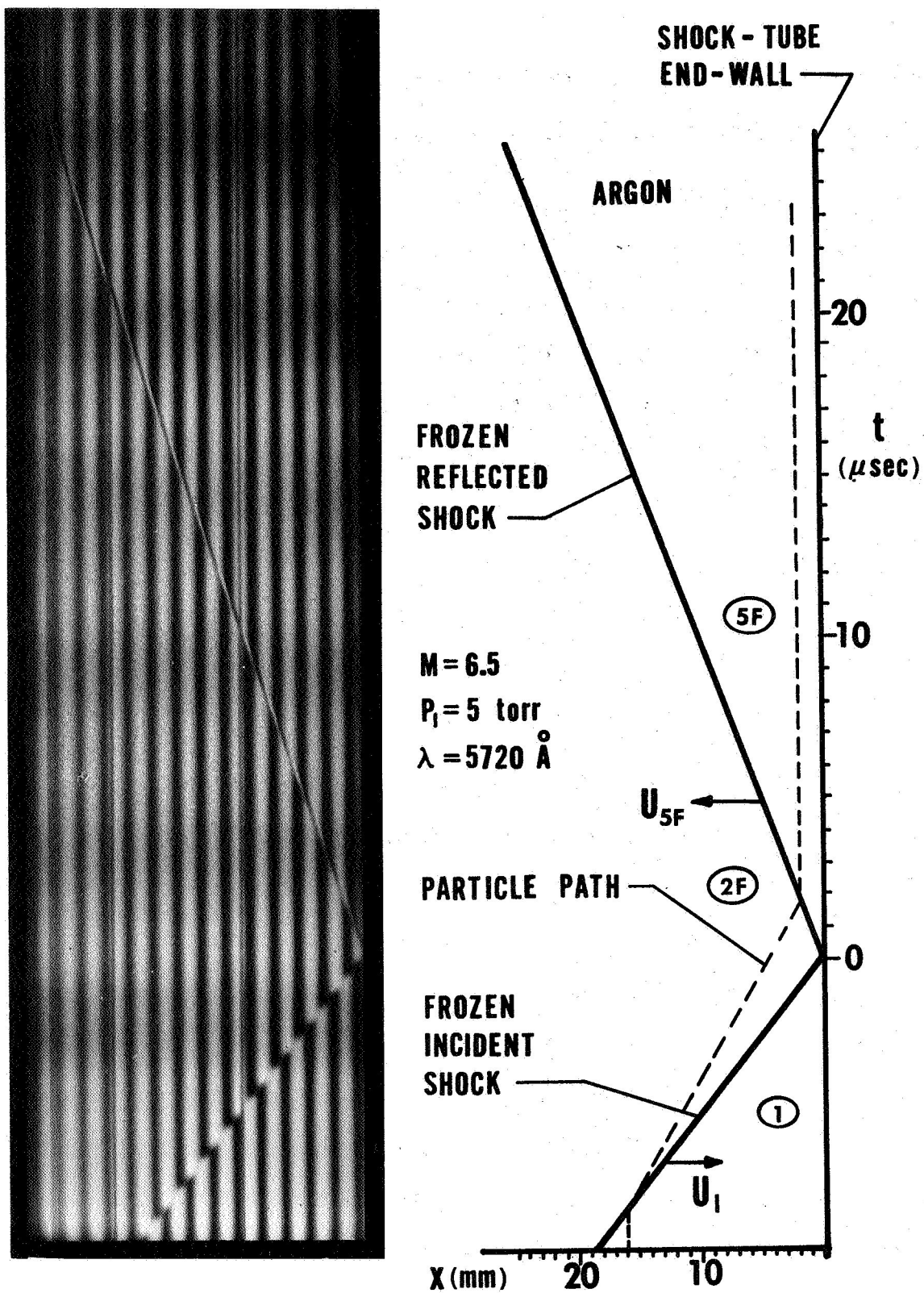


Figure 7. Streak interferogram and x-t diagram of shock reflection process with no ionization (argon).

As the incident shock strength is increased, the density and temperature in the reflected shock region become so high that the time to achieve full equilibrium behind the reflected shock is considerably shortened. Correspondingly, the degree of ionization at equilibrium will become large enough so that the presence of electrons will be quite noticable in the interferograms. An interferogram for conditions such that the equilibration behind the incident shock is only slightly visible is shown in figure 8 along with a corresponding x-t diagram. Immediately after reflection, the state of the gas behind the reflected shock in region 5F, and the speed of the reflected shock,  $U_{5F}$ , correspond closely to what one would obtain from perfect gas calculations. As occurs behind the incident shock, the approach to equilibrium is characterized by the sudden onset of ionization equilibrium.<sup>(2, 5, 6)</sup> Behind the reflected shock, this cascading of the ionization process appears to occur in the last 15 to 20% of the relaxation time,  $\tau_5$ , that is required to achieve full equilibrium, denoted 5E. The reflected shock ionization front,  $I_5$ , appears in the interferogram as a sudden shift of the fringes toward the wall. After equilibration the fringes in figure 8 begin to slope away from the wall. This is an indication that recombination or radiative cooling is causing a decrease in electron concentration, hence an increase in the refractivity (equation 2.4).

For the example under consideration, the temperature decreases and the density increases across the thin reflected ionization front by factors of  $T_{5E}/T_{5F} \sim .45$  and  $\rho_{5E}/\rho_{5F} \sim 1.7$ . In order to supply the necessary mass addition for this density increase, an expansion wave originating at the point of equilibration at the wall must propagate into the quiescent gas in region 5F. The presence of such a wave system is clearly demonstrated by the fringe shift toward the wall before the onset of equilibrium. Since there are not enough

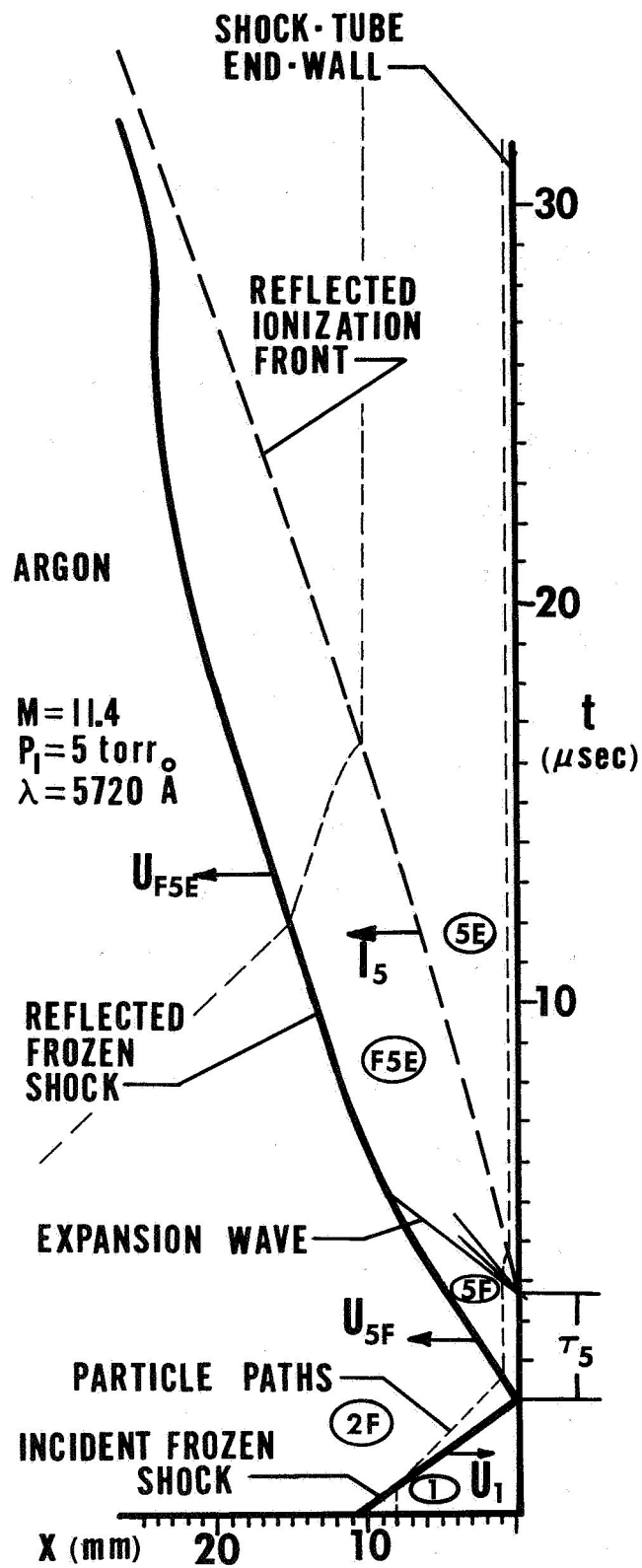


Figure 8. Streak interferogram and x-t diagram of shock reflection process with ionization behind reflected shock (argon).

electrons present in this region to cause such a fringe shift, one must conclude that it is caused by changes in mass density as would occur through the expansion wave. As seen in the x-t diagram, the ionization front then acts to bring the fluid to rest again after it has been accelerated toward the wall by the expansion wave,

The existence of this expansion wave was first hypothesized by Camac and Feinberg<sup>(1)</sup> in connection with their end-wall heat transfer measurements in argon. However, on the basis of his calculations in conjunction with end-wall pressure measurements in xenon, Smith<sup>(2)</sup> proposed that the reflected translational shock was primarily decelerated by the heat sink action of the ionization process distributed throughout the nonequilibrium region behind the shock. In fact, from the present data for argon at higher Mach numbers and for the few experiments done in xenon, it appears that both of these phenomena have an effect on the reflected shock speed. Camac and Feinberg also predicted that for sufficiently strong incident shocks, an inverse Chapman-Juguet condition would result at the ionization front,  $I_5$ ; that is, the fluid would leave the front supersonically and be brought to rest by an additional shock wave between the front and the end-wall. However, no evidence of such a shock was observed in any of the interferograms for the range of conditions considered here.

Upon overtaking the reflected shock, the expansion wave causes a rather sharp deceleration of the shock as can be seen in the interferogram of figure 8. To further substantiate that this is the result of an expansion wave overtaking a shock wave, one notes that the front of the expansion wave should propagate at the frozen speed of sound in region 5F. To show that this is the case,

figure 9 is presented wherein the quantity  $\alpha / \tan^{-1}(v_w/a_{5F})$  is plotted versus incident shock Mach number. The numerator of this ratio is the measured value of the angle between the normal to the wall and a line drawn between the point of equilibration at the wall and the point on the reflected shock where the deceleration appears to begin. The denominator represents the direction in the interferogram that would be followed by a disturbance propagating at the speed  $a_{5F}$ , the frozen speed of sound in region 5F.  $V_w$  is the writing speed on the film. Despite the fact that the measurement of  $\alpha$  is not very precise, the figure shows that the measurements are in fair agreement with the theoretical value of unity for this ratio. As implied previously, although an expansion wave system is visible in the interferograms obtained for xenon, the reflected shock appears to be slowing considerably before it is overtaken by the expansion wave. This was also the case at stronger conditions in argon, indicating that the heat sink effect of the ionization process is already acting to slow the shock. The snapshot interferogram of figure 10 was taken at a time indicated by the x-t diagram below it and clearly indicates the presence of the fringe shift across the expansion wave.

Because of the distinct difference in the thermodynamic and fluid dynamic properties in the region bounded by the reflected shock, ionization front, and the expansion wave system, the region has been denoted F5E. This nomenclature has been chosen to indicate that the gas is still frozen but that its state is a result of the equilibration to region 5E. The shock speed  $U_{F5E}$  may be closely approximated by "quasi-steady" reflected shock calculations assuming frozen conditions behind the incident shock and equilibrium conditions behind the reflected shock. (see Appendix B) The "non-reacting" state F5E may then be obtained by frozen calculations across a shock of speed  $U_{F5E} + U_{2F}(\text{LAB})$



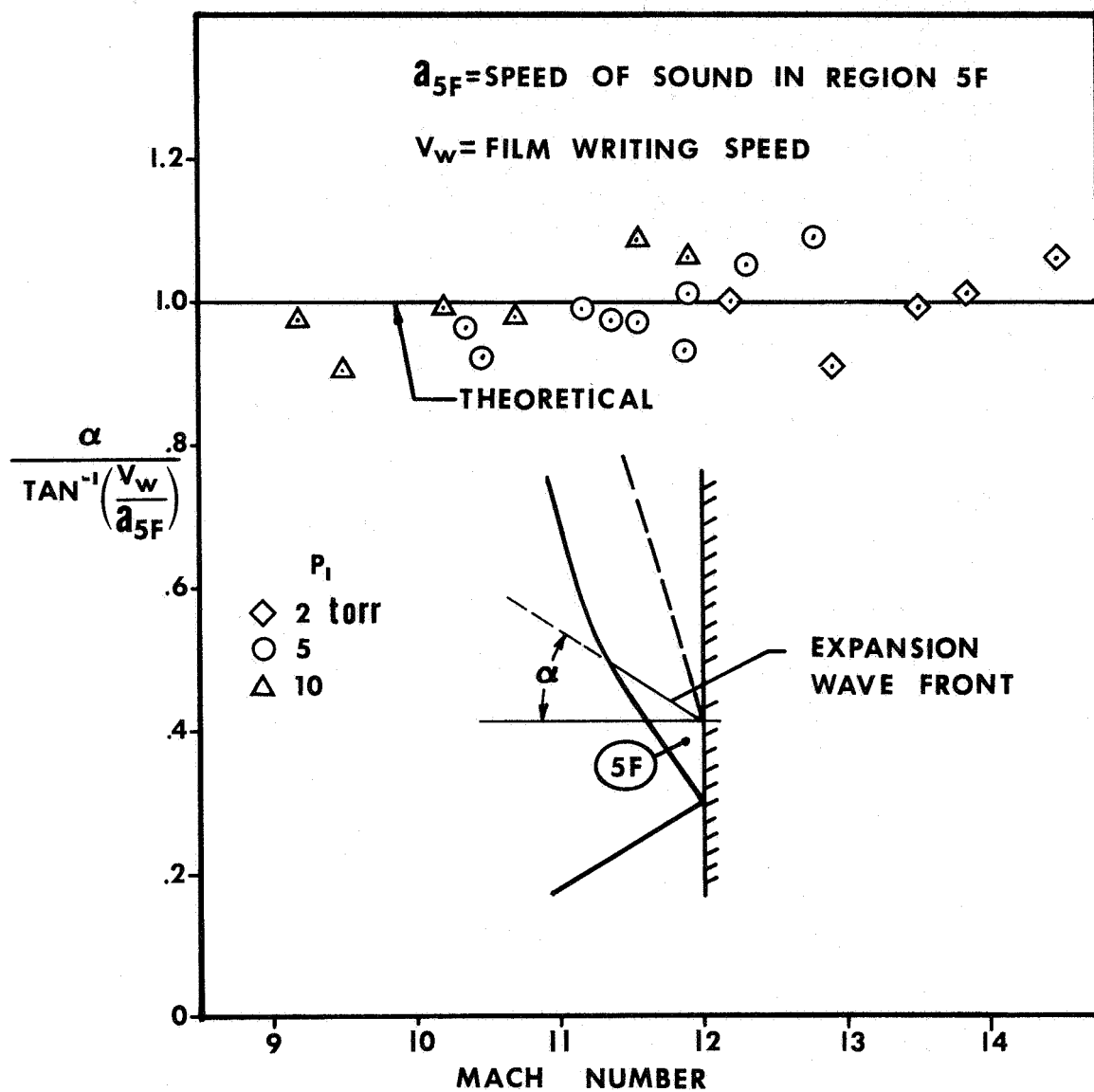


Figure 9. Comparison of expansion wave front speed with acoustic speed in region 5F (argon).

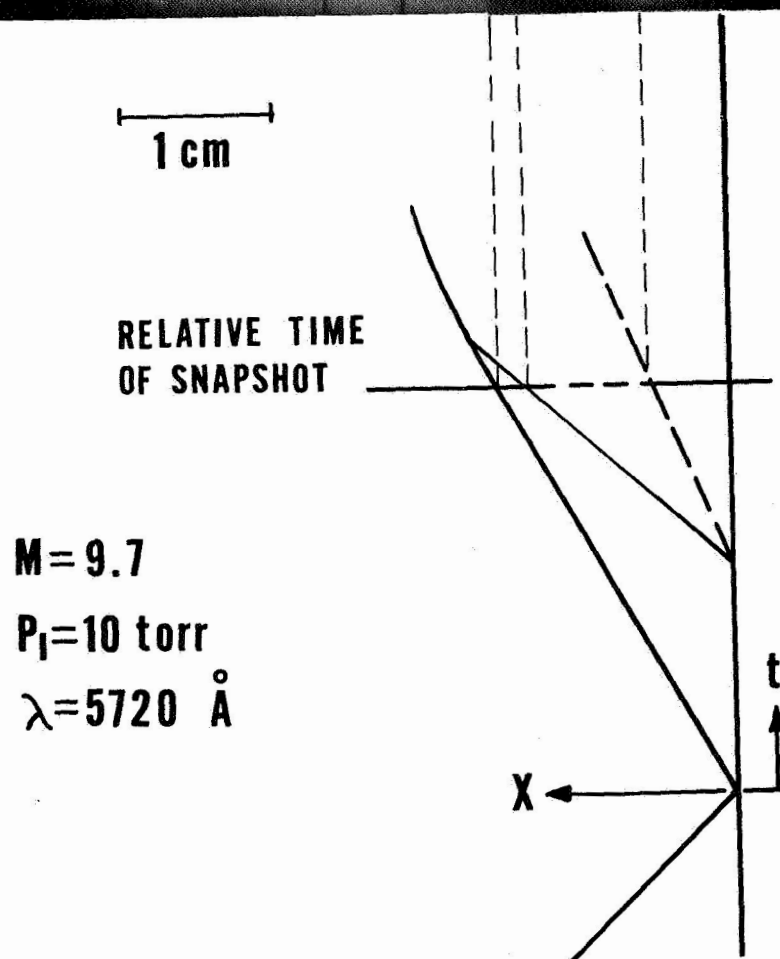
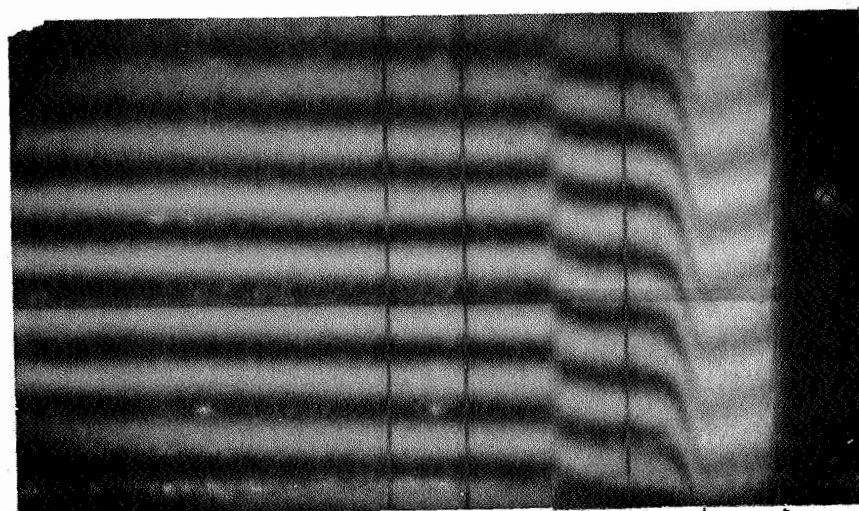


Figure 10. Snapshot interferogram showing expansion wave behind the reflected shock (argon).

into conditions 2F. To illustrate that this is the case, a plot of the measured and theoretical speeds  $U_{F5E}$  versus Mach number is shown in figure 11. Although the scatter in the measurement is large, this figure is presented to illustrate that the measured shock speed tends to be somewhat lower than the theoretical values. This agrees with what one would expect from the measured thermodynamic data presented in the following sections where it is shown that the measured density  $\rho_{5E}$  is greater than the theoretical value. The fluid velocities represented by the particle paths shown in the x-t diagram of figure 8 are scaled from theoretical calculations and as can be seen, are appreciable in magnitude.

Before continuing, it may be noted that the speed of propagation of the ionization front  $I_5$  is less than  $U_{5F}$  and approximately equal to  $U_{F5E}$ . This is consistent with the presence of an expansion wave for two reasons. First, one might expect the relaxation process to take place at a slower rate due to the cooling in the expansion wave; hence the longer relaxation time away from the wall. Second, and more important, the particle time or residence time away from the wall in the reflected shock region,  $\tau_{5P}$ , is less than the laboratory time,  $\tau_{5L}$ , unlike what occurs behind the incident shock where

$$\tau_{2P} \sim (\rho_{2F}/\rho_1) \tau_{2L} > \tau_{2L}$$

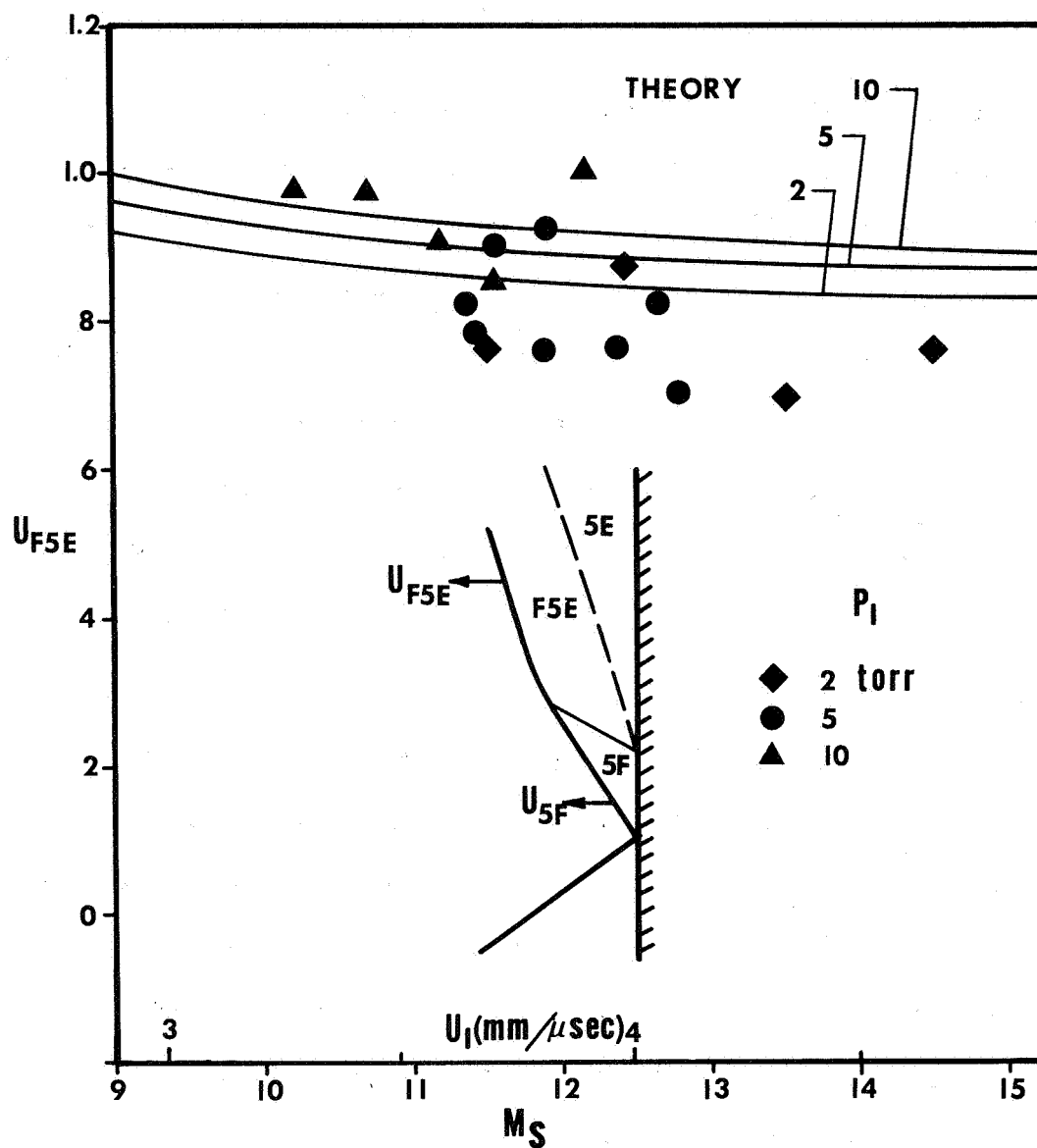
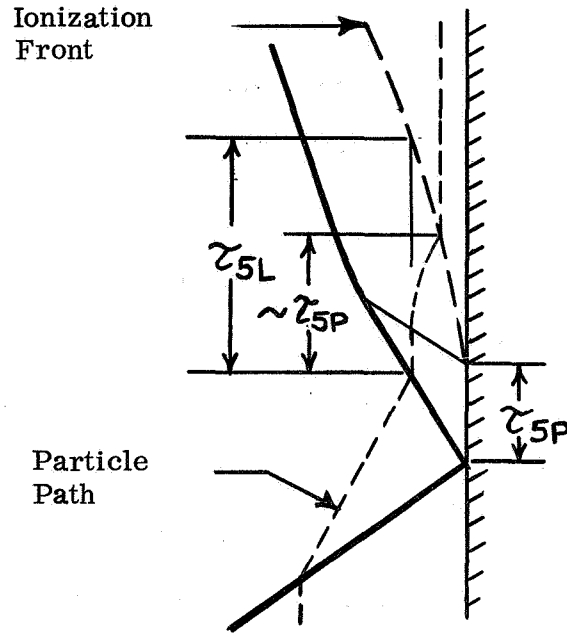


Figure 11. Comparison of measured reflected speed  $U_{F5E}$  with "quasi-steady" theory (argon).

This discussion is readily illustrated by the following sketch:



It should be obvious that one cannot measure the reflected shock speed by any techniques which depend directly on the propagation speed of the radiation or ionization front  $I_5$ . Care must also be taken in measuring  $\tau_{5P}$  at any distance into the flow field.

As the incident shock strength is increased even further, the ionization front  $I_2$  becomes visible on the time scale of the present investigations. The shock attenuation may be considered negligible over the field of view and therefore,  $I_2$  will be traveling at the same speed as the incident shock  $U_5$ . The ionization front  $I_2$  is a rather "thin" region as shown in reference 5 where it is found that approximately 80% of the change in conditions from the frozen state 2F to the equilibrium state 2E takes place in the last 20% or less of the relaxation time  $\tau_{2L}$ . The wave system resulting from the interaction of the reflected and incident shock structures is clearly visible in the interferograms

of figure 12. Because of the added complications, the x-t diagram is presented separately in figure 13.

A few words regarding the character of the interferograms in this figure are in order. Both of the interferograms are taken at approximately the same test conditions. The one on the left is of the usual type with the fringes shifting away from the wall for an increase in refractivity. The interferogram on the right was taken with the interferometer initially adjusted for an "infinite fringe" or "zero order fringe", and although impractical for quantitative measurements in these experiments, it is quite striking for its visualization of the various wave interactions. The fringes on such an interferogram represent contours of constant refractivity, or for the un-ionized portion of the flow field, constant density. Where the gas is ionized, however, all one can say is that the density and degree of ionization combine in such a manner as to maintain a constant refractivity. As an example of these points, the fringe shift across the incident shock in figure 12 (a) is approximately  $1/2$  fringe; therefore, the infinite fringe interferogram in figure 12 (b) changes from completely light to completely dark. The x-t diagram in figure 13 is a direct copy of the patterns observed in 12 (b).

The incident shock ionization front is quite visible in figure 12 (b) because the expected fringe shift across  $I_2$  for these conditions is .2 fringe. The reader will find small fringe shifts such as this more obvious in the regular interferograms by sighting along the fringes rather than looking directly down on the page. The state of the gas in region 2E may be obtained from normal shock equations and the equilibrium equation of state as verified in reference 5.

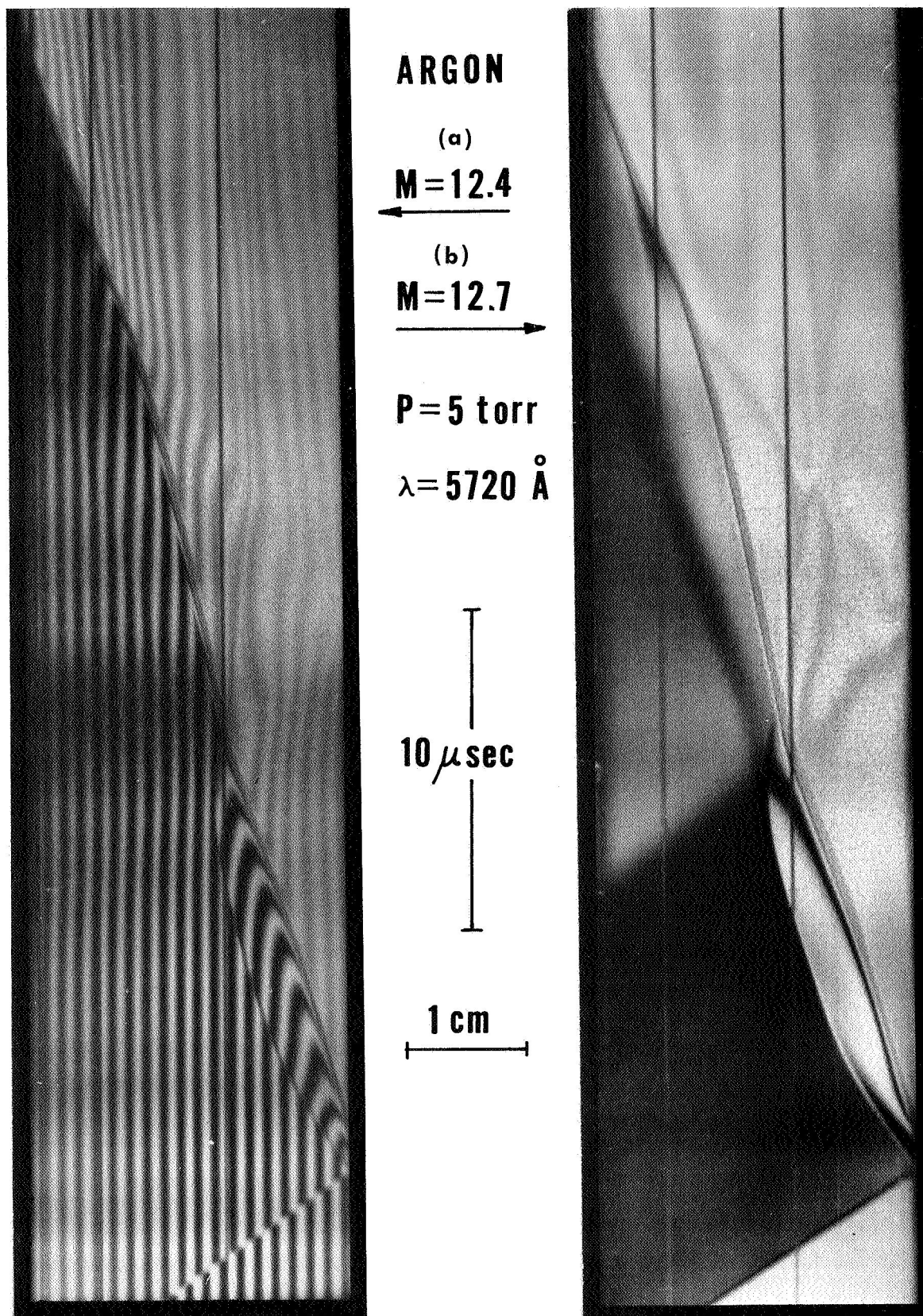


Figure 12. Regular and infinite fringe streak interferogram of reflection process with ionization behind incident shock (argon).

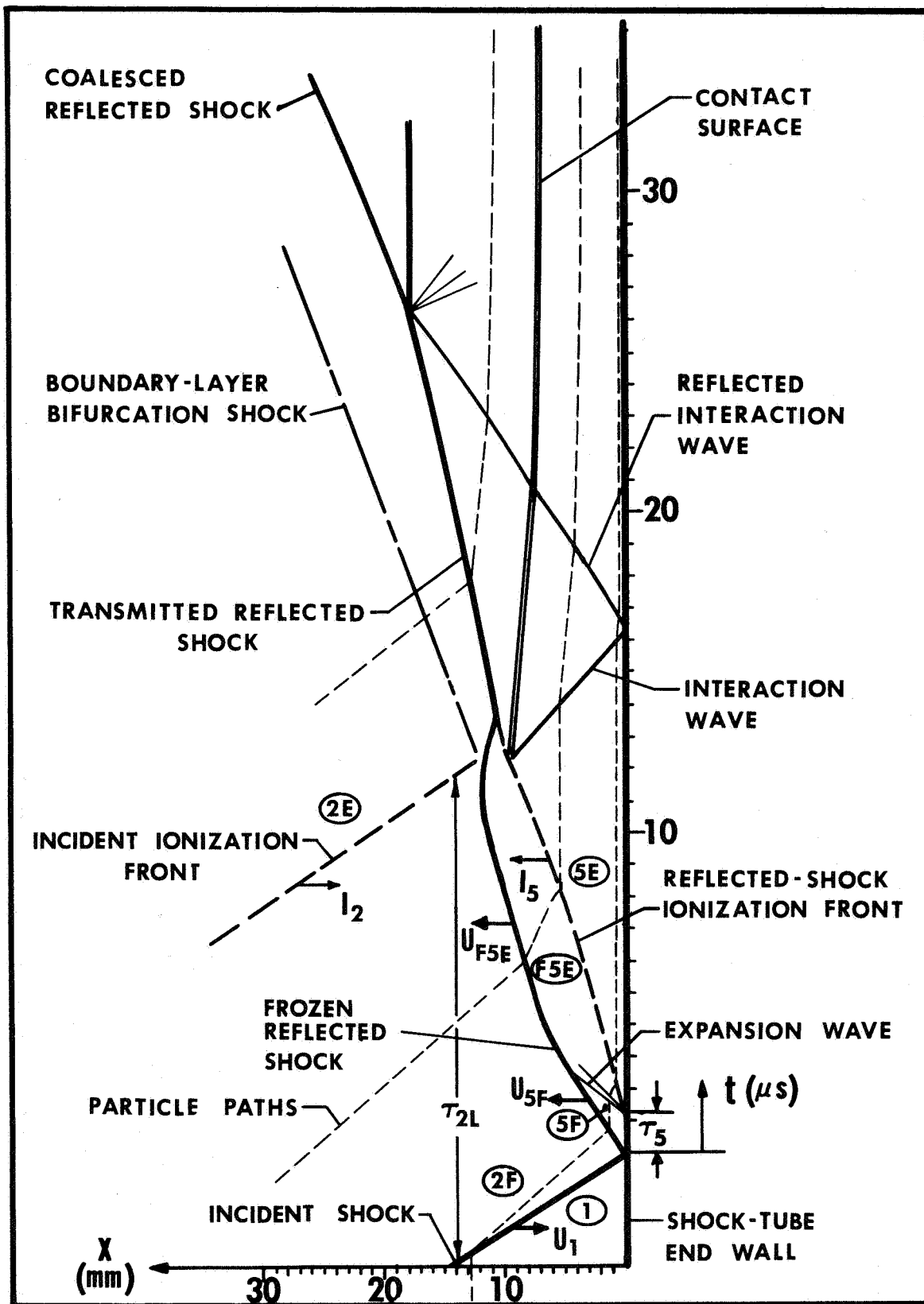


Figure 13. Distance vs. time ( $x$ - $t$ ) diagram of shock reflection process with ionization behind incident shock ( $M = 12.7$ ,  $P_1 = 5$  torr, argon).



The nature of the interactions can be described approximately by concepts applied in shock-shock interactions. When two normal shocks traveling in opposite directions meet, each one is transmitted with a strength dependent on the initial strengths of each wave. Thus since the incident shock ionization front is a fairly steep density gradient,  $\rho_{2E}/\rho_{2F} = 1.43$ , it will be transmitted as a compression wave, termed the "interaction wave" in the x-t diagram of figure 13. The reflected shock will also be transmitted but with a lower velocity in the laboratory coordinates. It should be noted that although the reflected shock in these coordinates slows to zero and moves back to the wall as it passes through the incident ionization front, its speed is still supersonic relative to the gas behind the incident shock. The interaction wave propagates to the wall whereupon it reflects and subsequently overtakes the transmitted reflected shock. The two waves coalesce into one shock traveling faster than either of the initial waves. These interactions require the presence of a contact surface, as shown on the x-t diagram, because the fluid along adjacent particle paths has gone through different entropy producing shock waves. On each side of the contact surfaces, the pressure and velocity are equal, but the other thermodynamic variables may differ considerably. These contact surfaces are quite visible in the interferograms of figure 12.

The unusual trajectory of the reflected ionization front results because the electron concentration behind the incident shock is increasing before the state 2E is completely attained. The presence of these additional electrons reflects itself in a decreased relaxation time behind the reflected shock. Furthermore, because of the relatively high electron concentration at conditions 2E (for this case,  $n_{e2E} = 3.7 \times 10^{16} \text{ cm}^{-3}$ ), the interaction between the reflected shock, the reflected ionization front, and incident ionization front

takes place in a relatively small region on the x-t diagram.

When the shock strengths were strong enough to show the incident ionization front, it was possible to obtain simultaneous measurements of both the incident and reflected shock ionization relaxation times. As a matter of definition, the measured times  $\tau_{2L}$  (laboratory time) was taken as the time to achieve complete equilibrium after passage of the incident shock wave. This time is indicated on the x-t diagram of figure 13. The results will be presented in the next section. It was found that this time was approximately 15 to 20% less than what one would obtain from end-wall pressure measurements which would sense the arrival of the interaction wave at the wall.

The interferograms of the present investigation substantiated end-wall pressure measurements which have been obtained at similar test conditions. An example of such an end-wall pressure history is given by the oscillogram in figure 14. This pressure trace was taken from reference 28 in which a pressure gauge of the Baganoff type<sup>(3)</sup> was used. The occurrence of events at the end wall and a comparison of measured to theoretical values are indicated in the figure. As will be noted again later, the discrepancy between theory and experiment for the pressure at 5E is in agreement with the present interferometric measurements and the relaxation times from these traces are in agreement with those reported here.

Another interesting feature of the flow field revealed by the interferograms of figure 12 is the occurrence of boundary layer separation behind the incident shock. This phenomenon, commonly called "bifuraction," results from the inability of the fluid in the incident boundary layer to negotiate the adverse pressure gradient presented by the reflected normal shock. This phenomenon

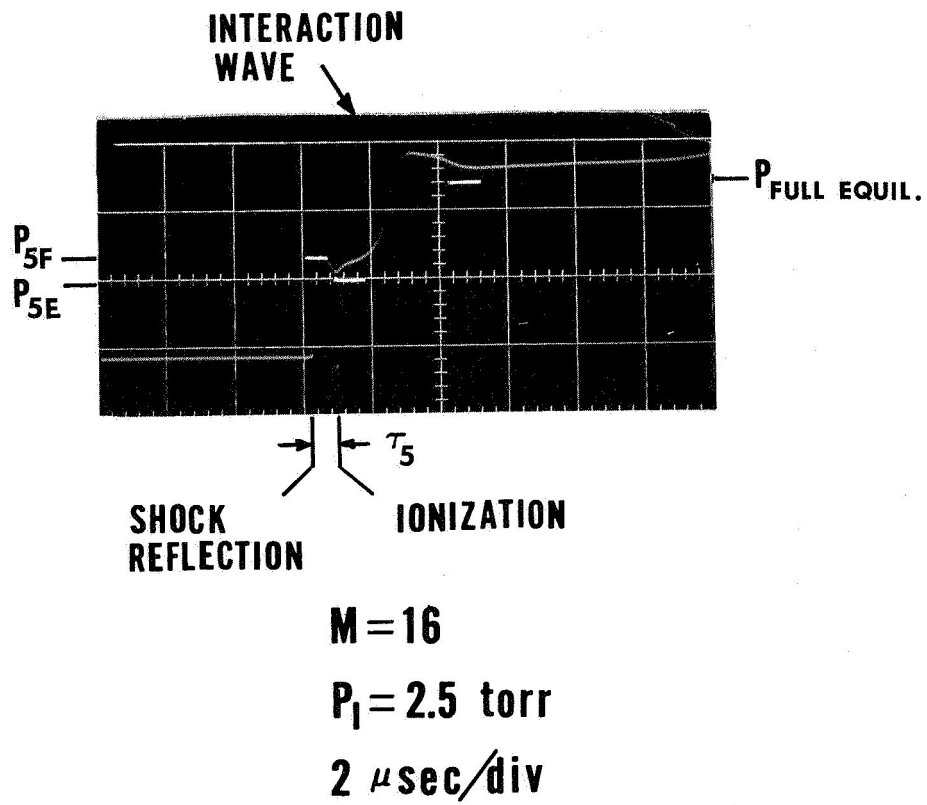


Figure 14. Oscillogram of pressure history measurement on shock tube end-wall for ionizing argon.

is also shown clearly by the snapshot interferogram of figure 15. A criterion for the occurrence of this momentum defect may be characterized by the ratio of the boundary layer stagnation pressure to the static pressure behind the reflected shock, relative to reflected shock fixed coordinates. When this ratio is less than unity, bifurcation will take place, as has been observed in the experimental and analytic studies of Mark<sup>(29)</sup> and Byron and Rott<sup>(9)</sup>. Reference 9 shows that the above criterion is strongly dependent on the gas properties behind both the incident and reflected shocks. In particular, the authors define the following two ratios:

$$\gamma_2 = \frac{h_2 - h_1}{e_2 - e_1}$$

$$\gamma_3 = \frac{h_3 - h_1}{e_3 - e_1}$$

where  $h$  and  $e$  are the specific enthalpy and internal energy respectively and the subscripts 1, 2, and 3 refer to initial, incident, and reflected shock conditions respectively. It may be noted that for a perfect gas, these expressions reduce to the ratio of specific heats. It is shown that bifurcation may be expected whenever  $M > 1.5$  and  $\gamma_3 < 1.5$ . It is also shown that bifurcation is more likely for a polyatomic gas for which  $\gamma_2$  is less than  $5/3$ , its value for a monatomic gas. Under the circumstances when the gas is monatomic and no ionization is present, bifurcation was not observed in either of references 9 and 29 or

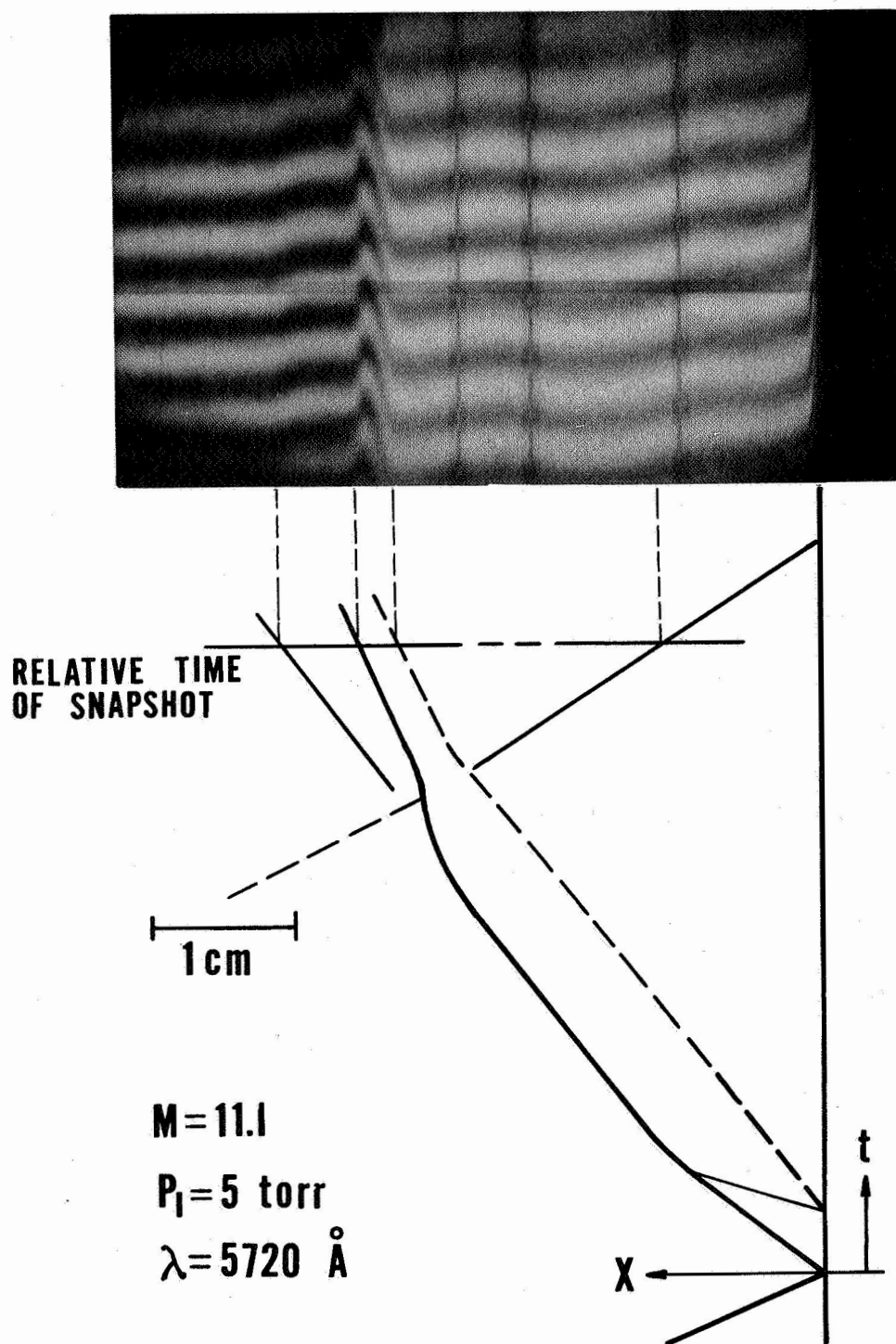


Figure 15. Snapshot interferogram showing reflected shock bifurcation in ionized argon.

reference 30. However, when a significant amount of nitrogen is added to the argon, bifurcation is readily observable. This is demonstrated by the interferograms of reference 9 and the several streak interferograms made in the present study for  $N_2$  and  $CO_2$  (see figure 18). The unusual occurrence of bifurcation in the present argon data is attributed to the presence of a significant amount of ionization behind both the incident and reflected shocks. This can be seen most readily when the appropriate expressions for an ionized monatomic gas are substituted into the above expressions for  $\gamma_2$  and  $\gamma_3$ , of Byron and Rott. For the equilibrium states corresponding to the conditions prevailing in figure 12, one obtains  $\gamma_{1,3} \cong 1.4 < 1.5$ . Because this change in properties and, hence, the reduction in  $P_{st}/P_3$  are associated with the onset of equilibrium in region 2, the bifurcation first occurs where the incident ionization front encounters the reflected shock as shown on the x-t diagram of figure 13.

The fact that the bifurcation effect seems to be propagating faster than the reflected shock is not inconsistent with the results of Mark<sup>(29)</sup> who showed that the bifurcation extended several boundary layer thicknesses into the flow and that its extent from the wall grows with the boundary layer thickness. Therefore, a simple geometric consideration will show that the leading edge of the bifurcation will travel faster than the reflected normal shock. This discussion of bifurcation phenomena may be summarized by the qualitative drawings in figure 16. The reader is reminded that bifurcation occurs on all four of the shock tube side-walls and that the interferograms represent a "view" normal to the side-wall of figure 16.

To summarize the discussions of the events which occur in the shock reflection process as the incident shock strength is increased, a series of

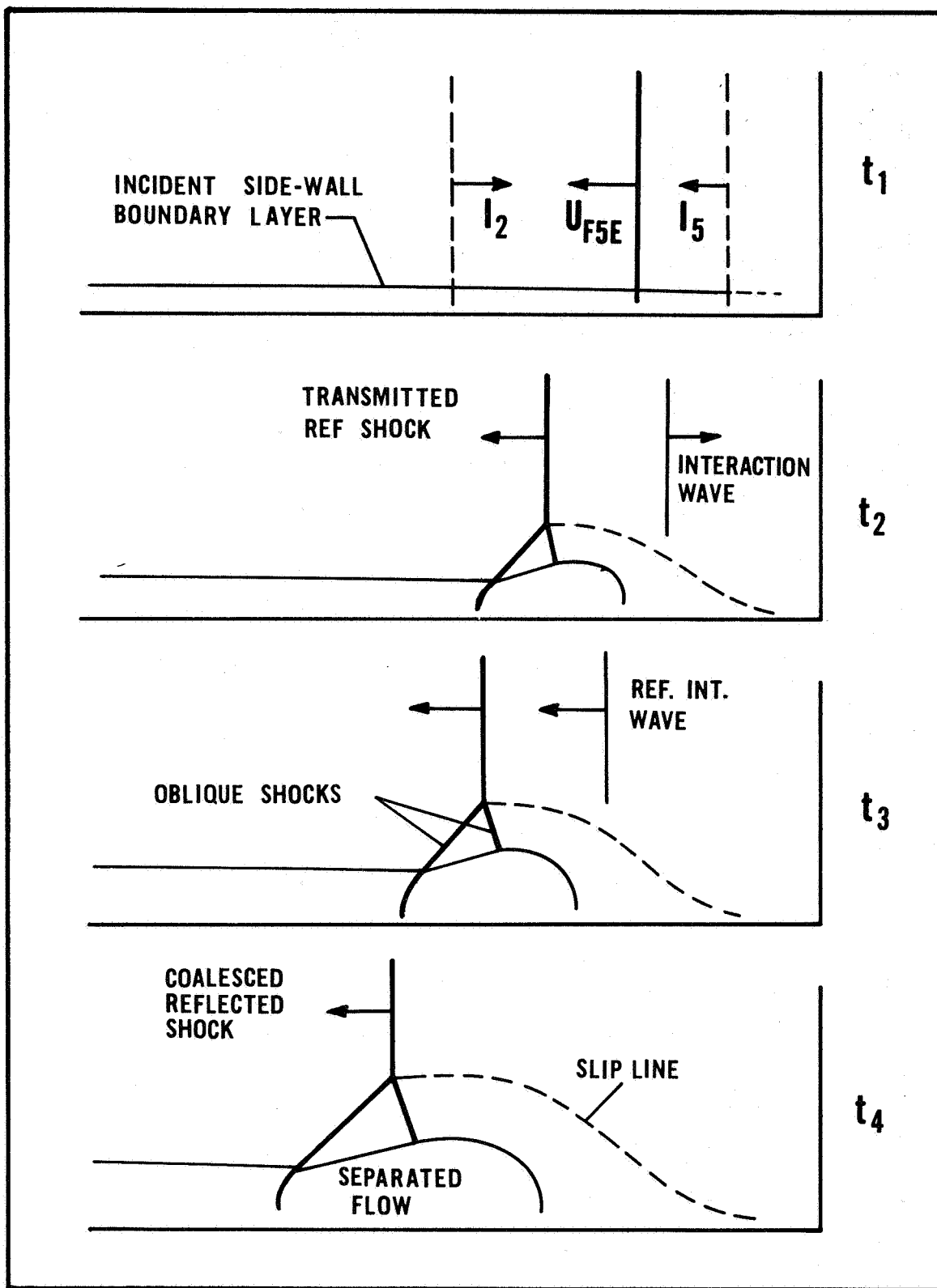


Figure 16. Schematic diagram illustrating onset and propagation of reflected shock bifurcation (argon).

interferograms with increasing Mach number at  $P_1 = 2$  torr is presented in figure 17. Unfortunately the incident shock was just missed in the  $M = 17.2$  case.

4.2 Comparison With Other Gases. As mentioned previously, several streak interferograms were obtained in gases other than argon. These results are presented here only to illustrate qualitatively some of the similarities and differences in the reflection processes.

Six runs made with xenon showed that the shock reflection process was basically similar to that for argon. It was noted, however, that the expansion wave resulting from the equilibration behind the reflected shock was not the only dominant factor causing the deceleration of the reflected shock. In fact, the gradual curvature of the reflected shock trajectory almost immediately after reflection supports Smith's<sup>(2)</sup> contention that the deceleration of the reflected shock is due at least partly to the heat sink effect of the ionization process which is occurring throughout the flow field in the reflected shock region. This effect, as noted earlier, is more noticeable in xenon than in argon. Figure 18 (a) shows one of the streak interferograms obtained in xenon. The relaxation times,  $\tau_5$ , measured from the xenon interferograms were compared to Smith's correlation obtained with pressure measurements and were found to be approximately 1.5 times larger. This discrepancy may be attributed to a slight difference in defining  $\tau_5$  and to the fact that the present measurements were made at considerably higher initial pressures and lower Mach numbers. An inadequate number of data points were obtained here to make any formal comparisons.

Interferograms were also obtained in  $N_2$  and  $CO_2$  and are shown in figure 18 (b) and (c). These interferograms illustrate vibrational and



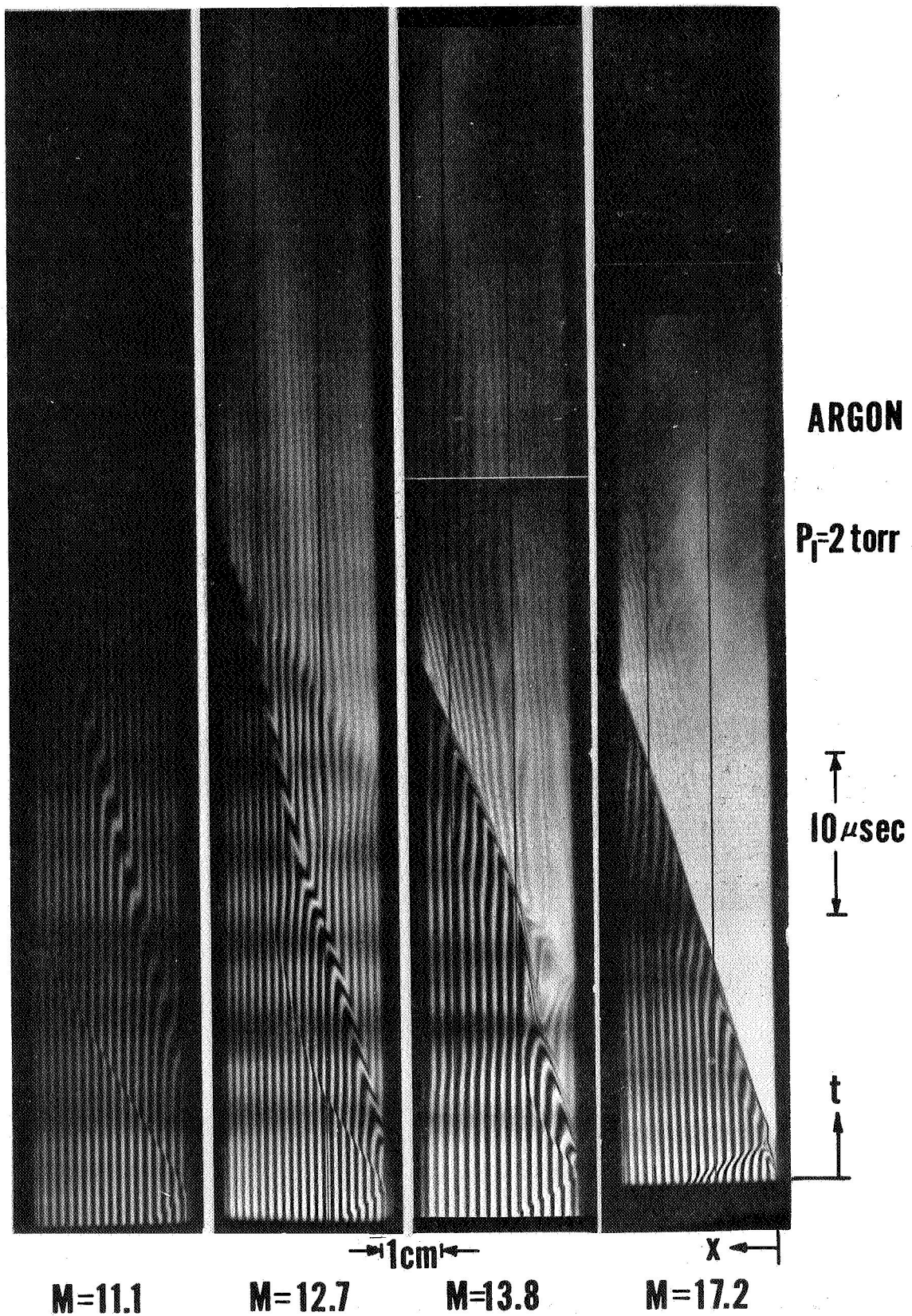


Figure 17. A series of streak interferograms in argon for  $P_1 = 2$  torr and increasing Mach number.

$P_i = 5 \text{ torr}$

$10 \mu\text{sec}$

(a)

(b)

(c)

$1 \text{ cm}$

**Xe**  
**M=9.7**

**N<sub>2</sub>**  
**M=6.2**

**CO<sub>2</sub>**  
**M=6.7**

Figure 18. Streak interferograms of the shock reflection process in a) xenon, b) nitrogen, and c) carbon dioxide.

chemical nonequilibrium behind the reflected shock as can be seen by the fringe shift to the right in (b) and the nonuniformity in (c). (Note: in figure 18 (b), the interferometer is adjusted so that fringes shift to the right for an increase in refractivity in opposition to all the other interferograms which have been shown here.) Reflected shock bifurcation is visible for both  $N_2$  and  $CO_2$  practically immediately after reflection. This is as one would expect from the discussion in the last section which was based on the results of Byron and Rott<sup>(9)</sup>. Since the actual reflected shock speed in the presence of bifurcation may be appreciably less than the theoretical speed, the interpretation of measured reaction rates using sensors on the end wall should include this effect. In particular, the reflected shock temperature jump will be different than expected and particle paths behind the incident shock will not intersect the reflected shock at the predicted space-time coordinate of an x-t diagram.

4.3 Time History of Thermodynamic Properties. The streak interferograms of the preceding discussions and others like them have provided a means of obtaining quantitative measurements of the time history of the mass density and electron concentration behind the reflected shock. For reasons which will be indicated, these measurements are restricted to one distance from the wall and at the occurrence of particular "events" or relatively long times after reflection where the flow field was apparently uniform. In particular, it was not possible to measure the thermodynamic properties during the approach to the equilibrium state 5E. Therefore, the interpretation of the relaxation data obtained from the interferograms remains somewhat incomplete, but the applicability of the data to other shock tube investigations or to the study of ionization relaxation in argon or other monatomic gases remains unaffected.

The thermodynamic data will be presented in section 4.3.2 and the relaxation data are presented in the following section along with a correlation of the results.

4.3.1 Approach to Ionization Equilibrium. The production of electrons subsequent to the initial passage of the translational or frozen shock wave is generally agreed to take place through a series of distinct regimes wherein different reactions dominate. <sup>(4, 5, 6)</sup> This description of the approach to equilibrium renders the theoretical interpretation of a "relaxation time" difficult. However, in argon or the other monatomic gases, the onset of equilibrium is quite sudden and distinct and therefore the measurement of a characteristic or total relaxation time is greatly facilitated because of its simplicity of experimental definition. In particular, for interferometric measurements, the attainment of full equilibrium, where the net rate of production of ionized species is zero, is indicated by a sharp change in the slope of the fringes. For the present experiments, the relaxation times  $\tau_2$  behind the incident shock and  $\tau_5$  behind the reflected shock are defined respectively as the times to reach full equilibrium after passage of the incident shock and after shock reflection.  $\tau_5$  is measured from the streak interferograms by extrapolating the "back edge" of the ionization front,  $I_5$ , to the wall and measuring the distance ( $\tau_5 = \text{distance}/V_w$ ) of this extrapolated point from the point where the reflected shock leaves the wall. This is a direct measure of the so called particle time because the particle speed is zero adjacent to the wall.  $\tau_{2L}$ , the incident relaxation time in laboratory fixed coordinates, is obtained by extrapolating the rear edge of the incident shock ionization front,  $I_2$ , to the wall and measuring the distance from the point of reflection to this extrapolated point. The measurement of  $\tau_{2L}$  is

undoubtedly less precise than that of  $\tau_5$ . This is partly responsible for the scatter exhibited in the incident shock data presented below. As a consequence of transforming from a laboratory observation to an observation made relative to the particles, the actual "residence" or particle time is defined as

$$\tau_{2P} = \int \frac{\rho_2}{\rho_1} dt_L$$

Since the present measurements do not provide the necessary density history for the evaluation of this integral, an estimate of the particle time  $\tau_2$  was made by the following equation:

$$\tau_{2P} = 1.2 \left( \frac{\rho_{2F}}{\rho_1} \right) \tau_{2L}$$

The factor 1.2 is introduced to account for density increase between the shock and the attainment of equilibrium. <sup>(5)</sup> Smith <sup>(2)</sup> found this factor was more like 1.1 for case of xenon. With this correction applied, the particle relaxation times are plotted in figure 19 in the form of  $P_1 \tau$  vs.  $1/T_F$  where  $T_F$  is the theoretical frozen temperature behind either the incident or reflected shock depending on the indicated origin of the data point. The incident shock results of Wong and Bershader <sup>(5)</sup> and Petschek and Byron <sup>(4)</sup> are also included for comparison where the laboratory times presented have also been corrected by the above formula to obtain particle times. It is not clear that this is the proper correction to use for Petschek and Byron's data since their results were based on radiation measurements, and they measured  $\tau_{2L}$  from shock passage to

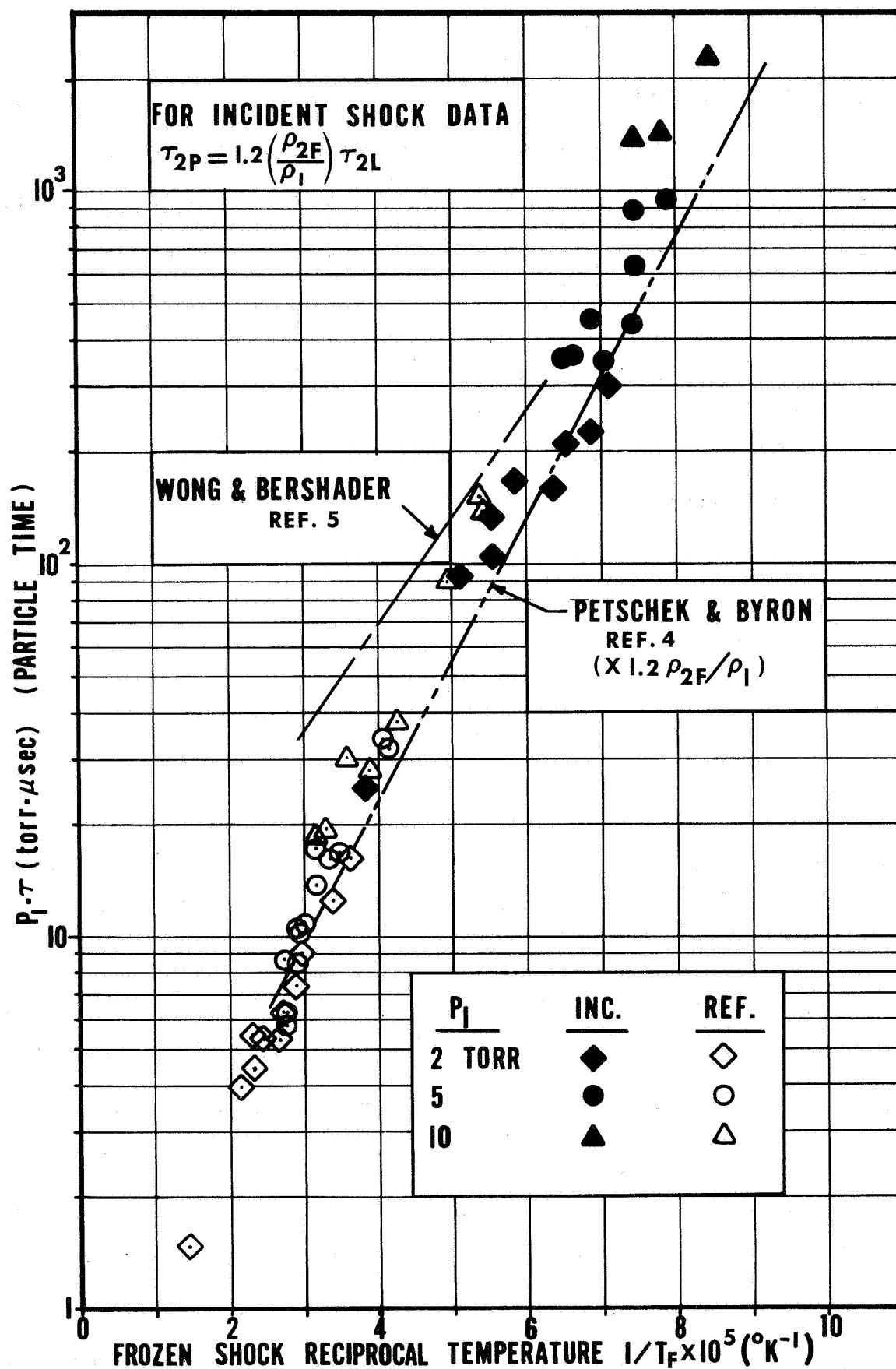


Figure 19. Ionization-relaxation particle times behind incident and reflected shocks in argon.

the point where the radiation intensity was half of its peak value. This fact partially explains the longer times represented by the present data.

That this data should so closely form a single straight line on the semi-log plot is remarkable when it is recalled that there are several reactions which sequentially dominate the approach to equilibrium. For example, in reactions resulting from atom-atom collisions, one might expect to observe a  $1/P_1$  dependence of the parameter  $P_1^{\tau}$ ; whereas for reactions involving electron-atom collisions, the temperature used in the correlation should be the electron temperature, which would be closer to the equilibrium gas temperature. (2, 5) However, use of this latter temperature would also introduce a  $P_1$  dependence. It is noted also that the frozen temperatures considered here range between 14000 and 70000°K and initial pressures between 2 and 10 torr.

It may be noticed that there does appear to be a slight difference between the incident and reflected shock data. The incident shock data shows considerably more scatter. This is quite probably caused by the greater effect of impurities on the reactions in the early stages of the equilibration process. (4, 6) The reflected shock data on the other hand, has relatively little scatter and appears to have a steeper slope (i.e., a higher activation temperature for the composite reaction rate) than the incident data. This might result, for example, if a greater portion of the equilibration is due directly to electron-atom ionizing collisions ( $T_{\text{Act}} = 15.75$  ev) and less to atom-atom inelastic collisions which raise one of the atoms to an excited state ( $T_{\text{Act}} = 11.5$  ev) followed by ionization. This hypothesis is supported to some extent by the results of the next section where it is shown that unlike the incident shock, there are already a measureable number of electrons present immediately behind the frozen

reflected shock.

In his work on xenon, Smith<sup>(2)</sup> proposed a correlation of the form

$$P_1 \tau \sim \frac{\left(\frac{E_1}{k T_{5E}}\right)^{3/2} \exp\left(\frac{E_1}{k T_{5E}}\right)}{\left(\frac{E_1}{k T_{5E}} + 2\right)}$$

in which  $E_1$  is the first excited state and  $T_{5E}$  is the temperature corresponding to region 5E. The apparent success of this correlation may have only been fortuitous since this correlation parameter is strongly dependent on the initial pressure,  $P_1$ . Most of his data was taken at  $P_1 = .5$  torr, and this pressure was used in determining  $T_{5E}$  for use in the correlations. However, the present results and Smith's  $P_1 \tau$  data at other initial pressures showed little dependence on  $P_1$ . The present measurements of the thermodynamic properties at 5E in argon also show that the simple theoretical properties are in disagreement with the measured ones. The question arises then as to the correct value of  $T_{5E}$  to use in such a correlation.

No attempt is made here to explain the behavior of the experimental data in terms of theoretical reaction rates. For the present, the data is given only as a correlation useful in designing and performing other shock tube experiments in which the times to attain equilibrium are of interest.

If one chooses to draw a single straight line through all the experimental results of figure 19, the following equation is obtained:

$$P_1 \tau = .59 \exp\left(\frac{97000}{T_F}\right)$$



Transforming this data back to the original data plane results in figure 20 which is more convenient for engineering application.

4.3.2 Thermodynamic Properties. As mentioned earlier, it was not possible to obtain simultaneous interferograms at two wavelengths. It was also not possible to obtain interferograms of 100  $\mu$  sec duration--the time at which the boundary layer measurements were to be made. Because of these difficulties, it was necessary to obtain a series of interferograms for the first 40  $\mu$  sec after reflection and another series starting at 40  $\mu$  sec. By crossplotting the results, the fringe shift at each of two wavelengths, a particular Mach number, and an initial pressure could be obtained. Figure 21 shows two interferograms at approximately the same conditions where the one on the left extends to 40  $\mu$  sec and the one on the right is an interferogram extending from 40  $\mu$  sec to 100  $\mu$  sec. The fringe shifts from 40 to 100  $\mu$  sec are also plotted versus Mach number and simply added to the measured shifts at 40  $\mu$  sec.

The reference conditions for these streak interferograms are the initial undisturbed test conditions, so that the electron concentrations and mass density are obtained from the simultaneous solution of

$$S_{1,2} = \frac{(\mu_{1,2}-1)_0}{\rho_0} \frac{L \rho_1}{\lambda_{1,2}} \left\{ \left( \frac{\rho}{\rho_1} - 1 \right) - n_e m_A \left[ 1 - \frac{a^+}{a^0} + \frac{1}{m_e a_{1,2}^0} \left( \frac{e^2 \lambda_{1,2}^2}{\epsilon_0 16 \pi^3 c^2} \right) \right] \right\}$$

The following equations result from this solution:

$$\rho = \rho_1 + (1.486 S_1 - 1.187 S_2)(10^{-4})$$

$$n_e = (1.574 S_1 - 2.021 S_2)(10^{17})$$

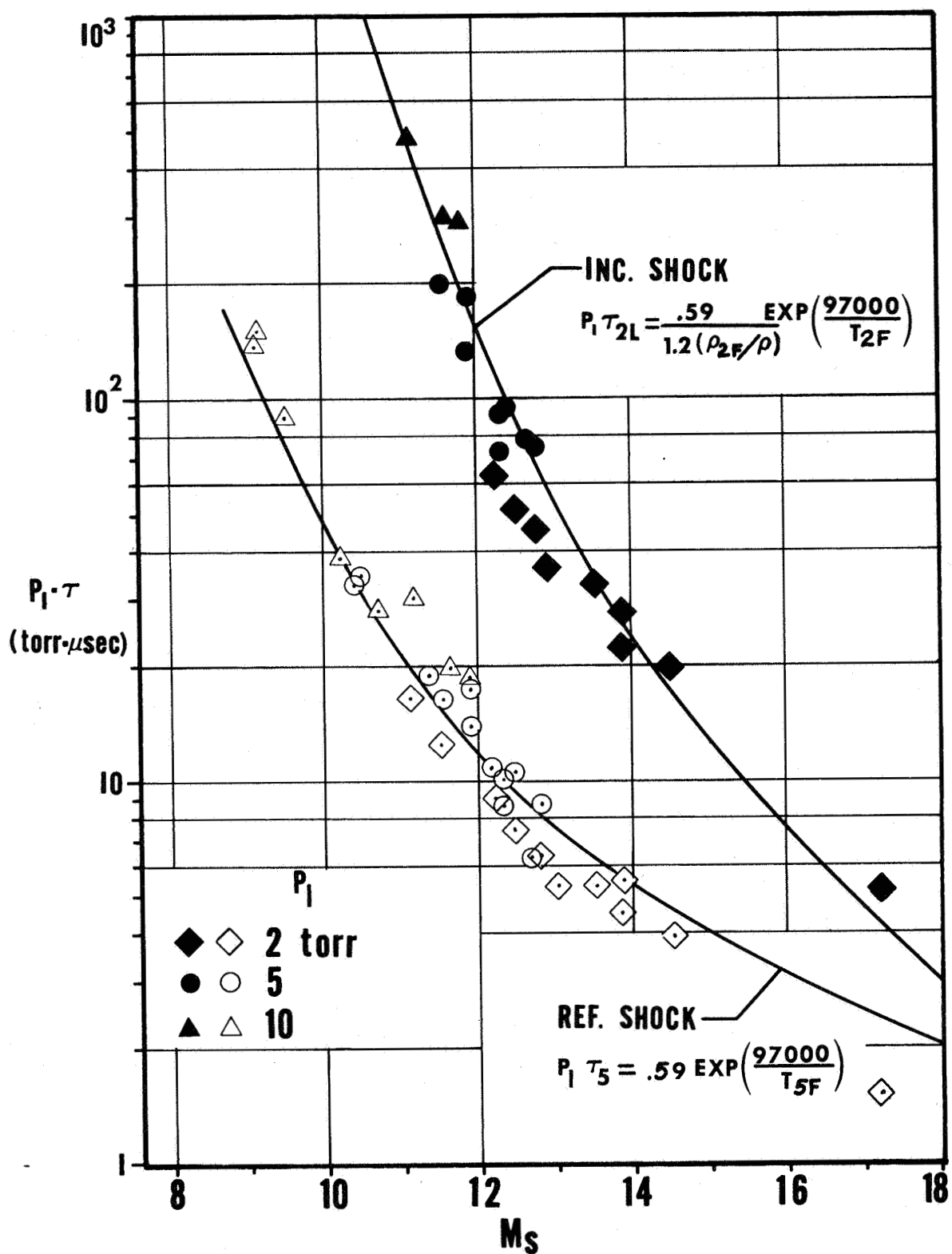


Figure 20. Ionization-relaxation laboratory times behind incident and reflected shocks in argon.

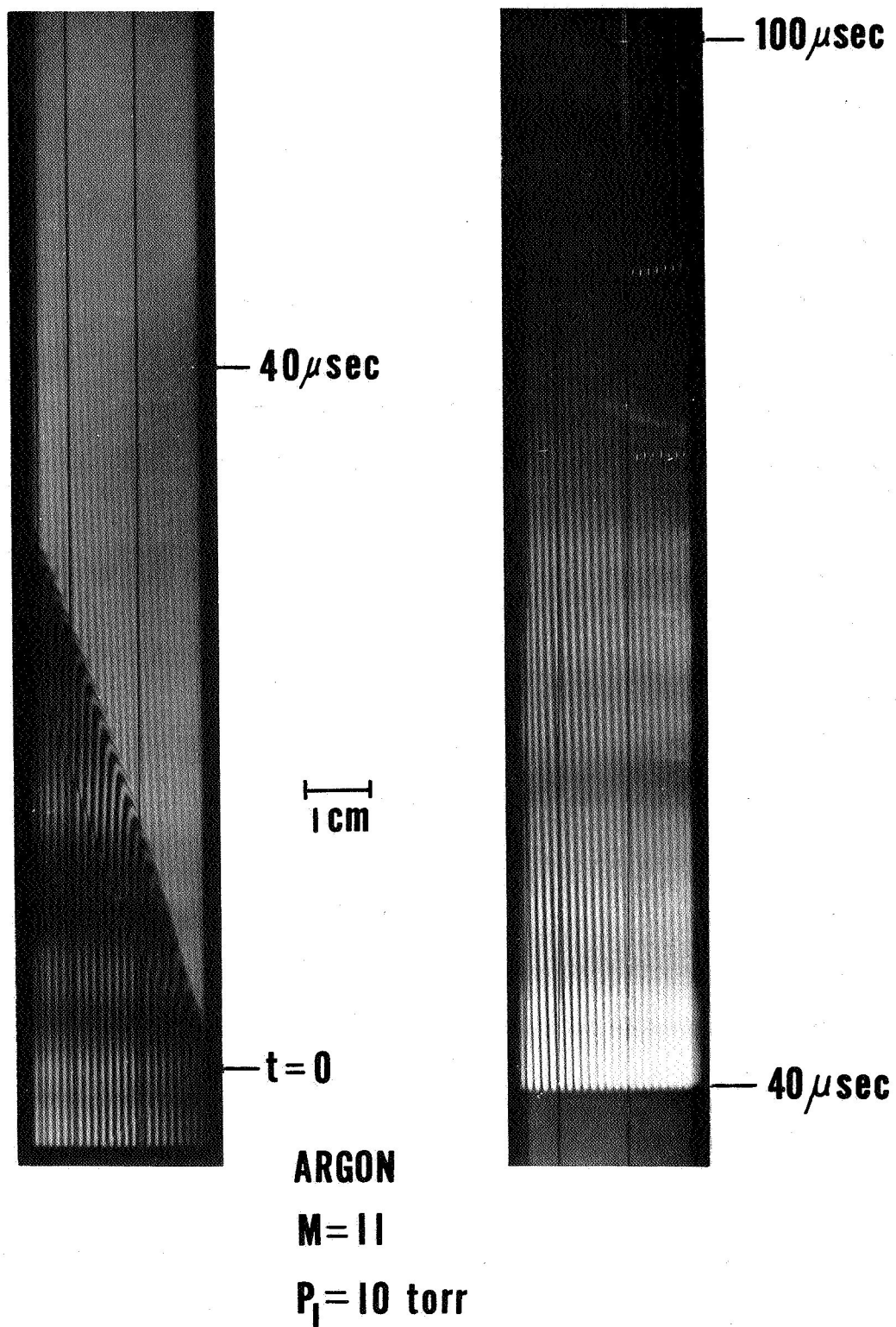


Figure 21. Streak interferograms of shock reflection process extending to 100 microseconds after reflection (argon).

Some of the fringe shift data are plotted in figures 22, 23, and 24. It is again noted that the measurements are all made at 4 mm from the end wall where, for all the conditions considered here, the reflected shock was still straight. Measurements of the conditions in 5E at larger distances from the wall, say 7 or 10 mm, showed better agreement between theory and experiment by about 5 to 10% . However, at these larger distances from the wall, the flow may or may not have passed through a straight shock, depending on how strong the incident shock was. Because of this "unsteadiness," considerably more data points should be required. In addition, the time scale of the reflected shock structure for the stronger incident shocks is determined by the incident shock relaxation times, which exhibit a significant amount of scatter. Thus, the gas properties in region 5E at a larger distance from the wall may result from the processing of different reflected shock speeds for the same incident shock Mach number. Furthermore, side-wall, boundary-layer interactions and contributions to the fringe shift are larger for larger distances from the end-wall, hence longer times after reflection. Because of all these effects, the cross plotting technique would not have been successful at larger distances from the wall.

In figure 22 the theoretical fringe shifts represented by the dashed lines show an obvious discrepancy across the frozen reflected shock wave. This discrepancy is well outside the estimated uncertainty in reading the fringe shifts and is due to the presence of a measurable number of electrons immediately behind the "frozen" reflected shock. It may be recalled that this

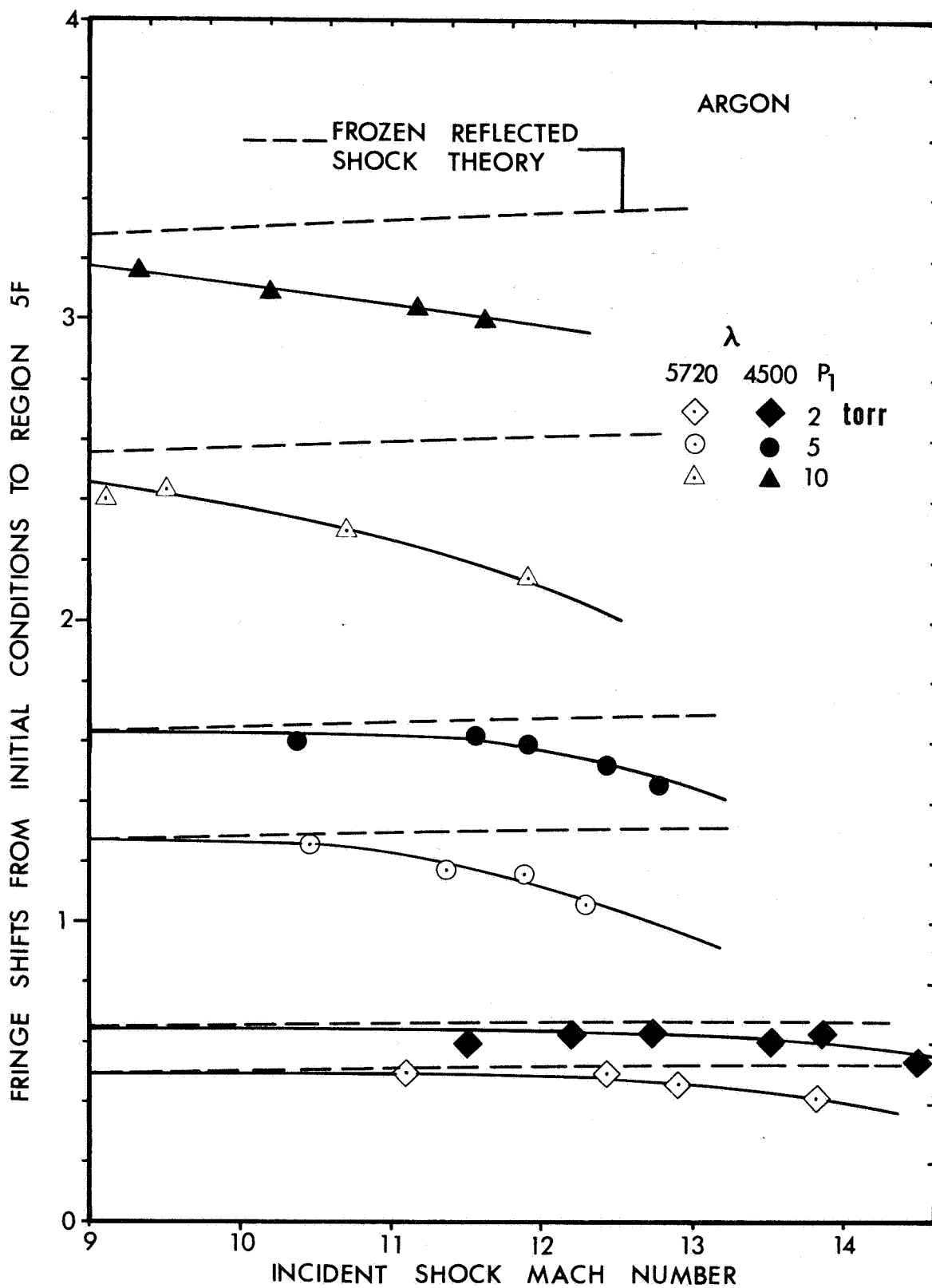


Figure 22. Measured and theoretical fringe shifts from initial conditions to frozen reflected shock conditions.

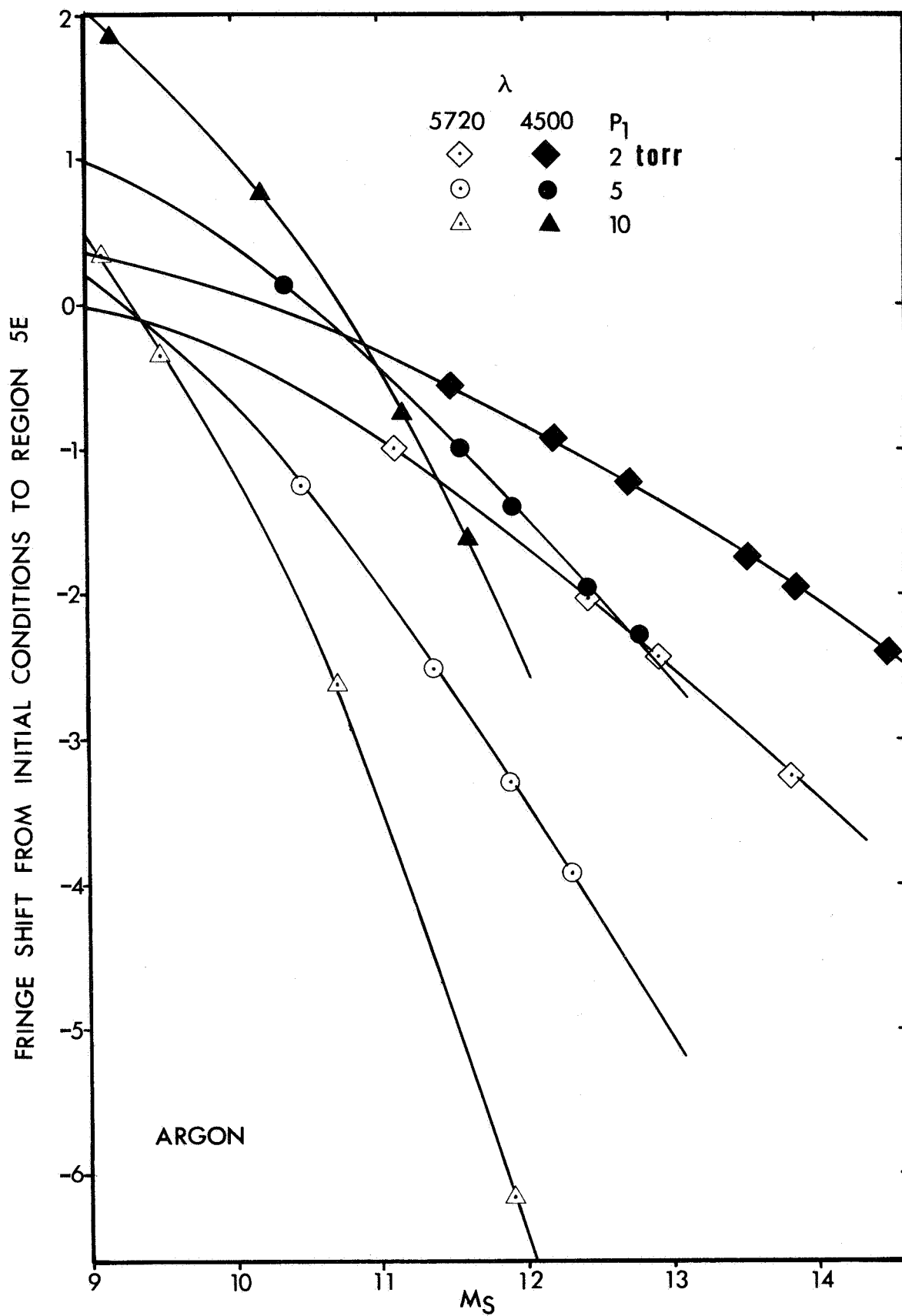


Figure 23. Measured fringe shifts from initial conditions to reflected shock equilibrium conditions.

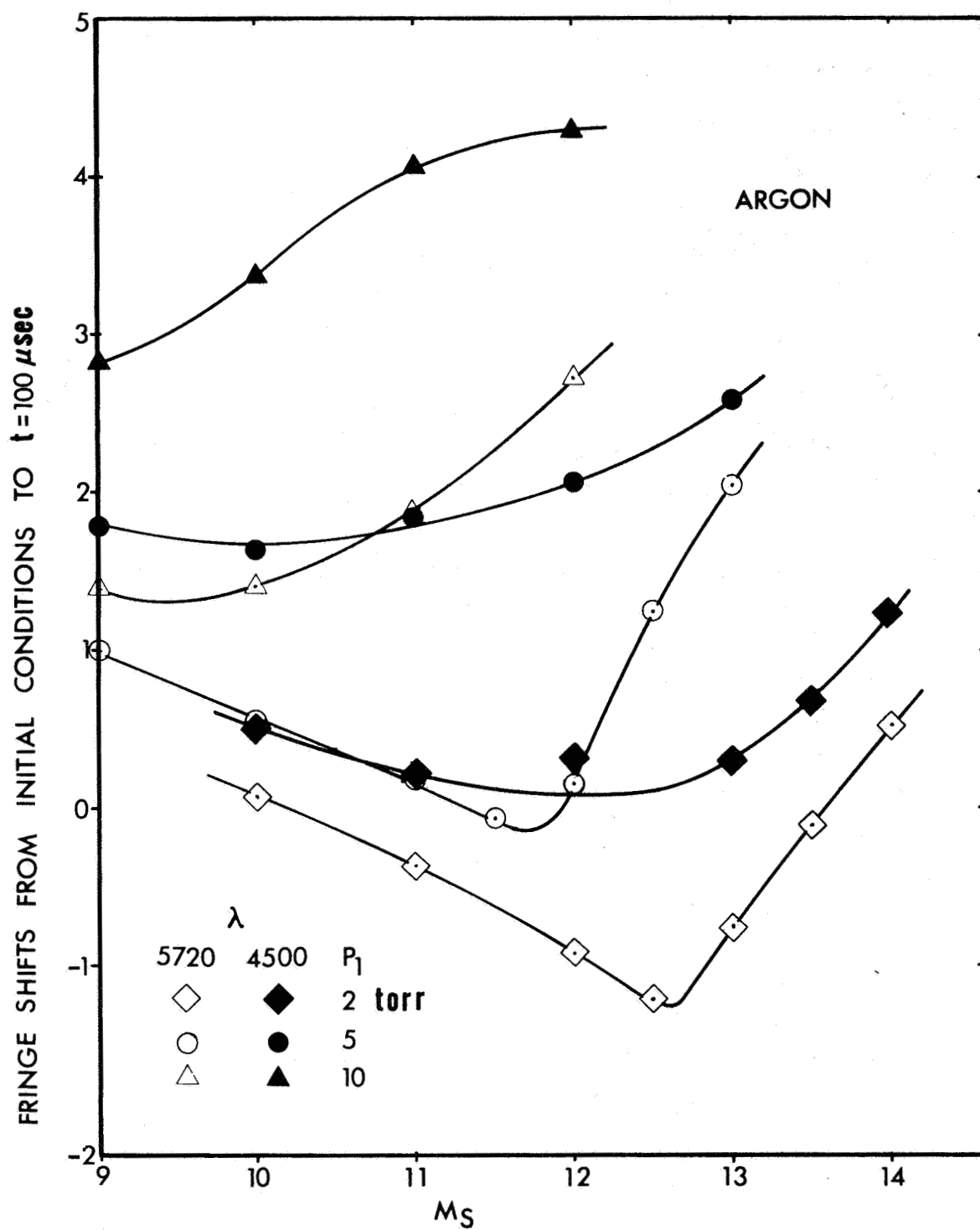


Figure 24. Measured fringe shifts from initial conditions to reflected shock conditions at 100 microseconds after reflection.

was mentioned in the preceding section as being a partial cause of the slight difference between the activation temperatures for the incident and reflected shock relaxation data. The measured electron concentrations in region 5F are presented in figure 25. The experimental uncertainty in these measurements is quite large, but the magnitude of the difference in fringe shifts from the theoretical should convince the reader that the electronic contribution is responsible for the difference. These large electron concentrations are also responsible for the erratic behavior of thin-film heat-transfer measurements immediately after shock reflection for Mach numbers of the present magnitude.

The measured mass densities for region 5F are given indirectly in figure 26 where the measured speed of the frozen reflected shock,  $U_{5F}$ , and the speed calculated by substituting the measured densities into the equation

$$U_{5F} = \frac{\left( \frac{\rho_{2F}}{\rho_1} - 1 \right)}{\left[ \frac{\rho_{5F}}{\rho_1} - \frac{\rho_{2F}}{\rho_1} \right]}$$

are compared with the purely theoretical speed. In accord with the results of references 25, 29, and 30, the measured speed  $U_{5F}$  is less than the theoretical value. Substitution of the measured densities yields speeds which exhibit the same trend as the measured speeds but are not as low. This is not disturbing since the uncertainty in  $\rho_{2F}/\rho_1$  (10%) and  $\rho_{5F}/\rho_1$  (5%) produce a large enough uncertainty in  $U_{5F}$  (21%) to encompass the directly measured speeds.

The measured densities and electron concentrations in region 5E are shown in figures 27 and 28 and the resulting temperatures and pressures obtained by assuming equilibrium and a Debye-Huckel Saha equation (see Appendix B)



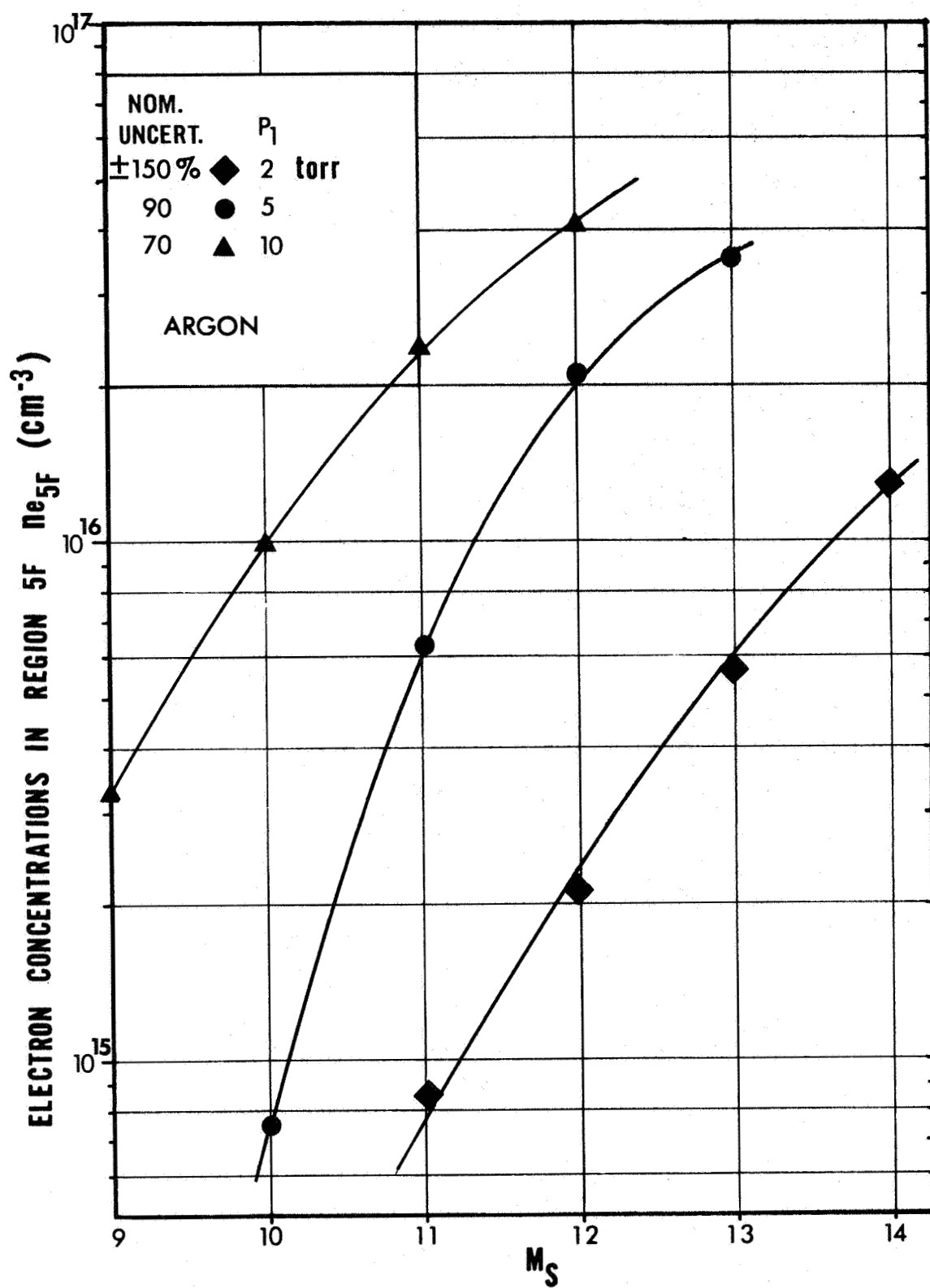


Figure 25. Measured electron concentrations in the frozen reflected shock region 5F.

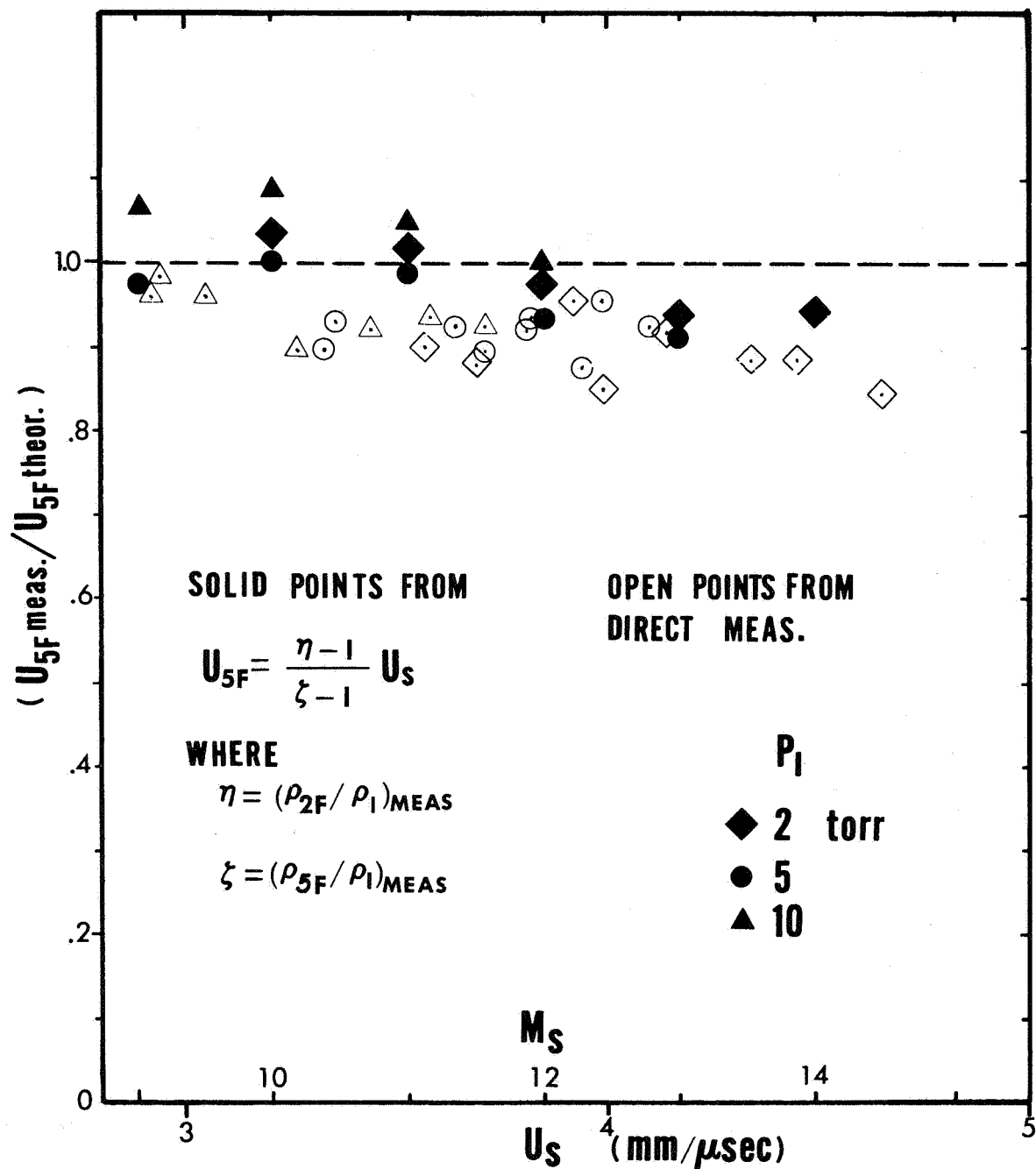


Figure 26. Comparison of measured and theoretical frozen reflected shock speed  $U_{5F}$  (argon).

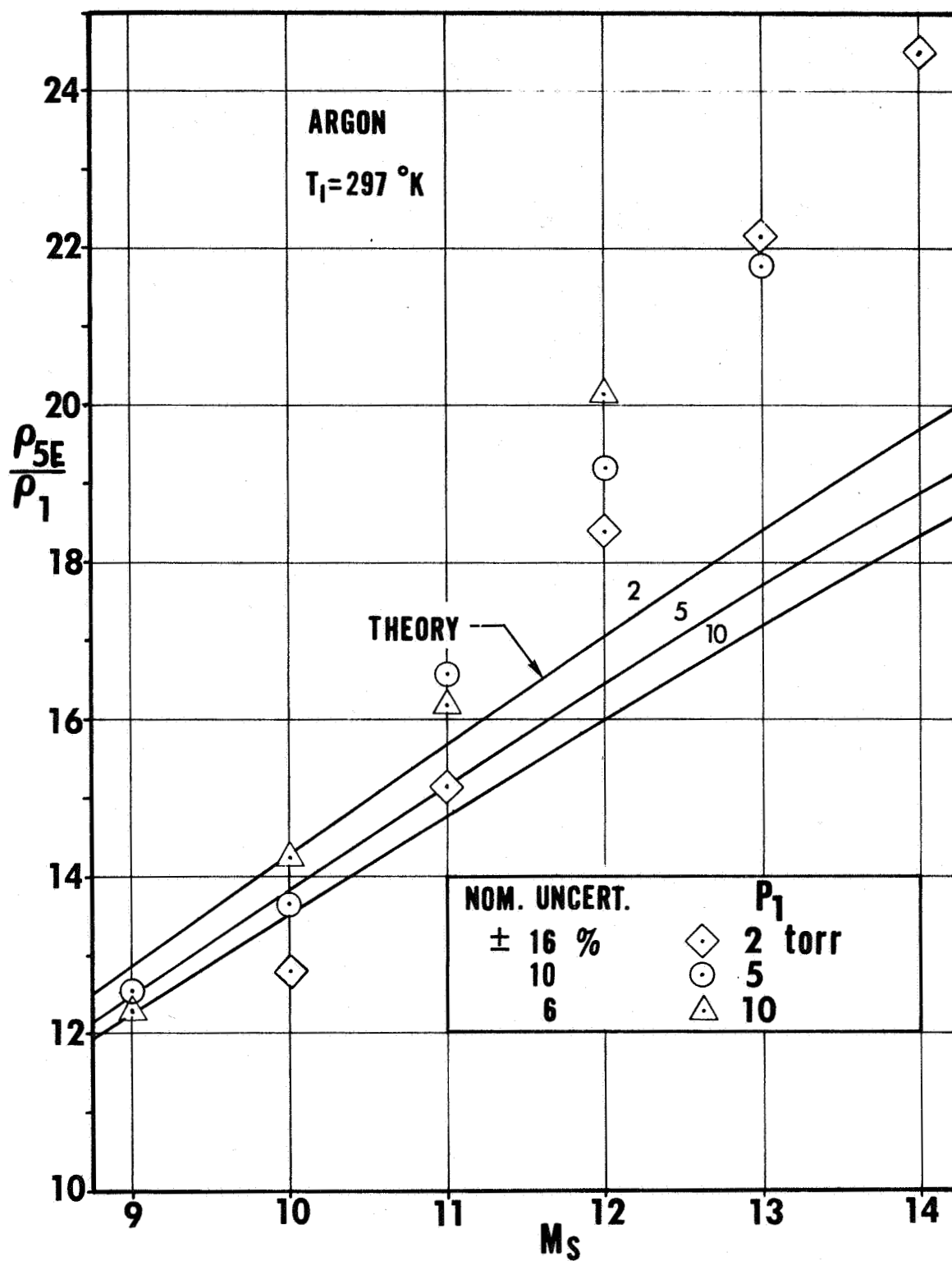


Figure 27. Reflected shock mass densities at equilibrium in region 5E.

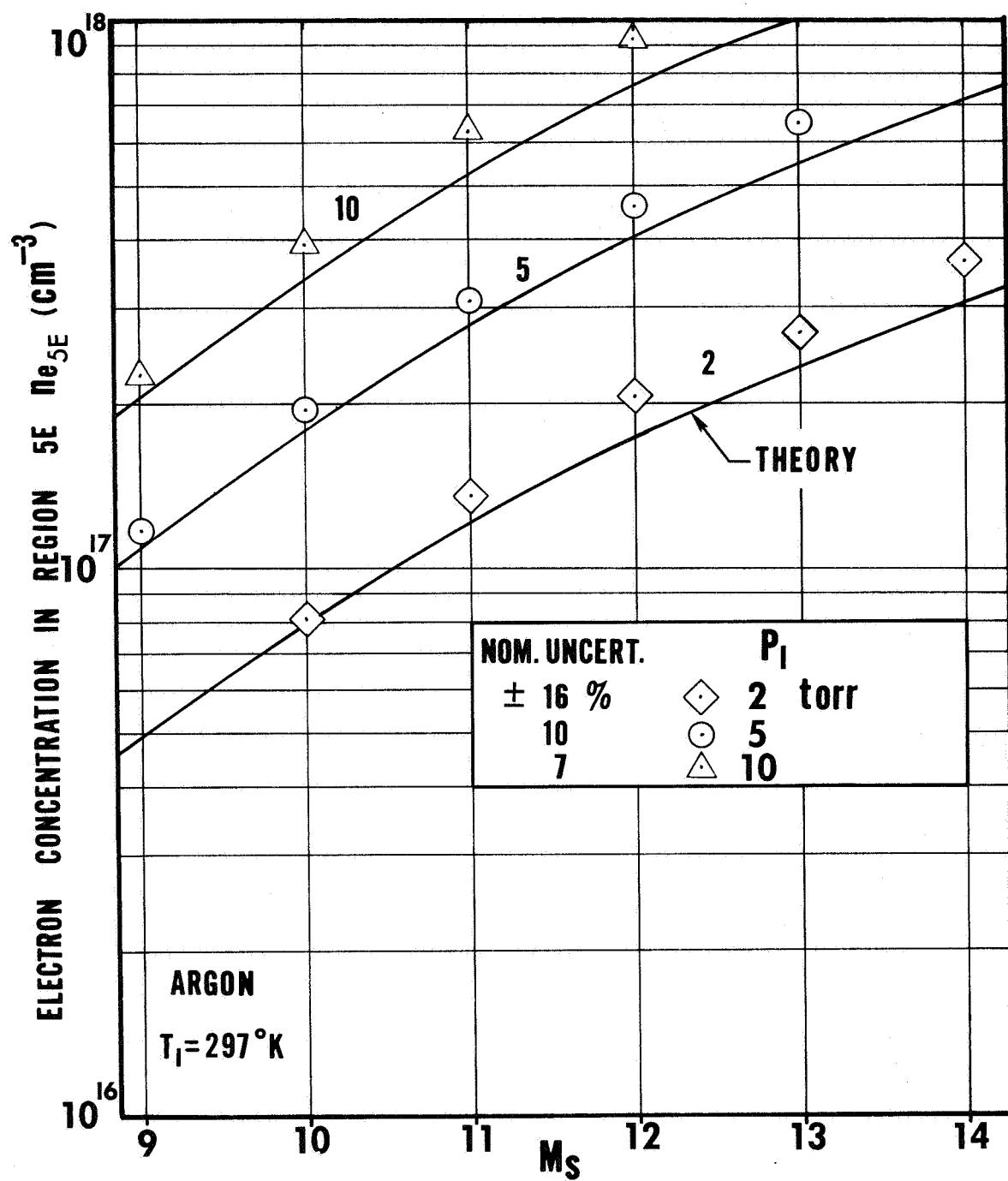


Figure 28. Reflected shock electron concentrations at equilibrium in region 5E.

are shown in figures 29 and 30. Included in these figures are the results obtained from the one dimensional equilibrium calculations given in Appendix B where the Debye-Hückel model is used. In the calculations of Appendix B, several forms of the Saha equation have been employed in order to give a measure of the various lowerings of the ionization potential resulting from electrostatic effects. The Debye-Hückel model was selected for comparison with experiment because of its internal consistency and because it satisfies certain limiting conditions as discussed in the appendix.

It will be noted that the measured properties are all higher than the theoretical ones. This not explainable in terms of experimental uncertainties or systematic errors. An example of a systematic error is that the side-wall boundary layer may be affecting the results to some extent, but if it were a significant factor, the electron concentration would be too low while the density would be too high. The explanation for the discrepancy, rather, lies in the "unsteadiness" of the actual reflection process. By considering the following sketches, one can see from (a) that the mass density in 5E is determined relative to the initial density by the expression  $\rho_{5E} = (x_1/x_{5E})\rho_1$ . The term "quasi-steady" has been applied to the theoretical calculations depicted by the model in sketch (b) because it assumes a constant reflected shock speed.

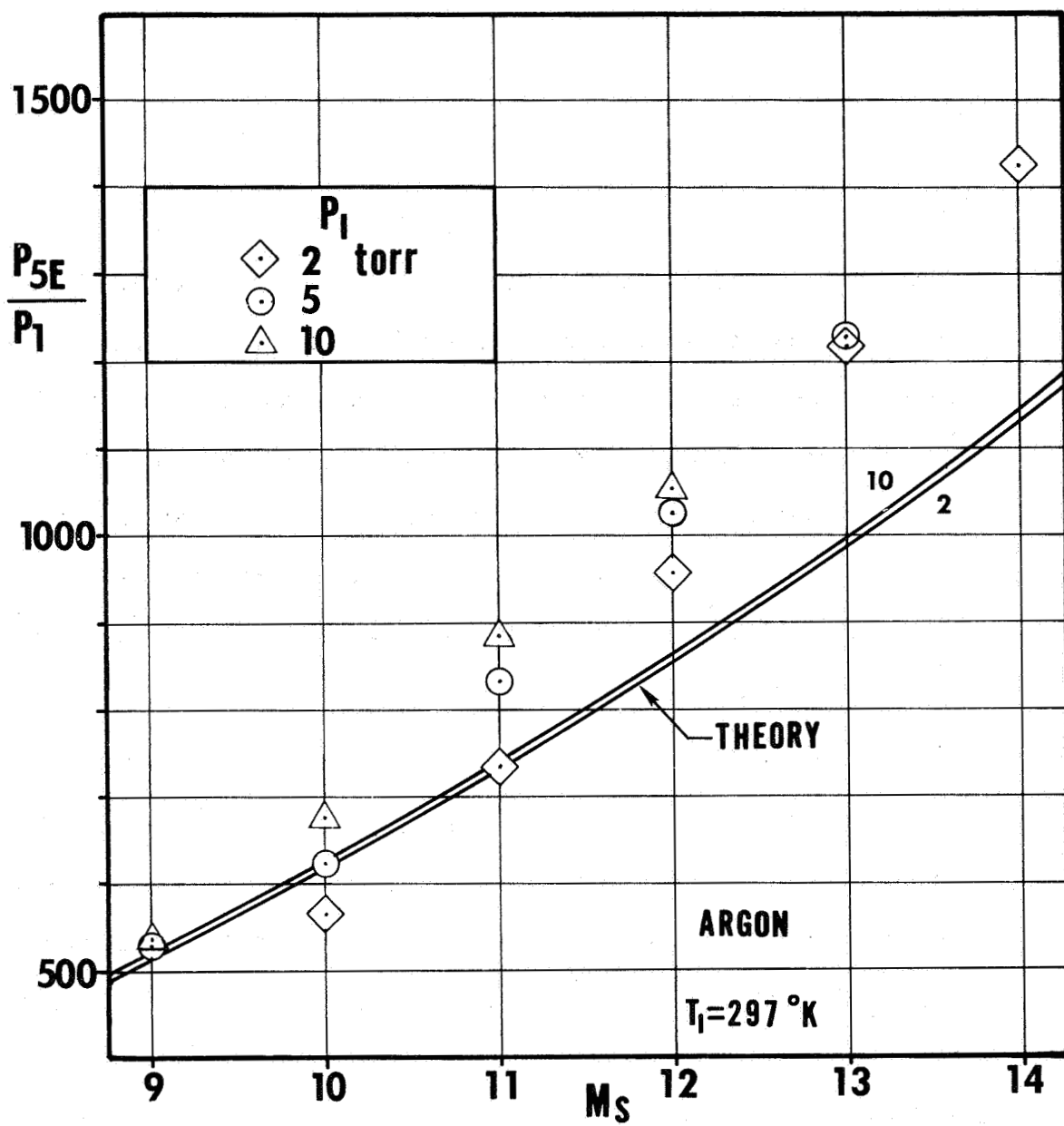


Figure 29. Reflected shock pressures at equilibrium in region 5E.

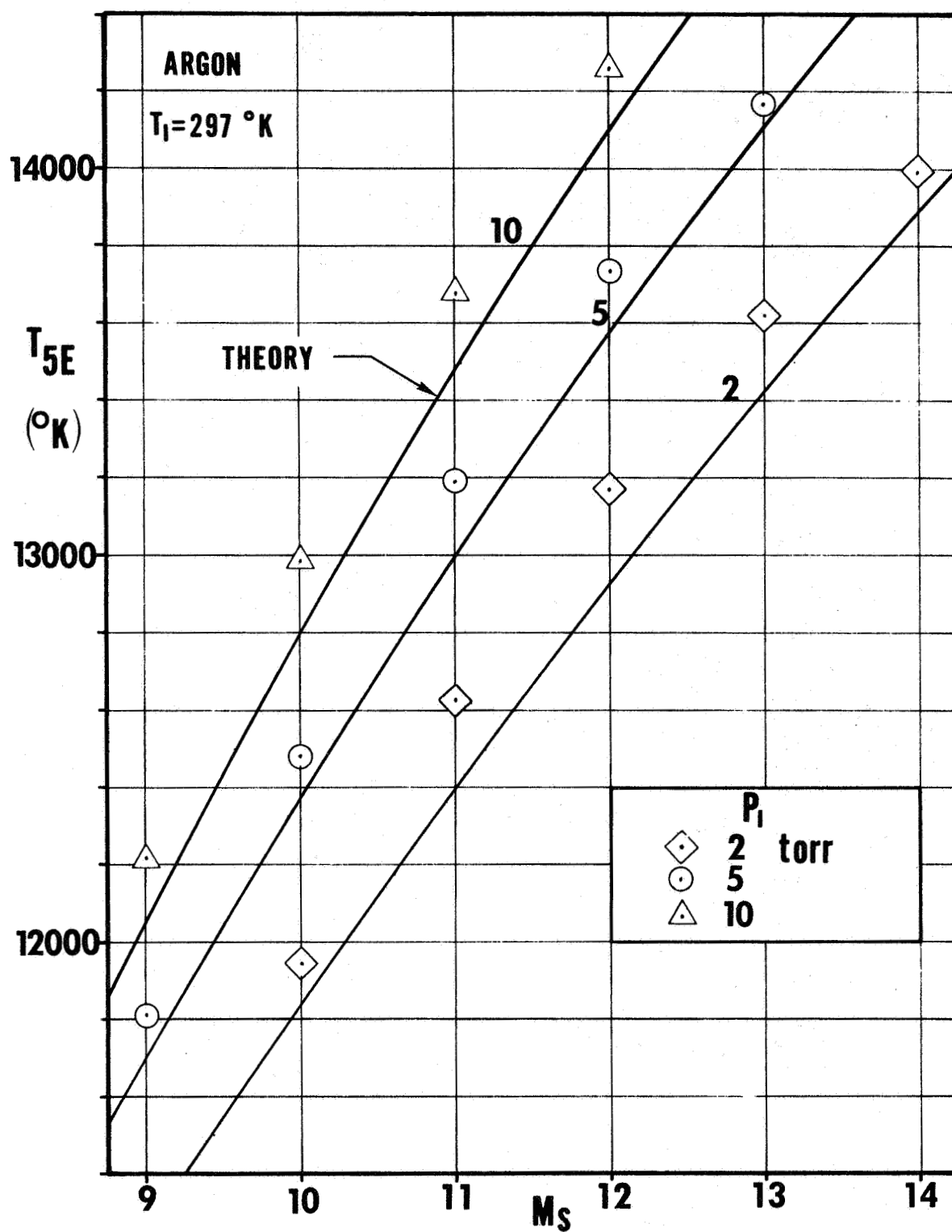
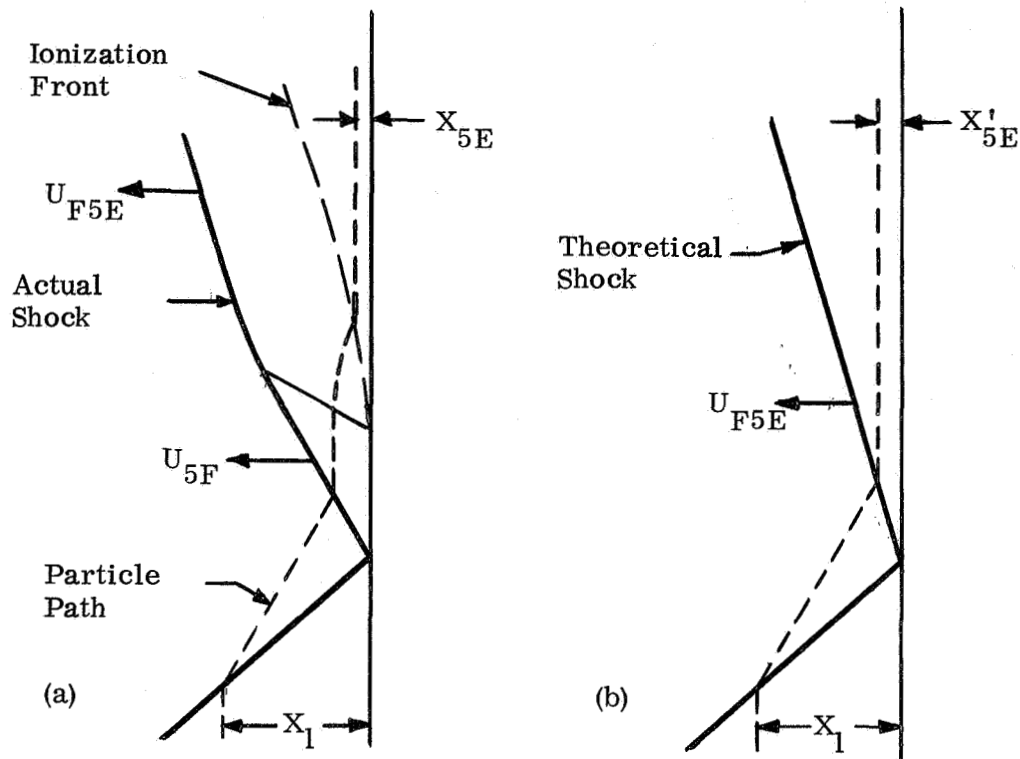


Figure 30. Reflected shock temperatures at equilibrium in region 5E.



Since the velocity next to the wall must be zero from the instant of reflection, there is no relaxation zone in the theoretical model, and the particle paths are as shown. For the same distance  $x_1$ , the distance  $x_{5E}$  is less than  $x'_{5E}$  reflecting the higher density in the actual case. Without these considerations, however, the fact that the gas is processed by a stronger shock,  $U_{5F}$ , than the slower theoretical shock speed corresponding to frozen conditions in 2 and equilibrium in 5 should lead one to anticipate a higher than theoretical density.

The comparison that was made with end-wall pressure measurements in figure 14 showed that the higher than theoretical pressures obtained in the present study are substantiated by the pressure traces. The magnitude of the discrepancy between the experiment and simple theory is also in good agreement between the present diagnostic technique and the pressure measurements. Specifically, the theory is approximately 13% below the pressure



measurement and approximately 15% below the interferometric measurements.

The fringe shifts at 40 and 100  $\mu$ sec after reflection exhibit a rather unexpected behavior. In figure 24, for example, the fringe shifts at 100  $\mu$ sec are shown to attain a minimum as a function of Mach number. The Mach number at which the minimum occurs increases with decreasing pressure. This behavior is attributed to the arrival of the interaction wave within the period of measurement. From these measurements, it would appear that the recombination processes are so enhanced by the increased pressure resulting from the incidence and reflection of the interaction wave that the expected increase in electron concentration is quickly negated. One might fully expect, however, that as the Mach number is further increased, this trend would be reversed. Several other phenomena may also be affecting the measurements at these longer times after reflection. Attenuation of the incident shock and irreversible losses such as radiative recombination in the ionized region  $2E$  should certainly affect the thermodynamic properties since these effects can propagate along characteristics toward the wall from the reflected shock. Another serious effect which can not be simply evaluated is the bifurcation of the reflected shock, as discussed earlier in this chapter. This phenomenon would be manifested by a rather thick separated region similar to that sketched in figure 16. To comment on the direction of the related error incurred by the optical measurements would require a knowledge of the state of the gas in the separated region relative to the "free stream". In connection with this separated region behind the reflected shock, it may be noted that there is a likelihood of gradients in refractivity normal to the light rays. These gradients would certainly cause indeterminate errors and might even be responsible for the

fringe "waviness" in the stronger shock cases.

In a similar connection, the presence of side wall boundary layers can cause serious systematic errors which are again difficult to evaluate. An estimate of the possible error resulting from the side wall boundary layer is made in Appendix A where it is shown that the measured density may be 20% too high and the electron concentrations only a few percent too low. No corrections were made to the measurements, however, since the extent of some of the effects could not be determined and might well tend to cancel the above boundary layer error.

The thermodynamic properties obtained from the measured fringe shifts at 100  $\mu$ sec after reflection are given in figures 31, 32, 33, and 34. The properties at the edge of the boundary layer were obtained from these figures for the corresponding Mach number and pressure at which the boundary-layer snapshots were taken.

Figure 35 shows a time history of the measured thermodynamic properties for the particular case of  $M = 11$  into 5 torr. This figure gives some estimate of how the radiative cooling affects the reflected shock gas properties and indicates that the cooling plays a dominate role in the long time history of the reflected shock properties. Although it has not been done here, the present data may be considered in terms of theoretical models for the radiative emission from shock heated argon.

Now that the shock structure has been studied and the thermodynamic properties measured to reasonable accuracy, we are in a position to evaluate the boundary layer interferograms obtained for an ionized gas.

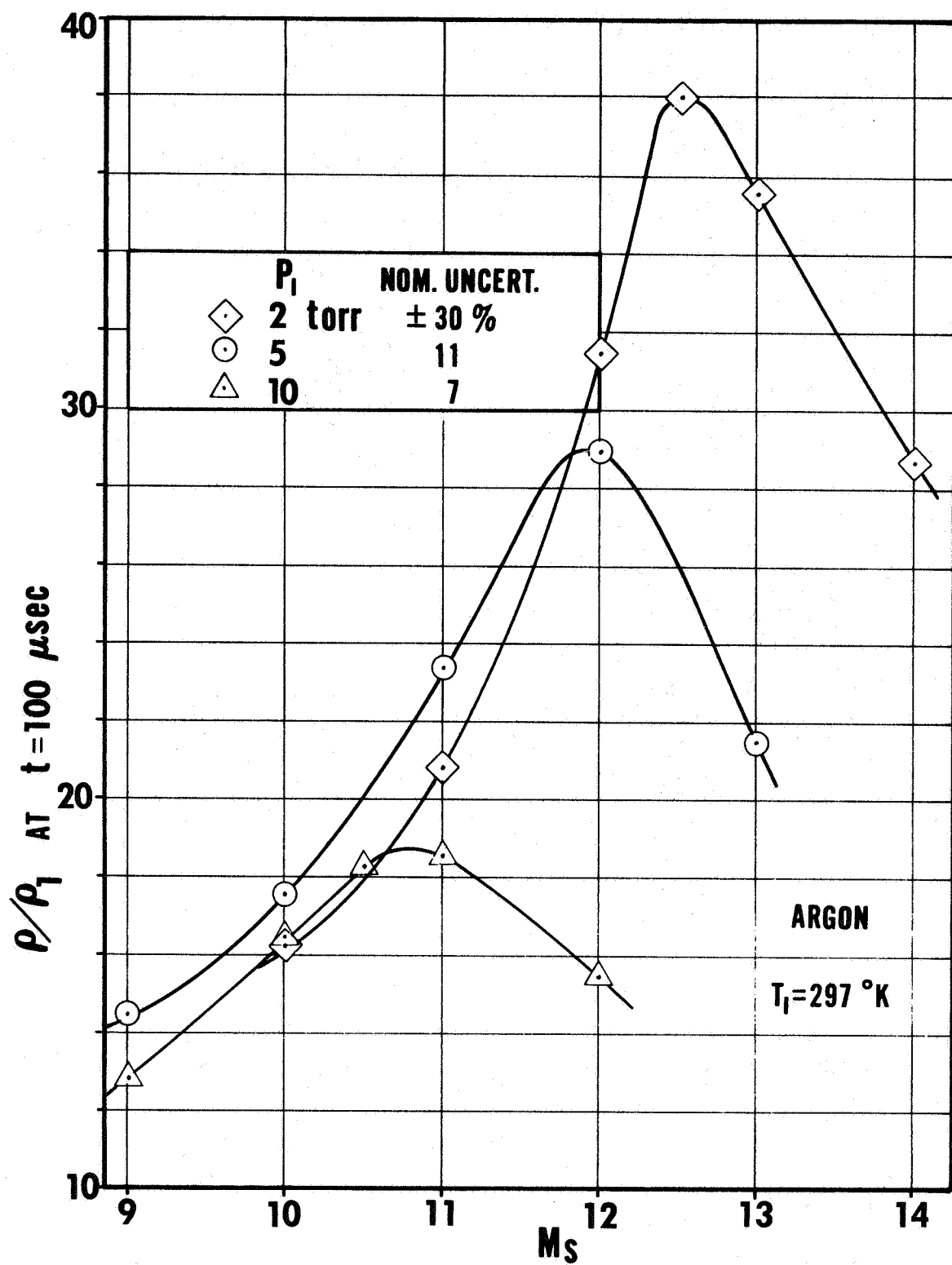


Figure 31. Reflected shock densities at 100 microseconds after reflection.

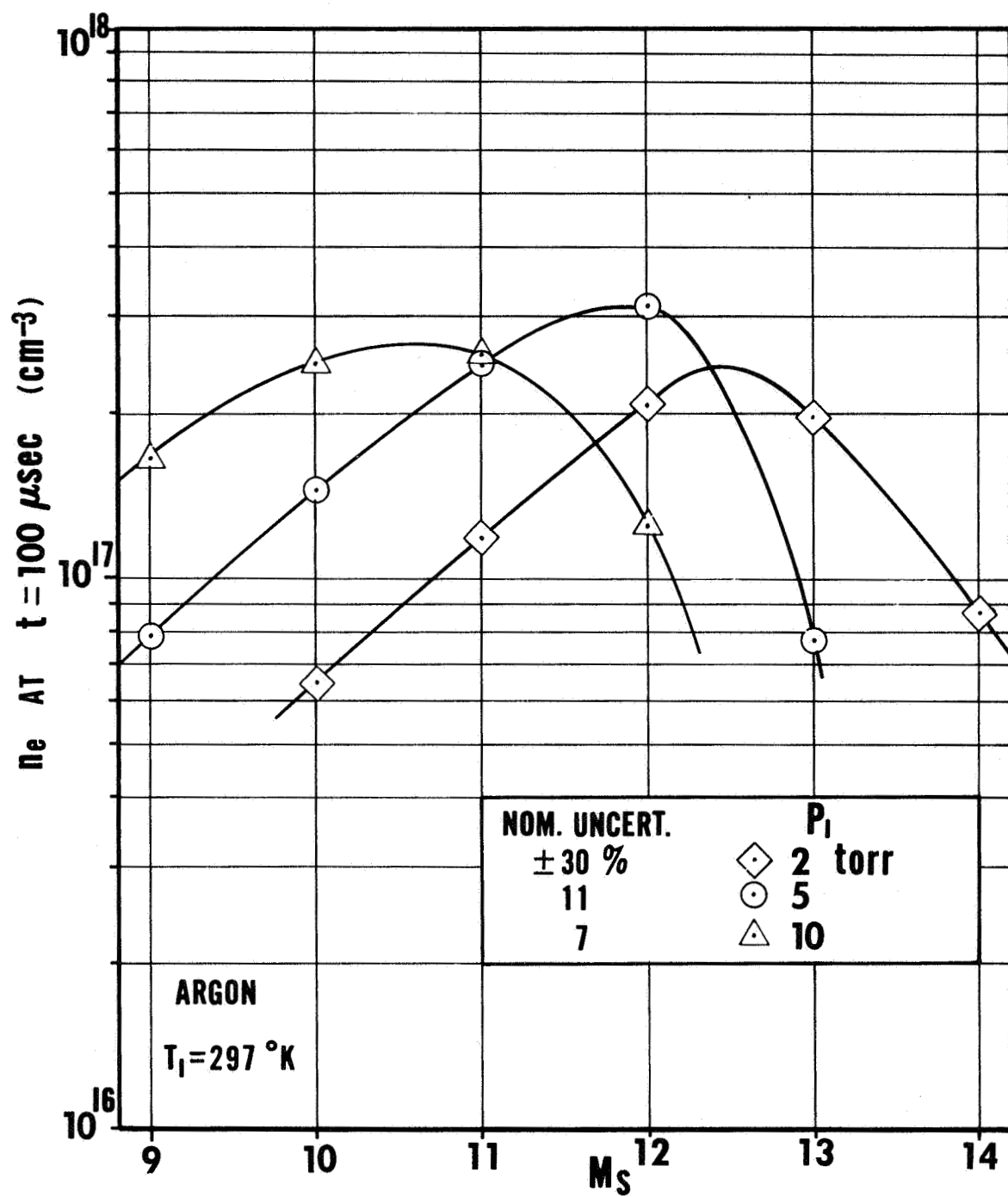


Figure 32. Reflected shock electron concentrations at 100 microseconds after reflection.

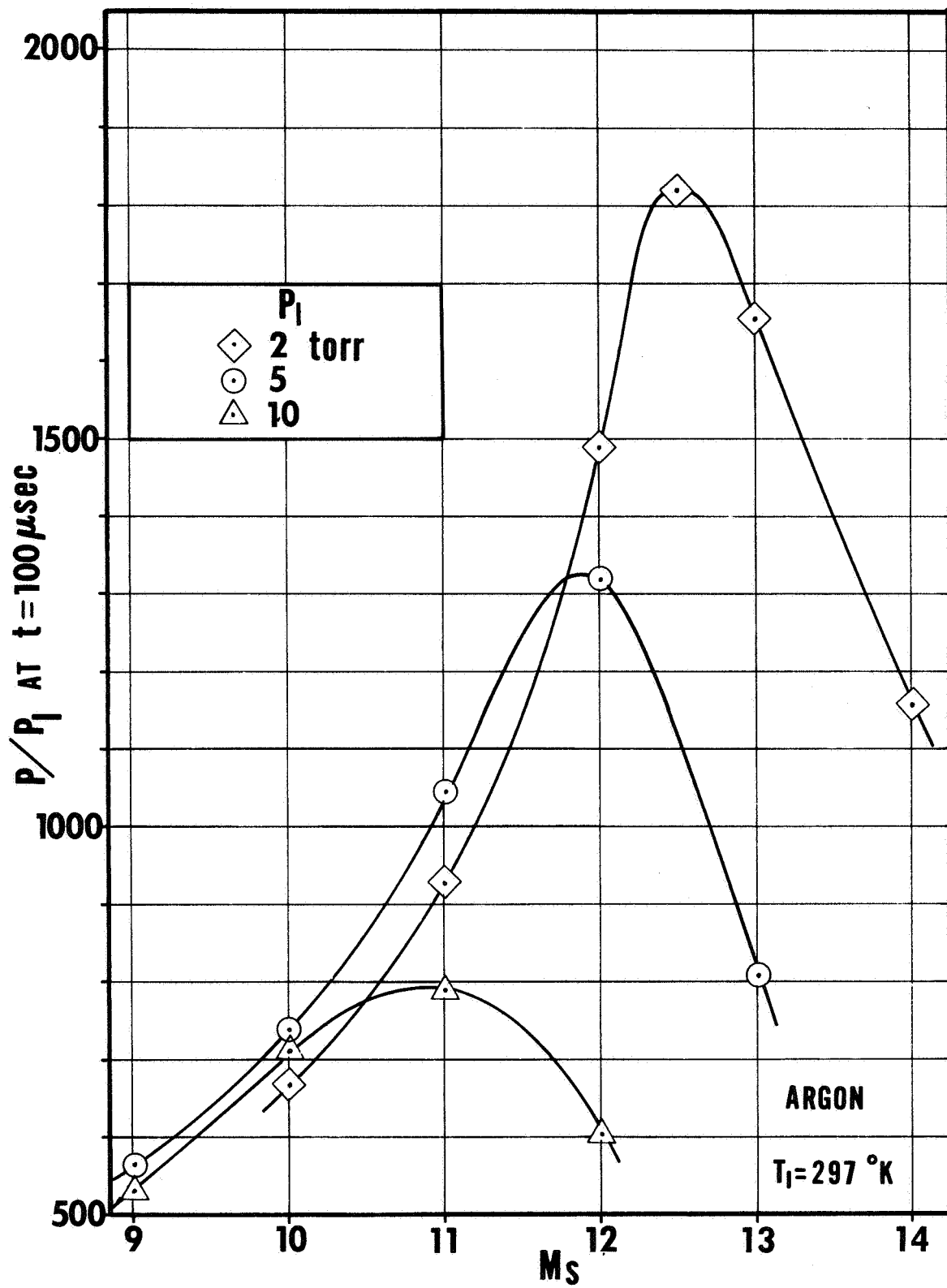


Figure 33. Reflected shock pressures at 100 microseconds after reflection.

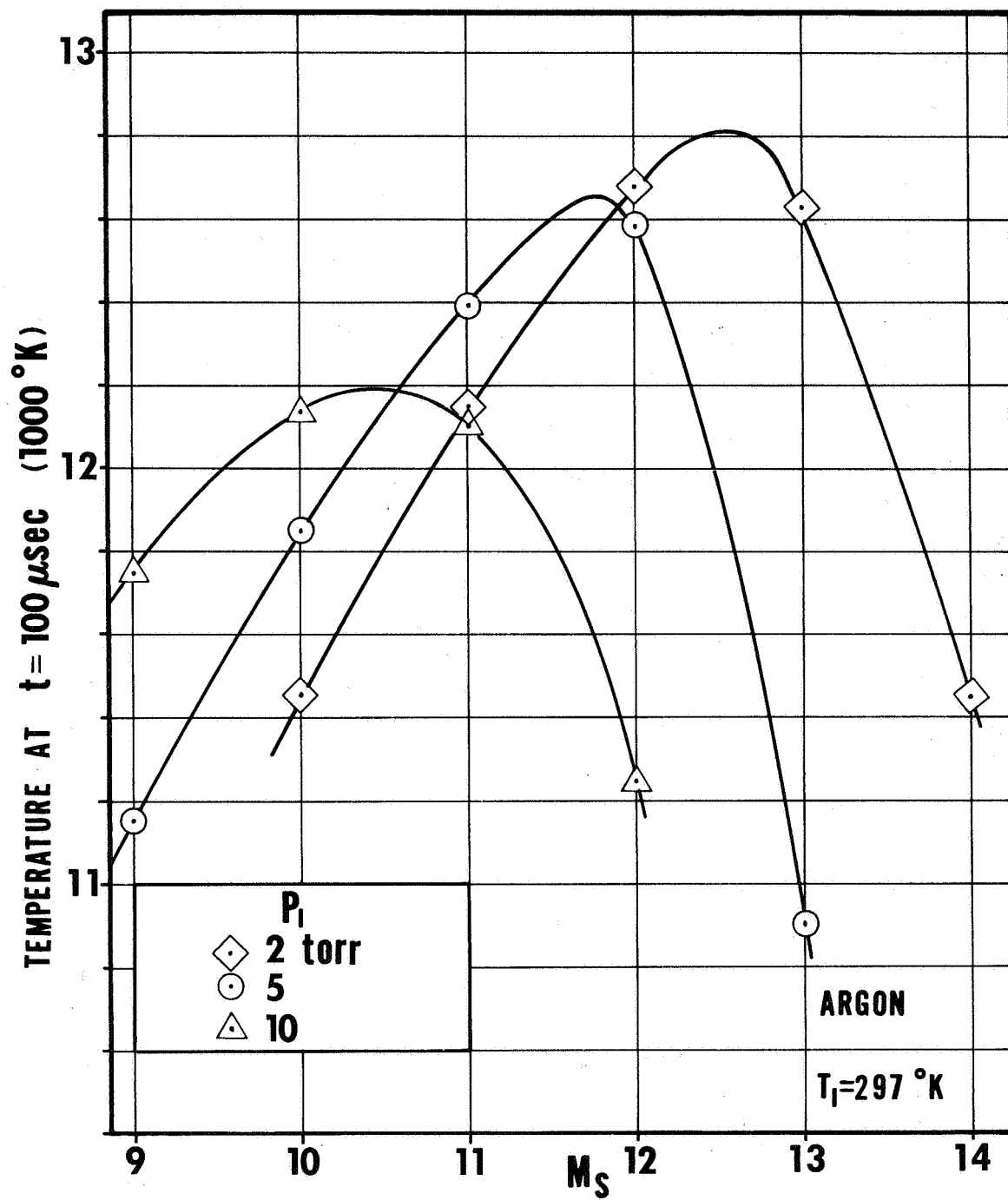


Figure 34. Reflected shock temperatures at 100 microseconds after reflection.

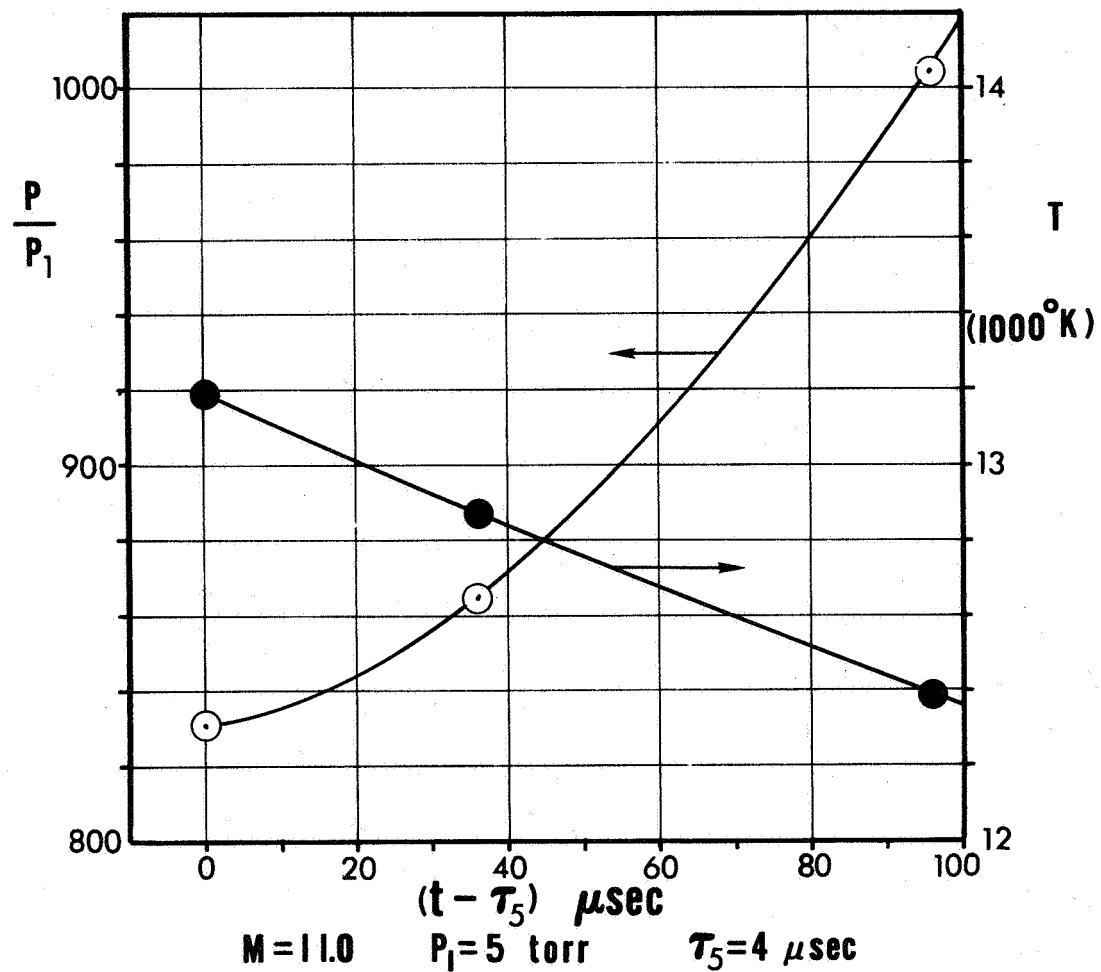
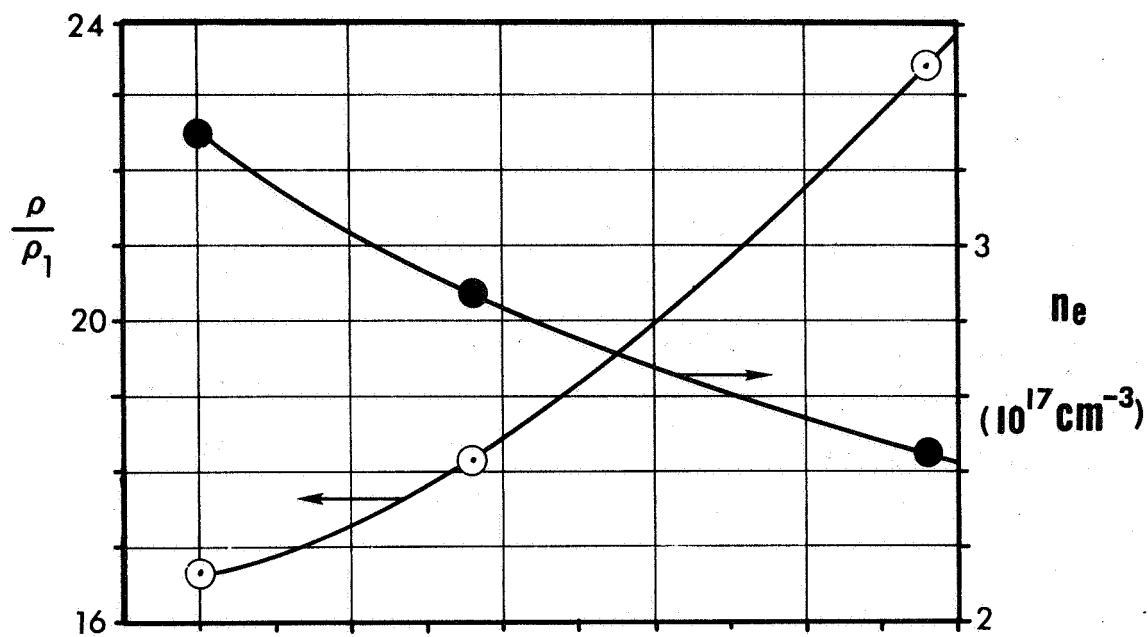


Figure 35. Time history of argon thermodynamic properties in reflected shock region.

## IONIZED BOUNDARY LAYER RESULTS

5.1 Theoretical. Experimental results have been obtained for the end-wall thermal layer for the case of an ionized "free stream" using techniques similar to those already described for unionized argon. Previous experimental investigations in the ionized regime were concerned with heat transfer rate measurements at the wall. The results presented in this chapter therefore represent the first successful attempts at experimentally resolving the variation of electron concentration and mass density through an ionized boundary layer. The experimental boundary layer profiles will be compared with calculations based on the theory of S. Knöös<sup>(12)</sup>. The primary discrepancy between theory and experiment occurs in the electron concentration, and, as will be shown, is probably a result of the failure of the present theories to adequately describe the physical problem.

The theory of end-wall heat transfer in a monatomic gas including ionization effects was first considered by Fay and Kemp<sup>(22)</sup>. Their analysis was concerned primarily with determining the surface heat flux, and they considered three limiting cases for which similarity solutions were feasible, namely: (1) no ionization; (2) complete thermodynamic equilibrium behind the reflected shock and in the boundary layer; (3) thermodynamic equilibrium behind the reflected shock, but no gas-phase recombination in the boundary layer, i. e., frozen boundary layer. Their analysis took no account of radiation effects on either the freestream or boundary layer properties and neglected any plasma "sheath" effects. It might also be added that models (2) and (3) above do not necessarily provide the bounds for a general thermodynamic and chemical nonequilibrium calculation.

As previously noted, reference 22 reports on the analytic results for the surface heat flux but gives no boundary layer "profiles." The heating rates



to the end-wall were of primary interest to them because they were to provide the basis for comparison with the heat transfer experiments of Camac and Feinberg<sup>(1)</sup>. The latter used an infrared detector gauge to measure the heat transfer rates to a shock tube end-wall in the presence of ionized argon. The agreement between their experimental results and those of this study for the un-ionized case has already been discussed in Chapter III; however, it is of interest to this discussion to note that Camac and Feinberg saw no change in surface heat flux when equilibrium was attained behind the reflected shock. This meant that, the experimental results for the heat flux in the ionized regime were higher than the theoretical predictions. It would appear from their discussion that one should use caution in drawing major conclusions from this result. However, one contributing factor is already clear from the results of Chapter IV, namely, that the freestream properties (conditions at 5E) used in their calculations correspond closely to the curves marked theory in figures 27, 28, 29, and 30. From these figures, one can readily see that the actual conditions are generally more severe, and so one might reasonably expect a greater heat flux for the actual conditions. In view of the present results, however, it is more than likely that this unusual result is also partially due to the oversimplification of the problem. The fact that they noticed no change in the heat transfer signal until the arrival at the wall of the interaction wave implies that the onset of equilibrium represents no large perturbation on the boundary layer development. One is then at least partially justified in assuming that the ionized boundary-layer profiles measured in the present experiments at  $t = 100 \mu\text{sec}$  after reflection are unaffected by the un-ionized boundary layer prevailing for  $0 < t < \tau_5$ , where  $\tau_5 \ll 100 \mu\text{sec}$ .

Camac and Feinberg did find a significant increase in surface heat flux upon arrival of the interaction wave at the surface. This indicates a significant change in free stream conditions and boundary layer profile. Because of experimental limitations, it was not possible in this investigation to determine the exact effect of this pressure wave on the thermal layer growth. To avoid

this unknown, the present measurements were made at conditions such that  $\tau_{2L} \approx 100 \mu\text{sec}$  so that the effect was negligible. This also avoided what appeared to be nonuniformities in the reflected shock region for stronger incident shock conditions. (See the interferograms of figure 17 for example.)

In reference 31, Camac and Kemp have attempted a multitemperature solution of the thermodynamic profiles for the end-wall boundary layer including chemical nonequilibrium. Because inclusion of these considerations renders a similarity solution impossible, they were only able to report the results for one case of frozen chemistry but including the poor energy transfer between the lighter electrons and heavy particles through elastic collisions, i. e., a two temperature boundary layer. The paucity of results in their report makes it impossible to draw any conclusions by comparison with the experimental results of this investigation.

Knöös<sup>(12)</sup> considered the shock tube, side-wall boundary layer and the Rayleigh problem for the case of ionized argon. His treatment of the end-wall boundary layer is a special case of the Rayleigh problem with the wall velocity equal to zero and is essentially similar to the equilibrium analysis of Fay and Kemp<sup>(22)</sup>, although the latter were concerned only with the heat flux. The theoretical boundary layer profiles of Knöös are used for comparison with the profiles obtained in the present experiments. Only a brief outline of the theory including essential results will be given here.

The conservation equations used for the equilibrium, ionized boundary layer are structurally similar to those used for the un-ionized boundary layer of Chapter III, except that the energy equation includes the effects of species diffusion. If we let  $C_i$ ,  $h_i$ , and  $\vec{V}_i$  be the mass concentration, enthalpy, and diffusion velocity of species  $i$  respectively, then the conservation equations become

$$\frac{\partial \rho}{\partial t} + \frac{\partial (\rho v)}{\partial y} = 0 \quad (5.1)$$

$$\frac{\partial h}{\partial t} + v \frac{\partial h}{\partial y} = \frac{1}{\rho} \frac{\partial}{\partial y} \left[ K \frac{\partial T}{\partial y} + \sum_i \rho C_i h_i \vec{V}_i \right] \quad (5.2)$$

If the bracketed term on the right in the energy equation can be written in terms of a total conductivity so that

$$q = -K_{tot} \frac{\partial T}{\partial y} \quad (5.3)$$

then the equations are amenable to a similarity analysis in terms of a new variable defined by

$$\eta = \frac{1}{2} \left( \frac{\rho_{\infty} C_{p\infty}}{K_{tot\infty} t} \right)^{1/2} \int \frac{\rho}{\rho_{\infty}} dy \quad (5.4)$$

The single ordinary differential equation

$$2\eta \frac{dH}{d\eta} + \frac{d}{d\eta} \left( \frac{\rho K_{tot} C_{p\infty}}{\rho_{\infty} K_{tot\infty} C_p} \frac{dH}{d\eta} \right) = 0 \quad (5.5)$$

is then obtained where

$$H = \frac{h - h_w}{h_\infty - h_w} \quad (5.6)$$

and for which the boundary conditions are taken as (for  $t > 0$ )

$$\begin{aligned} H(0,t) &= 0 \\ H(\infty,t) &= 1 \end{aligned} \quad (5.7)$$

The analysis proceeds by matching inner and outer solutions and interpolating for the transport properties in the boundary layer. The expression used for the total thermal conductivity is

$$K_{\text{tot}} = K + \frac{\alpha(1-\alpha)}{2} D_{\text{amb}} \frac{P}{T} \left[ \frac{5}{2} + \frac{I}{KT} \right] \quad (5.8)$$

where  $D_{\text{amb}}$ ,  $I$ , and  $K$  are respectively, the ambipolar diffusion coefficient, the ionization potential (15.75 ev), and the translation thermal conductivity of the mixture of electrons, ions, and neutrals; the latter quantity is obtained from the individual components through a mixture rule. The rest of the details of the analysis and calculations are not included here. However, it is worth noting again the most important assumptions made in this theoretical approach:

1. Thermodynamic and chemical equilibrium, i. e., the electrons and heavy particles are at the same temperature and the composition and temperature are related by the Saha equation.
2. Radiation effects in both the freestream and boundary layer are neglected, i. e., no variation of free-stream properties due to radiation cooling and no absorption or emission by the boundary-layer fluid.

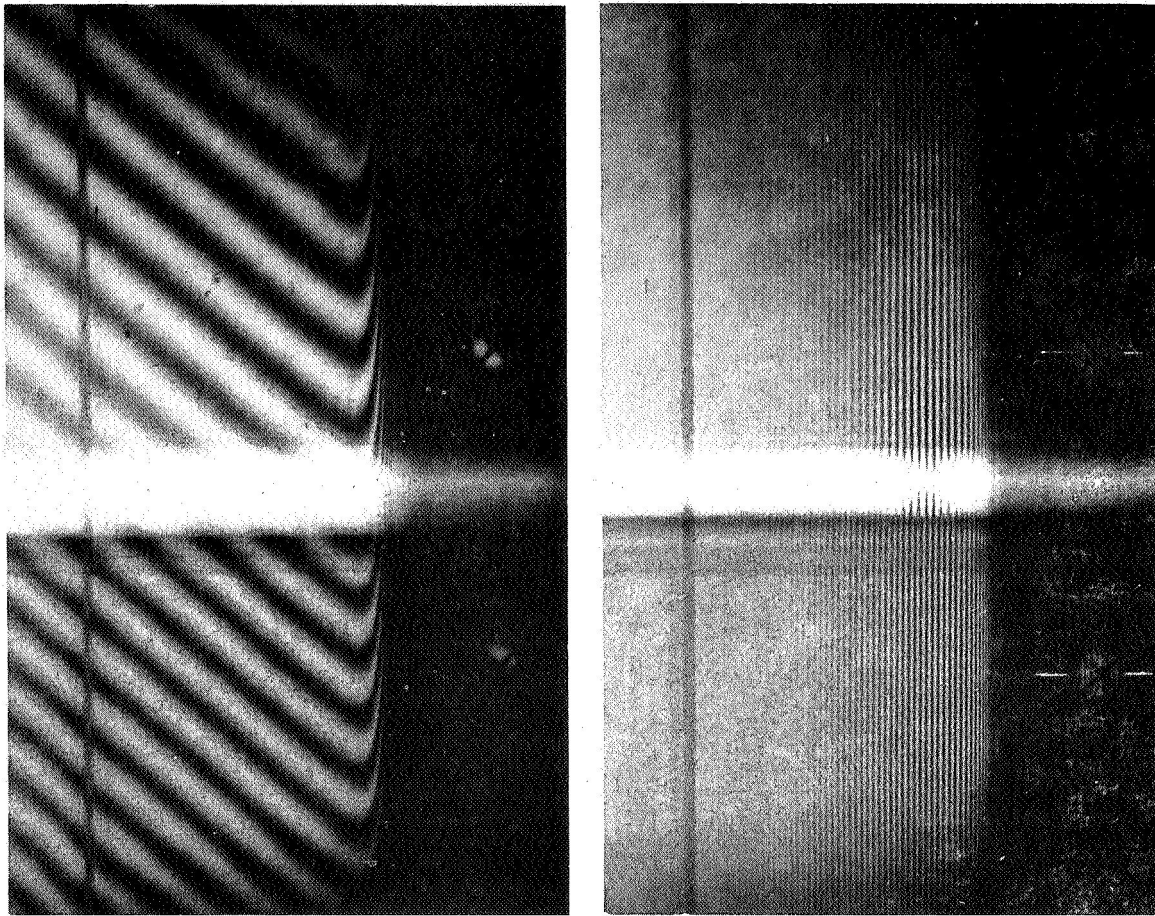
3. The wall is at a floating potential, i. e. , no net current to the wall.
4. The general assumption that the calculated transport properties for a partially ionized gas used in the analysis are correct.

The assumption of charge neutrality and ambipolar diffusion in the boundary layer is also made. This assumption appears to be well justified by the small Debye length in the boundary layer, i. e. ,  $10^{-5}$  mm. Deviations from the four assumptions already listed above, however, are believed to be primarily responsible for the discrepancies between theory and experiment discussed in the following section.

5.2 Experimental Results. The experimental results for the end-wall, boundary-layer profiles for the case of ionized argon are obtained in a manner similar to that for the un-ionized case as described in Chapter III. The primary differences are the manner of data reduction and in the fact that the free-stream, reference quantities (  $\rho_{\infty}$  and  $n_{e\infty}$  ) are obtained from the measurements presented in Chapter IV.

Figure 36 shows two snapshot interferograms of the ionized boundary layer in argon formed on the end wall of the shock tube. These snap shots were taken 100  $\mu$  sec after shock reflection, as were all of the results shown in this chapter. The interferogram on the left could, of course, be used for quantitative measurements; however, the spatial resolution is not as fine as that obtainable from the usual type shown on the right and is presented only to illustrate the extent of the boundary layer. It may be noted that the boundary layer thickness is on the order of 1 mm and that the fringes shift upward as one moves toward the wall, indicating the increase in refractivity. The time of  $t = 100 \mu$  sec was selected to provide a spatially resolvable boundary layer and to be within the test time in the reflected region. The experiments, furthermore, had to be done at strong enough conditions that there were enough electrons present to be of interest and yet be weak enough to have a relatively long, incident-shock

$$\lambda = 5720 \text{ \AA}$$



$$\lambda = 4530 \text{ \AA}$$

$$M_S = 11.1$$

$$M_S = 11.0$$

1cm

**INTERFEROGRAMS OF IONIZED END-WALL  
BOUNDARY LAYER IN ARGON  $P_1 = 5$  TORR**

**FREE-STREAM PROPERTIES**

$$T = 12400^\circ \text{K} , \quad n_e = 2.5 \times 10^{17} \text{ CM}^{-3}$$

$$P = 7.2 \text{ ATM} , \quad \alpha = .067$$

$$t = 100 \text{ } \mu\text{SEC}$$

Figure 36. Snapshot interferograms of ionized end-wall boundary layer in argon.

relaxation time. This latter criterion has already been mentioned as being necessary to avoid the complications arising from the presence of the interaction wave. From the interferograms, it was noted that if  $\tau_{2L} > 40 \mu\text{sec}$ , the interaction wave was very weak so even if  $\tau_{2L}$  was somewhat less than  $100 \mu\text{sec}$ , it could still be considered to have a negligible effect on the boundary layer. Due to the difference in relative time scales, it was possible to do experiments with  $\tau_{2L} \sim 100 \mu\text{sec}$  and still have  $\tau_5 \ll 100 \mu\text{sec}$ .

The fringe shift distribution for each wave length is obtained from an interferogram like that on the right in figure 36 in exactly the same manner as described previously for the un-ionized boundary layer. Because the fringes for each wavelength are not at the same distance from the wall, smooth curves had to be drawn through the reduced fringe shift data in order to obtain simultaneous fringe shifts at the same space coordinate. This procedure is illustrated by one example in figure 37. It should not be disturbing that the two fringe shift curves lie so closely together as this simply results from the increased sensitivity at the longer wave length because of the presence of electrons. For the same mass density profile with no electrons present the fringe shifts for the long wave length would be lesser than for the short wave length by the ratio of the two wave lengths. A consideration of the following data reduction equations, derived from equation 2.4, will further convince the reader that there is nothing disturbing about figure 37.

$$\frac{\rho}{\rho_\infty} = 1 + \frac{\lambda_1 A_2 B_2 S_1 - \lambda_2 A_1 B_1 S_2}{L(B_2 - B_1) A_1 A_2 \rho_\infty} = 1 + \frac{1.523 S_1 - 1.222 S_2}{\rho_\infty (10^4)}$$

$$\frac{n_e}{n_{e\infty}} = 1 - \frac{\lambda_2 A_1 S_2 - \lambda_1 A_2 S_1}{L(B_2 - B_1) A_1 A_2 n_{e\infty}} = 1 - \frac{2.056 S_2 - 1.611 S_1}{n_{e\infty} (10^{-17})}$$

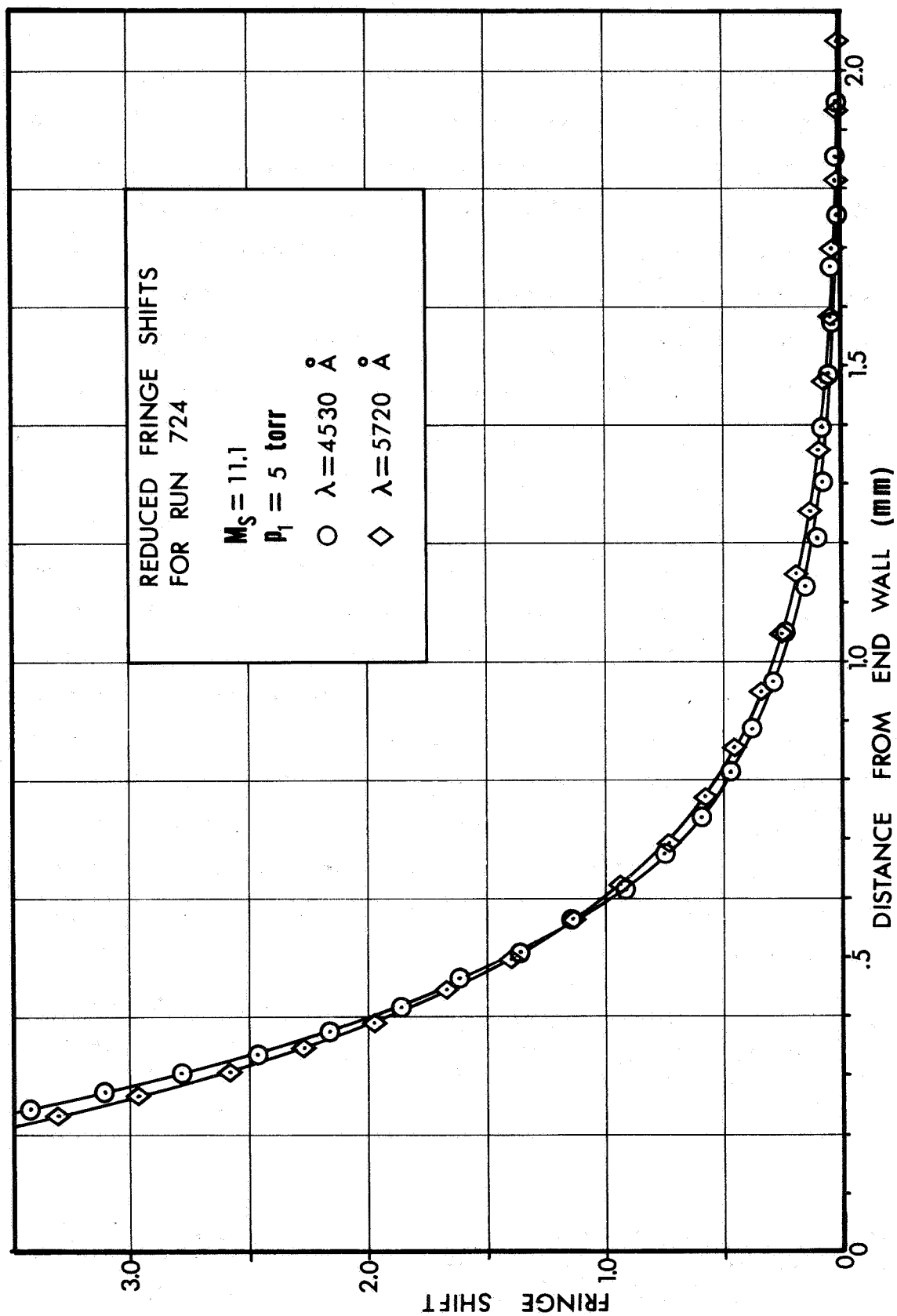


Figure 37. Measured fringe shifts at two wavelengths in ionized argon boundary layer.



In these equations the subscripts 1 and 2 refer to quantities evaluated or measured at  $\lambda_1 = 4530 \text{ \AA}$  and  $\lambda_2 = 5720 \text{ \AA}$  respectively, and the quantities  $\rho_\infty$  ( $\text{gm/cm}^3$ ) and  $n_{e\infty}$  ( $\text{cm}^{-3}$ ) are obtained from figures 31 and 32 of Chapter IV.

Unlike the un-ionized studies of Chapter III, a radiation stop had to be used for the ionized boundary-layer experiments to prevent the test gas radiation from "washing out" the interferograms. Unfortunately, the edges of the radiation stop, placed near the focal point of the field lens acted like a Schlieren knife edge blocking out light rays which had been deflected by the refractivity gradient in the boundary layer. This had not been anticipated, and so the first attempts were unsuccessful because the boundary layer appeared as a shadow which was first thought to be due to the crowding of the fringes in the boundary layer. However, analysis indicated and trial and error verified that for the dimensions and test conditions used, the light passing through the boundary layer as far as .8 mm from the wall was deflected at the focal point of the field lens by as much as 3-5 mm. The problem was alleviated by opening one side of the radiation stop and blocking off that half of the test section field of view that was of no interest (away from the wall) with a piece of black paper. An indication of the radiation intensity from the test section was exhibited by the charring of the paper mounted just outside the test section window and the resulting deposition of char vapors on the window itself.

The results from three ionized boundary layer experiments are presented in figures 38, 39 and 40 along with theoretical curves obtained from the analysis of reference 12 outlined above. Note that the two measured quantities are the density and electron concentration normalized by the free stream values. The degree of ionization plotted in the figures is obtained from  $\alpha = n_e m_A / \rho$ . The experimental uncertainty in the results was calculated at .3 mm from the wall and is indicated by the horizontal and vertical bars in the figures. These uncertainties are based on an overall fringe shift error at each wavelength of  $\pm .1$ , uncertainties in the free stream properties corresponding to those shown on figures 31 and 32, and wall location of  $\pm .015$  mm. If one considers the

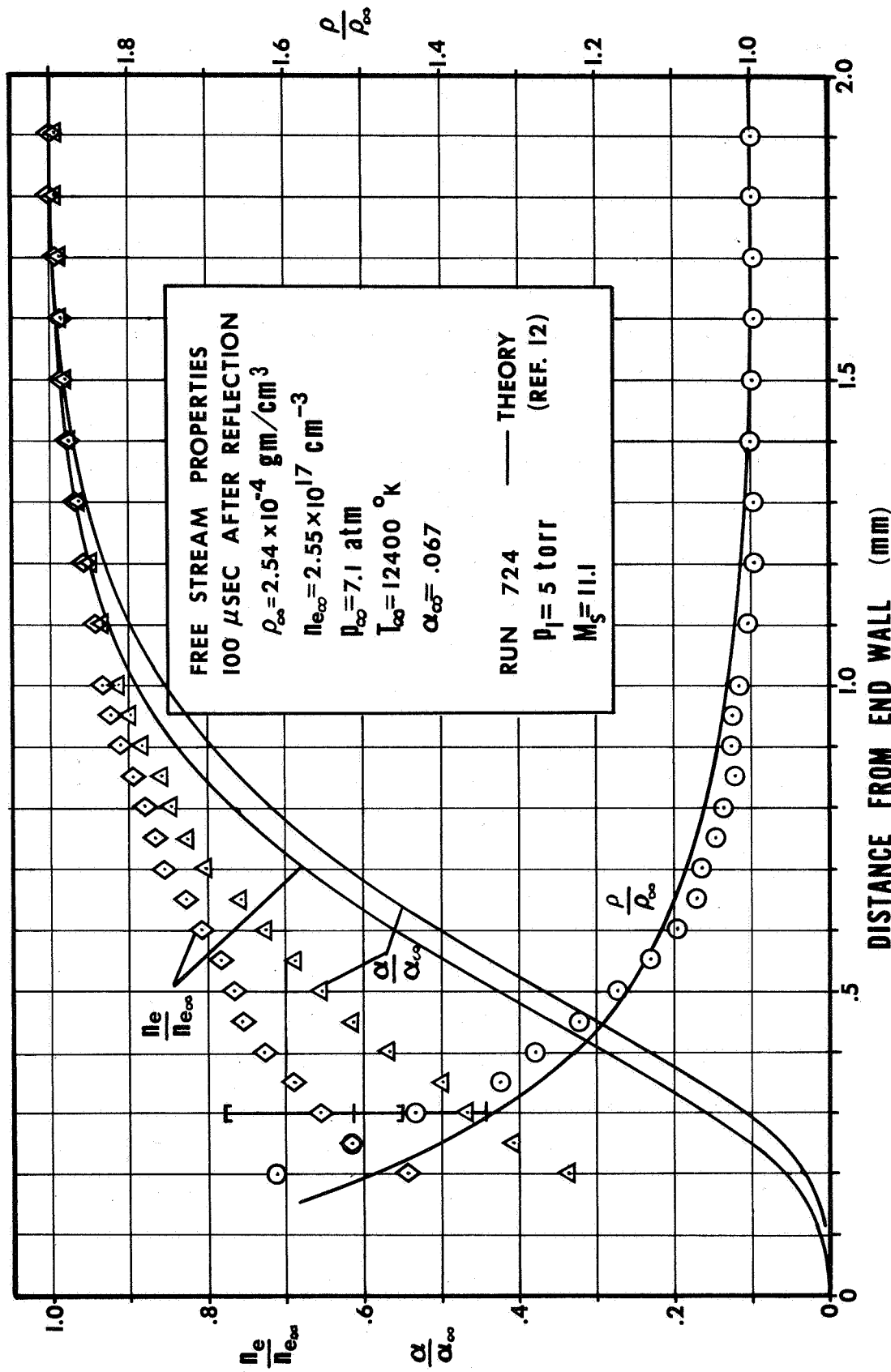


Figure 38. End-wall boundary layer profile of density and electron concentration in ionized argon.

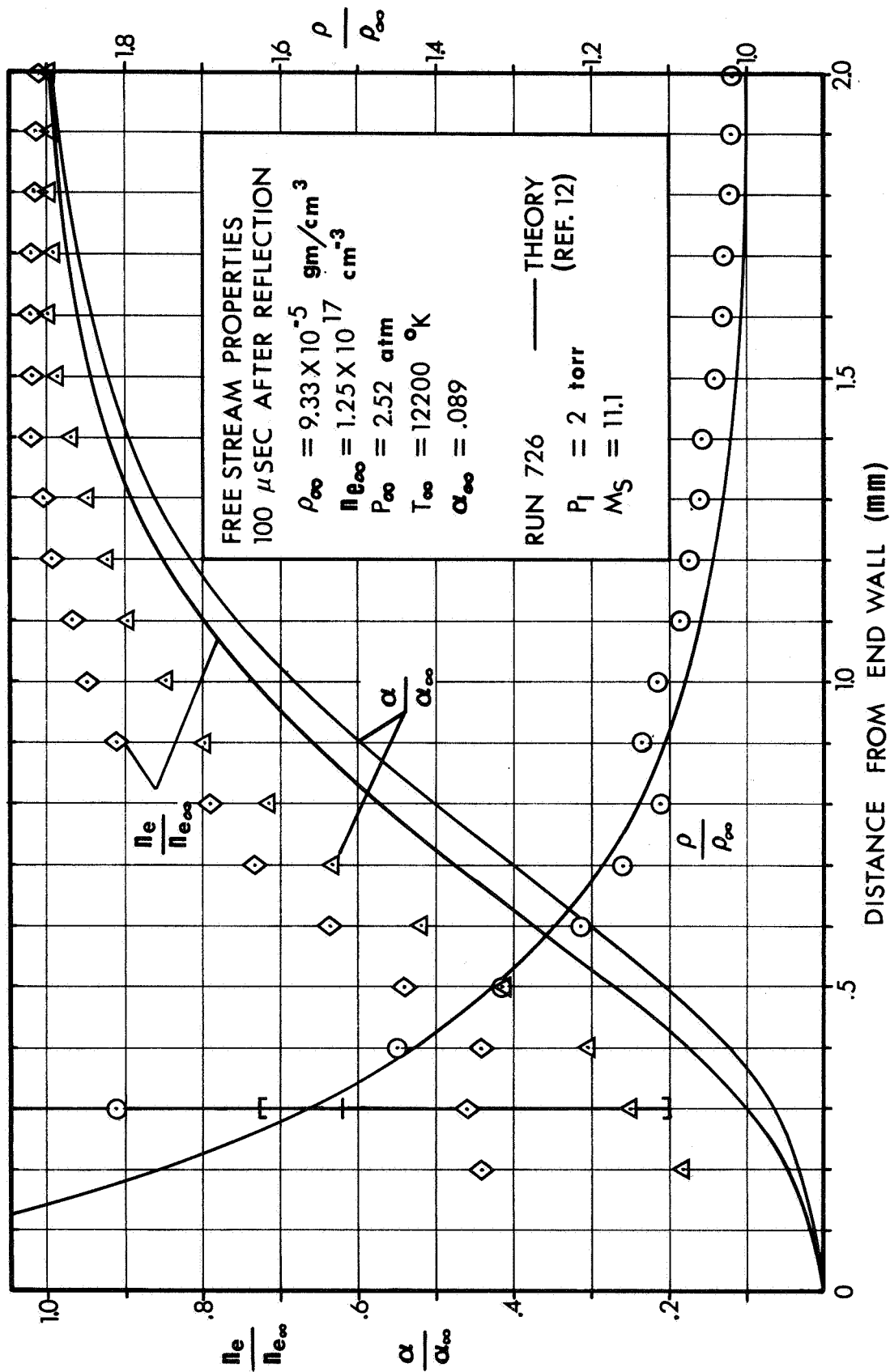


Figure 39. End-wall boundary layer profile of density and electron concentration in ionized argon.

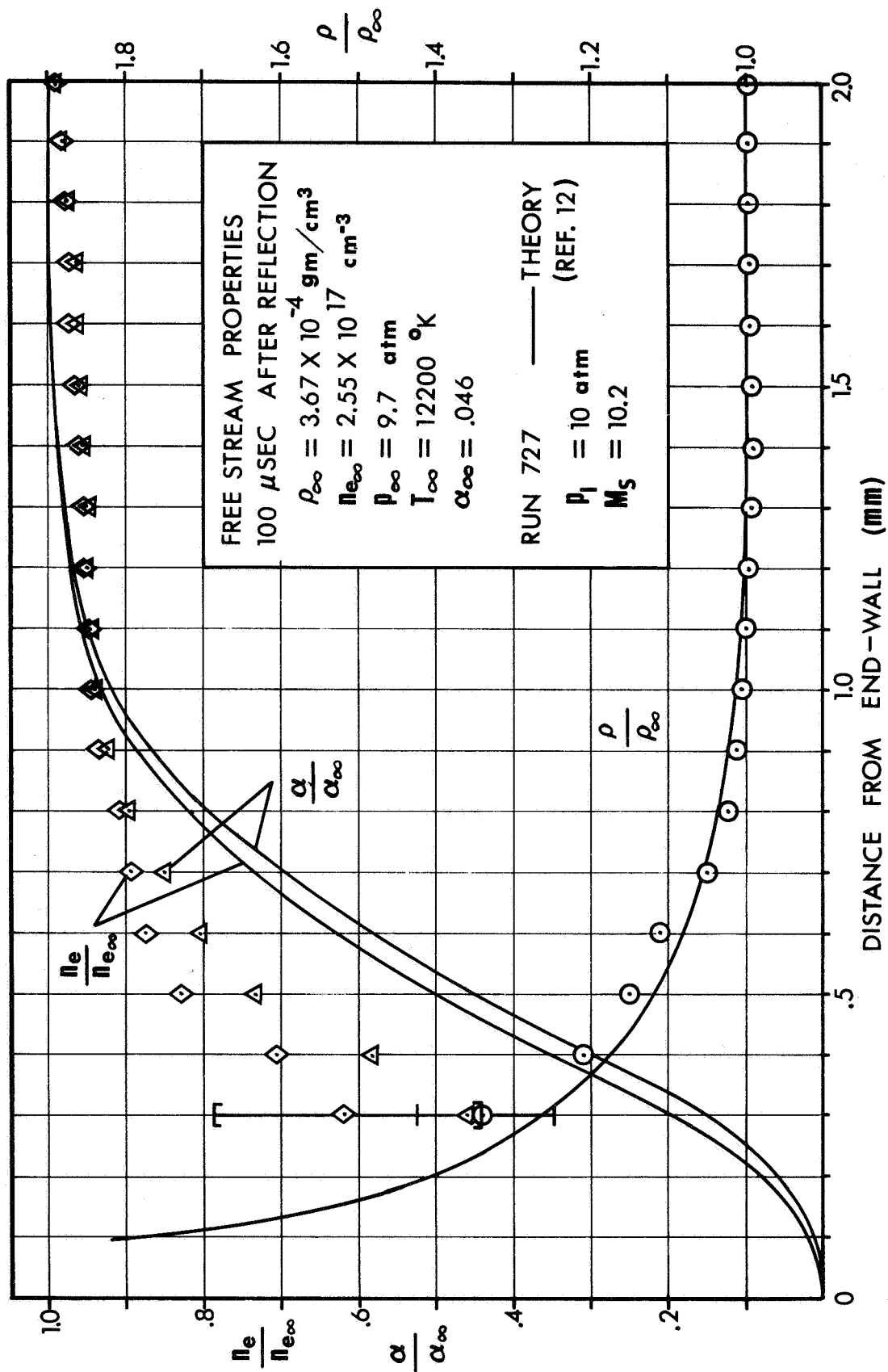


Figure 40. End-wall boundary layer profile of density and electron concentration in ionized argon.

uncertainty in the time after reflection as  $\pm 4 \mu\text{sec}$ , an additional error of only a few percent would appear in the distance coordinate with negligible error in the dependent variables. It is readily apparent that the experimental uncertainty does not make up the discrepancy between theory and experiment, and one must therefore look to the theoretical treatment for the source of the disagreement.

5.3 Discussion of Results. The experimental results shown on the figures in section 5.2 correspond to the free stream properties measured at  $100 \mu\text{sec}$  after reflection. The theoretical curves are based on the assumption that these properties prevailed from time zero. A rough estimate of the effect of varying free stream conditions in the theory might be obtained by performing the calculations with the conditions at the onset of ionization behind the reflected shock. This means using the properties at 5E instead of those at  $100 \mu\text{sec}$  as inputs to the analysis. The results of doing this yielded very little difference between the two sets of theoretical curves. Although it is true that this approach is artificial, it is taken to imply that varying free stream conditions is not a main source of the discrepancy.

The assumption of local thermodynamic equilibrium and a one temperature boundary layer may be subject to question. In particular, one can calculate a temperature profile if the Saha equation is used in conjunction with the measured values of  $\alpha$  and  $\rho$  through the boundary layer. And if this derived temperature along with the measured values for  $\alpha$  and  $\rho$  are used to compute a pressure with  $p = (1 + \alpha)\rho RT$  one finds that the pressure does not remain constant as one approaches the wall, as is generally assumed in boundary layer analyses. In fact, the pressure increases monotonically to factors as high as 2.0 and 1.2 times the free stream pressure for initial test pressures of 2 and 10 torr respectively. To arrive at the assumption that the pressure is constant through the boundary layer, one usually makes an order of magnitude comparison of the various terms in the momentum equation normal to the surface. In view of the fact that the gas is highly ionized, it may no longer be true that the body

forces acting on the fluid are negligible, and therefore, even though the induced velocity in the boundary layer is small, adequate body forces (arising from induced electric fields) may be acting to support the negative pressure gradient  $dp/dy$ . This is conjecture, however, since the full equations including the normal momentum equation would have to be solved to obtain verification.

It seems much more likely at this time that the reason for the unexpected behavior of the derived pressure is that the assumption of equilibrium is invalid over a large portion of the boundary layer. A proper criterion to determine whether chemical equilibrium prevails in a particular flow situation will allow a determination of whether or not the rate of production or depletion of the various species through collisions can keep up with the rates due to gradients in the flow process. Such a criterion was used by Knöös<sup>(12)</sup> in the ambipolar region of the boundary layer by considering the electron continuity equation to compute  $(\partial n_e / \partial t) / n_e$  and then comparing the result with the "available number of collisions",  $Q^{avail}$ , resulting for the three body recombination reaction



Equilibrium is then assumed if the following criterion is satisfied

$$\frac{Q^{avail}}{\frac{1}{n_e} \left( \frac{\partial n_e}{\partial t} \right)} = \frac{t Q^{avail}}{Q^{conv} + Q^{diff}} \gg 1$$

where  $Q^{conv}$  and  $Q^{diff}$  are respectively measures of the local loss of electrons due to convection and diffusion,  $t$  is the time after shock reflection, and

$$Q^{avail} = k_{rec} n_e^2$$

$$k_{rec} = 1.3 (10^{-32}) \left( 2 + \frac{134000}{T} \right) \exp \left( \frac{49000}{T} \right) \left[ \frac{\text{cm}^6}{\text{elec}^2 \cdot \text{sec}} \right]$$

The denominator of the above expression has been computed along with the other properties in the boundary layer profiles and a check on the above criteria made. The results indicate that for the entire 100  $\mu$  sec, even at relatively large distances from the wall (e. g. , 80% of the boundary layer thickness), the above criterion is not satisfied. Note that for longer times, the equilibrium criterion is more easily satisfied, but its use is questionable since the denominator is calculated based on the assumption of equilibrium during all stages of development.

With respect to the question of temperature equilibrium between the electrons and heavy particles, it is generally argued that because of the disparity in mass between electrons and heavy particles,  $m_A / m_e \sim 10^5$  collisions are required for equilibration to a single temperature for the two components. For a stationary gas, one criteria for temperature equilibrium between electrons and heavy particles is that the atom temperature shall change very little over a distance  $L$  where  $L$  is now given by

$$\left(\frac{L}{\lambda}\right)^2 \sim 10^5$$

or

$$\frac{\delta T_A / T_A}{L} \sim \text{grad}(\ln T_A) \ll \frac{1}{10^{5/2} \lambda}$$

For the present purposes, a conservative estimate for the mean free path,  $\lambda$ , would yield  $1 \text{ mm}^{-1}$  for the right-hand side of the inequality. This says that to maintain temperature equilibrium, the atom temperature should not change much over distances of the order of 1 mm. Since the boundary layer thicknesses are on the order of 1 mm, one might reasonably expect that the above criterion would not be satisfied close to the wall where the gradients are steep. For example, in the only solution presented in the two temperature analysis of reference 31, the electron temperature at the sheath edge was still 50% of the free stream value:

The nature and extent of a plasma sheath at the wall in the present problem is also not well understood. One usually assumes that there is a thin region adjacent to the wall with a thickness on the order of the Debye length  $h = (\epsilon_0 k T_e / e^2 n_e)^{1/2}$  in which space charge effects dominate. Using the measured values closest to the wall for  $n_e$  and assuming  $T_e \sim .5 T_\infty$  results in  $h \sim 10^{-5}$  mm. In this region, Poisson's equation is applied with the assumption of no net current to the wall. It is furthermore generally assumed that the surface otherwise represents no large perturbation on the fluid, e. g., no heat transfer, and that the problem is "steady," i. e., no time derivatives. It is immediately apparent that these last two assumptions are not valid in the present case, and that therefore, one cannot reasonably expect that the net current to the wall will be zero. The resulting effect on the boundary layer profile is not clear except that now one may not realize the assumption of charge neutrality at the edge of the sheath. These last remarks are made only to indicate further the great complexities which prevail in the ionized boundary layer adjacent to the grounded end-wall of the shock tube. They are also made to indicate where the causes might lie for the unusual behavior of the electron number density profiles near the wall for the case of  $P_1 = 2$  torr (figure 39).

Initially, it was anticipated that the present measurements would give some indication of the values of the transport coefficients in a partially ionized gas. It is now apparent, however, that the complications already discussed in this section severely cloud the sole issue of thermal transport. Therefore, an analytic variation of the transport properties to obtain agreement with experiment, as was done for the un-ionized case, would be of dubious value. It may have been noted from the figures that reasonable agreement exists for the density profiles -- at least in the outer region of the boundary layer. Since this parameter rather than the electron concentration will reflect the values used for the total thermal conductivity more strongly, one might assume that the theoretical values for the transport properties are at least reasonable even though the state of the gas may be slightly out of equilibrium. To compare the



values for the total thermal conductivity used in the analysis of Knöös with others, it is noted that those of Knöös are a maximum of 30% lower than the values given by Devoto<sup>(32)</sup> in the temperature range of 10000-20000°K. Although he did not compute a total thermal conductivity, Ahtye's<sup>(33)</sup> results for the mixture translational thermal conductivity and ion-atom diffusion coefficients are the same as Devoto's. Since the ambipolar diffusion coefficient is closely approximated by twice the ion-atom diffusion coefficient, these two references (32 and 33) would have been in agreement on the total thermal conductivity, as may readily be seen from equation 5.8. Devoto compares his results with the arc measurements of Knopp and Cambel<sup>(34)</sup> and finds relatively good agreement although the theory is on the order of 10 to 20% lower.

The experimental results of this study have shown that the present theories do not adequately describe the end-wall boundary layer for ionized argon. It appears from a comparison with one of these theories that the causes of the discrepancies can be attributed to the inapplicability of the basic assumptions listed earlier in this chapter. The task of providing an adequate theory to agree with the present experiments has been left for future efforts.

## VI

### SUMMARY AND CONCLUSION

The experimental results reported here have been concerned with two rather distinct areas of investigation. The initial motivation for studying the shock reflection process and the time history of thermodynamic properties in the reflected shock region was provided by the need to know the free stream properties at the edge of the end-wall boundary layer. The boundary layer studies were performed for both an ionized and un-ionized free stream. The results for the latter case were found to agree very well with theory based on the assumption that the thermal conductivity for atomic argon is proportional to the local temperature raised to the  $3/4$  power.

The application of two-wavelength time-resolved interferometry as a diagnostic tool provided a quantitative measure of the equilibrium mass density and electron concentration in the reflected shock region. These results were found to be systematically higher than those predicted by "quasi-steady" reflected shock theory, i. e. , constant reflected shock speed, in conjunction with a modified Saha Equation. When no ionization took place, the thermodynamic properties were found to be in excellent agreement with simple perfect gas theory. Radiation cooling was found to have a significant effect on the properties for times on the order of  $10^{-8}$  s of microseconds as shown in figure 35. The interferograms also provided an informative visualization of the shock reflection process, and a significant portion of this report was devoted to interpreting the observed non-equilibrium wave interactions resulting from the onset of ionization.

The nature of the shock reflection process in ionizing argon was discussed in terms of  $x-t$  diagrams which showed the trajectories of the incident and reflected shocks along with the associated ionization fronts. It was found that the initial reflected shock speed is less than that predicted by perfect gas calculations, and that there are a significant number of electrons immediately behind

the frozen reflected shock. The reflected shock is further decelerated when it is overtaken by an expansion wave originating at the onset of equilibrium at the end-wall. The incident shock ionization front was seen to be transmitted through the reflected shock as an "interaction pressure wave" which propagates to the end-wall; whereupon it is also reflected. The reflected interaction wave then overtakes and coalesces with the transmitted reflected shock. The interferograms also show clearly the existence of contact surfaces separating regions of the flow field where the gas has been processed by different entropy producing shock waves. For the stronger incident shocks, the reflected shock region appears to be non-uniform after the interactions are complete, as exhibited by a waviness in the interference fringes. It was postulated that these non-uniformities were partially caused by the occurrence of reflected shock bifurcation and the associated separation of the incident shock side-wall boundary layer. The unexpected presence of bifurcation in argon was found to be associated with the onset of ionization behind both the incident and reflected shocks. A few rotating mirror interferograms were taken for gases other than argon for purposes of comparison, and it was found that the reflected shock structure in xenon is basically similar to that in argon.

Knowing the free stream conditions from the streak interferograms, the ionized end-wall boundary layer was studied in a manner similar to that used for the un-ionized boundary layer. The results for the ionized boundary layer were then compared with the theoretical analysis of Knöös<sup>(12)</sup>. The experimentally determined electron concentrations in the boundary layer for each of three initial pressures were found to fall off less rapidly from the freestream values than the theory predicted. The theoretical analysis assumes complete thermodynamic and chemical equilibrium in the boundary layer as well as constant freestream properties. However, it was shown that the criteria for the existence of these conditions were not satisfied and that nonequilibrium effects are probably the main reason for the observed discrepancy. It was also noted that failure of the theory to account for radiation absorption in the boundary layer may contribute

to the disagreement. No attempt was made to correlate the transport properties for the ionized boundary layer because of the apparent inapplicability of the present theories.

The experimental investigation reported here has provided a considerable amount of data which may provide the basis for future theoretical efforts. In particular, a flow field analysis of the reflected shock region in conjunction with the streak interferograms would yield additional information on the rate processes leading to ionization equilibrium. The basic techniques used here may also be applied to the detailed study of more complicated gases. Perhaps of greater interest would be the construction of a more realistic ionized, boundary-layer theory which would account for the above mentioned nonequilibrium effects. Such an analysis would then allow a comparison of theory and experiment to evaluate the transport properties of an argon plasma.

## REFERENCES

1. M. Camac and R. M. Feinberg, "Thermal Conductivity of Argon at High Temperatures," Avco-Everett Research Report 168 (1963).
2. J. A. Smith, "An Experimental Investigation of the Structure of Reflecting, Ionizing Shocks in Xenon," Ph. D. Thesis, Calif. Inst. of Tech. (1967).
3. D. Baganoff, "Experiments on the Wall Pressure History in Shock Reflection Processes," J. Fluid Mech. , 23, 209 (1965).
4. H. E. Petschek and S. Byron, "Approach to Equilibrium Ionization Behind Strong Shock Waves in Argon," Annals of Physics 1, 270 (1957).
5. H. Wong and D. Bershader, "Thermal Equilibration Behind an Ionizing Shock," J. of Fluid Mech. 26, 459 (1966).
6. K. E. Harwell and R. G. Jahn, "Initial Ionization Rates in Shock-Heated Argon, Krypton, and Xenon," Physics of Fluids 7, 214 (1964).
7. V. Blackman, "Vibrational Relaxation in Oxygen and Nitrogen," J. of Fluid Mech. 1, 61 (1956).
8. N. H. Johannesen, G. A. Bird and H. K. Zienkiewicz, "Theoretical and Experimental Investigations of the Reflexion of Normal Shock Waves With Vibrational Relaxation," J. of Fluid Mech. 30, 51 (1967).
9. S. Byron and N. Rott, "On the Interaction of the Reflected Shock Wave With the Laminar Boundary Layer on the Shock Tube Side Walls," Proceedings 1961 Heat Trans. and Fluid Mech. Inst.
10. J. O. Bunting and R. S. Devoto, "Shock Tube Study of the Thermal Conductivity of Argon," SUDAAR No. 313, Dept. of Aero. and Astro., Stanford Univ. (1967).
11. I. Amdur and E. A. Mason, "Properties of Gases at Very High Temperatures," Phys. of Fluids 1, 370 (1958).
12. S. Knöös, "Analysis of Boundary Layer Structure in a Shock Generated Plasma Flow," SUDAAR No. 277, Stanford Univ. (1966).
13. J. N. Bradley, Shock Waves In Chemistry and Physics, J. Wiley and Sons, Inc., N. Y., 1962.
14. A. G. Gaydon and I. R. Hurle, Shock Tube In High Temperature Physics, Reinhold Pub. Corp., N. Y., 1963.
15. R. Ladenburg and D. Bershader, "Physical Measurements in High Speed Aerodynamics and Combustion," Vol. IX Princeton Series.
16. D. W. Holder, R. J. North, and G. P. Wood, "Optical Methods for Examining Flow in High Speed Wind Tunnels," AGARDograph No. 23 (1956).

17. W. L. Howes and D. R. Buchele, "Practical Considerations of Gas Flow Interferometry," NACA TN 3507 (1955).
18. R. A. Alpher and D. R. White, "Optical Refractivity of High Temperature Gases. II Effects Resulting from Ionization of Monatomic Gases," *Phys. of Fluids* 2, 162 (1959).
19. G. P. Wachtell, "Refraction Error in Interferometry of Boundary Layers in Flow Along a Flat Plate," Ph.D. Thesis, Princeton University (1951) (Abstract, *Phys. Rev.* 78, 333 (1950).
20. W. L. Howes and D. R. Buchele, "Optical Interferometry of Inhomogeneous Gases," *J. of Opt. Soc. of Am.*, 56, 1517 (1966).
21. S. Chapman and T. G. Colwing, The Mathematical Theory of Non-Uniform Gases, Cambridge Press (1964).
22. J. A. Fay and N. H. Kemp, "Theory of End Wall Heat Transfer in Monatomic Gases Including Ionization Effects," Avco-Everett Res. Rep. 166 (1963).
23. R. E. Duff, "Shock Tube Performance at Low Initial Pressures," *Phys. of Fluids* 2, 207, (1959).
24. H. Mirels, "Flow Nonuniformity in Shock Tubes Operating at Maximum Test Times," *Phys. of Fluids* 9, 1907 (1966).
25. B. Sturtevant and E. Slachmuylders, "End Wall Heat Transfer Effects on the Trajectory of a Reflected Shock Wave," *Phys. of Fluids* 7, 1201 (1964).
26. D. J. Collins and W. A. Mennard, "Measurement of the Thermal Conductivity of Noble Gases in the Temperature Range 1500 to 5000 Deg. Kelvin," *Jour. of Heat Trans.* 88, 52 (1966).
27. F. A. Jenkins and H. E. White, Fundamentals of Optics, McGraw-Hill (1957).
28. Progress Report on Experimental and Analytic Studies of Plasma Transport Properties, Department of Aeronautics and Astronautics, Stanford University, June 1967.
29. H. Mark, "The Interaction of a Reflected Shock Wave with the Boundary Layer in a Shock Tube," NACA TM 1418 (1958).
30. R. A. Strehlow and A. Cohen, "Limitations of the Reflected Shock Technique for Studying Fast Chemical Reactions and Its Application to the Observation of Relaxation in  $N_2$  and  $O_2$ ," *J. Chem. Phys.* 30, 257 (1959).
31. M. Camac and N. H. Kemp, "A Multitemperature Boundary Layer," Avco-Everett, RR-184 (1964).
32. R. S. Devoto, "Transport Coefficients of Partially Ionized Argon," *Phys. of Fluids*, 10, 354 (1967).

33. W. F. Ahtye, "A Critical Evaluation of Methods for Calculating Transport Coefficients of Partially and Fully Ionized Gases," NASA TN D-2611 (1965).
34. C. F. Knopp and A. B. Cambel, "Experimental and Theoretical Determination of Atmospheric Argon Plasma," Phys. of Fluids 9, 989 (1966).
35. H. Griem, Plasma Spectroscopy, McGraw Hill, (1964).
36. D. P. Duclos and A. B. Cambel, "The Equation of State of an Ionized Gas," Prog. in International Res. on Thermo. and Trans. Prop., J. F. Masi and D. H. Tsai (ed.) Academic Press (1962).
37. J. Cooper, (Editor), Proceedings of the Workshop Conference on the Lowering of the Ionization Potential and Related Problems of the Equilibrium Plasma," JILA Report No. 79, Univ. of Colorado (1965).
38. G. Ecker and W. Kroll, "Lowering of the Ionization Energy for a Plasma in Thermodynamic Equilibrium," Phys. of Fluids 6, 62 (1962).

EFFECT OF REFRACTION AND WINDOW BOUNDARY LAYER ON  
INTERFEROMETRIC MEASUREMENTS
$$\frac{1}{R} = \frac{1}{\mu} |\text{grad } \mu| \sin \theta$$

where  $R$  is the radius of curvature of the light ray,  $\mu$  is the index of refraction in the medium, and  $\Theta$  is the angle between the tangent to the trajectory and  $\text{grad } \mu$ . Now consider the following figure appropriate to the conditions in the end-wall boundary-layer studies.





This figure, which is a vertical view of the test section, illustrates that because the density increases and, if ionized, the electron concentration decreases as  $y$  approaches zero, the refractivity,  $(\mu - 1)$ , will increase in the same direction and cause the light ray to bend toward the wall. For a two-dimensional problem such as this, the above equation for the light ray EF becomes

$$\frac{y''}{1 + y'^2} = \frac{1}{\mu} \frac{d\mu}{dy} = f[y(x)] \quad \text{A.2}$$

where the primes indicate differentiation with respect to  $x$ . This equation can be solved numerically for a known boundary-layer profile since we know the relationship between  $\mu$  and  $\rho$  and  $n_e$  from equation 2.4. In particular for each of the two wavelengths in an argon plasma

$$(\mu - 1)_1 = .160 \rho_\infty \left[ \frac{\rho}{\rho_\infty} - 5.95(10^{-22}) \frac{n_e}{\rho_\infty} \right] ; \lambda_1 = 4530 \text{ \AA} \quad \text{A.3}$$

$$(\mu - 1)_2 = .159 \rho_\infty \left[ \frac{\rho}{\rho_\infty} - 9.45(10^{-22}) \frac{n_e}{\rho_\infty} \right] ; \lambda_2 = 5720 \text{ \AA}$$

It is also useful for the following material to integrate equation A.2 once to obtain

$$\frac{\mu}{\mu_E} = \sqrt{1 + y'^2} \quad \text{A.4}$$

where use has been made of the boundary conditions

$$\begin{aligned} \mu &= \mu_E \\ y' &= 0 \end{aligned} \quad \text{at } y = y_E, x = 0$$

In this analysis we are interested in the magnitude of the difference in what the fringe shift would be if no refraction were present and what the theoretical measured fringe shift would be for the same theoretical boundary layer profile. To do this we choose to compute each of these separately and subtract the theoretical measured values with refraction from the theoretical values with no refraction.

Consider the following optical path lengths

$$\psi_{1,2} = \int_{\text{light source}}^{\bar{Q}} \mu ds \quad \text{A. 5}$$

where  $ds$  is the elemental geometric path length and the subscripts 1 and 2 refer to integration from the source to the same point  $\bar{Q}$  in the image plane through the interferometer test beam and compensating beam respectively.

Then if the coordinate in the image plane is denoted by  $\bar{y}$ , one can see from the principle of interference that interference fringes of order  $N$  will be formed in the image plane at points where the difference  $\psi_1 - \psi_2$  is equal to  $N$  vacuum wavelengths of this incident light. That is, the fringe distribution is given by

$$N(\bar{y}) = \frac{1}{\lambda_0} [\psi_1(\bar{y}) - \psi_2(\bar{y})] \quad \text{A. 6}$$

Now, if an inhomogeneity in refractivity exists in some region of the field of view, a new distribution of fringe order will result. Denoting the new distribution by  $N(\bar{y})$  and the original undisturbed distribution by  $N^0(\bar{y})$ , we can write for the so called "fringe shift" or change in the order of interference at a particular point  $\bar{Q}$

$$S(\bar{Q}) = N(\bar{Q}) - N^0(\bar{Q})$$

For a particular point  $\bar{Q}$  in the image plane, the optical path through the compensating beam is the same as before the disturbance so we can write

$$\begin{aligned} S(\bar{Q}) &= \frac{1}{\lambda_0} \left\{ [\psi_1(\bar{Q}) - \psi_2(\bar{Q})] - [\psi_1^0(\bar{Q}) - \psi_2(\bar{Q})] \right\} \\ &= \frac{1}{\lambda_0} [\psi_1(\bar{Q}) - \psi_1^0(\bar{Q})] \end{aligned} \quad \text{A. 7}$$

If no consideration is given to refraction, this reduces to the familiar

$$S(\bar{Q}) = \frac{L}{\lambda_0} \left\{ [\mu(\bar{Q}) - 1] - [\mu_\infty - 1] \right\} \quad \text{A. 8}$$

since the only difference in optical path length occurs within the test section width,  $L$ , and where  $(\mu_\infty - 1)$  is the refractivity of the reference conditions in the free stream.

Referring to figure A.1, it can be seen that when refraction is accounted for, the light ray through the test section that arrives at the point

$\bar{Q}$  appears to come from  $Q$  in the object plane, which for this analysis is located at  $h = L/3 = \frac{50}{3}$  mm. The fringe shift that will be measured at  $\bar{Q}$  is thus given by

$$S_M(\bar{Q}) = \frac{1}{\lambda_0} [\psi_{SEFG\bar{Q}} - \psi_{SABC\bar{Q}}^0]$$

By assuming an on axis point light source and perfect optics, the wave fronts entering the test section are plane and parallel to the entrance window so that

$$S_M(\bar{Q}) = \frac{1}{\lambda_0} [\psi_{EFG\bar{Q}} - \psi_{ABC\bar{Q}}^0]$$

A.9

$$= \frac{1}{\lambda_0} [(\psi_{EF} - \psi_{AB}^0) + (\psi_{FG} - \psi_{BC}^0) + (\psi_{G\bar{Q}} - \psi_{C\bar{Q}}^0)]$$

For the first term in equation A.9, we have

$$\psi_{EF} - \psi_{AB}^0 = \int_0^L \mu(y) \sqrt{1 + y'^2} dx - \mu_0 L$$

A.10

$$= \mu_E \int_0^L (1 + y'^2) dx - \mu_0 L$$

where use has been made of equation A.4. The integral is evaluated from the solution of equation A.2 for the assumed theoretical boundary layer profile.

The second term of A.9 is expressible as

$$\psi_{FG} - \psi_{BC}^{\circ} = \mu_g [FG - BC]$$

$$= \mu_g \left[ \frac{t}{\cos \varphi_2} - t \right]$$

$$= \mu_g t \left\{ \left[ 1 - \left( \frac{\mu_F}{\mu_g} \right)^2 \frac{y_F'^2}{1 + y_F'^2} \right]^{-1/2} - 1 \right\} \quad \text{A. 11}$$

$$= \mu_g t \left\{ \left[ 1 - \left( \frac{\mu_E}{\mu_g} \right)^2 y_F'^2 \right]^{-1/2} - 1 \right\}$$

where use has been made of the geometry in figure A. 1, Snell's law of refraction, and equation A.4. The value of  $y_F'$  is obtained from the solution of A.2. Several authors have considered that special problems arise in refraction analyses when the test section light is transmitted through and not reflected from the last beamsplitter of the interferometer. This latter arrangement is, of course, more desirable than the former which is the way the present interferometer is arranged. However, it appears that in this case where the plane of centers for the interferometer is perpendicular to the refractive gradient, the effect of the beam splitter is simply to make the effective exit window thickness  $t$  larger. Therefore, in the actual calculations,  $t'$

is substituted for  $t$  where

$$t' = t_{\text{window}} + \frac{t_{\text{beam splitter}}}{\sin(45^\circ)}$$

To determine the last term in equation A.9, one notes that a backward extrapolation of  $G\bar{Q}$  appears to come from the apparent object point  $Q^*$ . Therefore, again by Fermat's principle, if the windows and test section are removed, rays emanating in any direction from  $Q^*$  have equal optical path lengths to the conjugate point  $\bar{Q}$ , so that

$$\mu_a \cdot (Q^*G) + \psi_{G\bar{Q}} = \mu_a(Q^*C) + \psi_{C\bar{Q}}^o$$

or

$$\psi_{G\bar{Q}} - \psi_{C\bar{Q}}^o = \mu_a [Q^*C - Q^*G]$$

Noting that

$$CG = (h^* + t) \tan \varphi_1$$

$$= (h^* + t) \tan \varphi_3$$

$$= h \tan \epsilon + t \tan \varphi_2$$

or

$$Q^*C = h^* + t$$

$$= h \frac{\tan \epsilon}{\tan \varphi_3} + t \frac{\tan \varphi_2}{\tan \varphi_3}$$

and

$$Q^*G = \frac{Q^*C}{\cos \varphi_1} = \frac{Q^*C}{\cos \varphi_3}$$

where the following relations apply

$$\tan \epsilon = y'_F$$

$$\tan \varphi_2 = \frac{\mu_E}{\mu_g} \frac{y'_F}{\left[1 - \left(\frac{\mu_E}{\mu_g}\right)^2 y'^2_F\right]^{1/2}}$$

$$\tan \varphi_3 = \frac{\mu_E}{\mu_a} \frac{y'_F}{\left[1 - \left(\frac{\mu_E}{\mu_a}\right)^2 y'^2_F\right]^{1/2}}$$

Where again use has been made of the geometry and equation A.4. Finally, we can write for the third term

$$\psi_{G\bar{Q}} - \psi_{C\bar{Q}}^0 = \frac{\mu_a^2}{\mu_E} \left\{ h + \frac{t \left( \frac{\mu_E}{\mu_g} \right)}{\left[ 1 - \left( \frac{\mu_E}{\mu_g} \right)^2 y_F'^2 \right]^{1/2}} \right\} \left\{ \left[ 1 - \left( \frac{\mu_E}{\mu_a} \right)^2 y_F'^2 \right]^{1/2} - 1 \right\}$$

A.12

With the solution to equation A.2 known and equations A.10, A.11, and A.12 substituted into A.9, we can calculate the fringe shift,  $S_M$ , that would be measured at  $\bar{Q}$  corresponding to the point Q in the test section for the assumed boundary layer profile. It remains only to determine the value of  $y_Q$  which can be written

$$\begin{aligned} y_Q &= y_E - D \\ &= y_E - [(y_E - y_F) - h \tan \epsilon] \\ &= y_F + h \cdot |y_F'| \end{aligned}$$

A.13

The theoretical boundary layer profiles assumed in this analysis were the solutions to equation 3.4 for  $\mathcal{V} = .75$  and the un-ionized free stream conditions corresponding to run 714 and those resulting from the solution of the equations presented in Chapter IV for the ionized boundary layer. Equation A.2 was solved for these profiles by use of a Runge-Kutta procedure, and the integral of equation A.10 was performed by Simpson's rule on an IBM 360-67



computer. The results of the analysis are presented for two cases, typical of the un-ionized and ionized boundary layer, in figure 41. The fringe shift profile for no refraction  $S$  (equation A. 8) is plotted along with the "error"  $S-S_M$  where again,  $S_M$  is the fringe shift profile one would actually measure if the "true" boundary layer profile were given by the above solutions.

4.2 Window Boundary Layer. In the presence of side-wall boundary layers on the test section windows, the actual measured fringe shift will be given by (no refraction since refractivity gradients are parallel to the optical axis)

$$S = \frac{1}{\lambda} \int_0^L [\mu(x) - 1] dx - \frac{L}{\lambda} \left[ \frac{(\mu-1)_0}{\rho_0} \right] \rho_1$$

A. 14

$$= \frac{L}{\lambda} \left\{ (\mu-1) - \left[ \frac{(\mu_0-1)}{\rho_0} \right] \rho_1 \right\} - \frac{2\delta}{\lambda} (\mu-1) + \frac{2}{\lambda} \int_0^\delta (\mu-1)_{B.L.} dx$$

In this equation no subscript refers to the true test section properties and the subscripts 1 and B. L. refer to the reference conditions and the boundary layer properties respectively. The boundary layer thickness is given by  $\delta$ . From equation A.3 we can write

$$(\mu-1) = A(\lambda) \rho_1 \left[ \frac{\rho}{\rho_1} - \frac{n_e}{\rho_1} B(\lambda) \right] \quad A. 15$$

If one neglects the effects of the side wall boundary layer, the indicated test section properties denoted by the primed quantities will be related to the measured fringe shift by

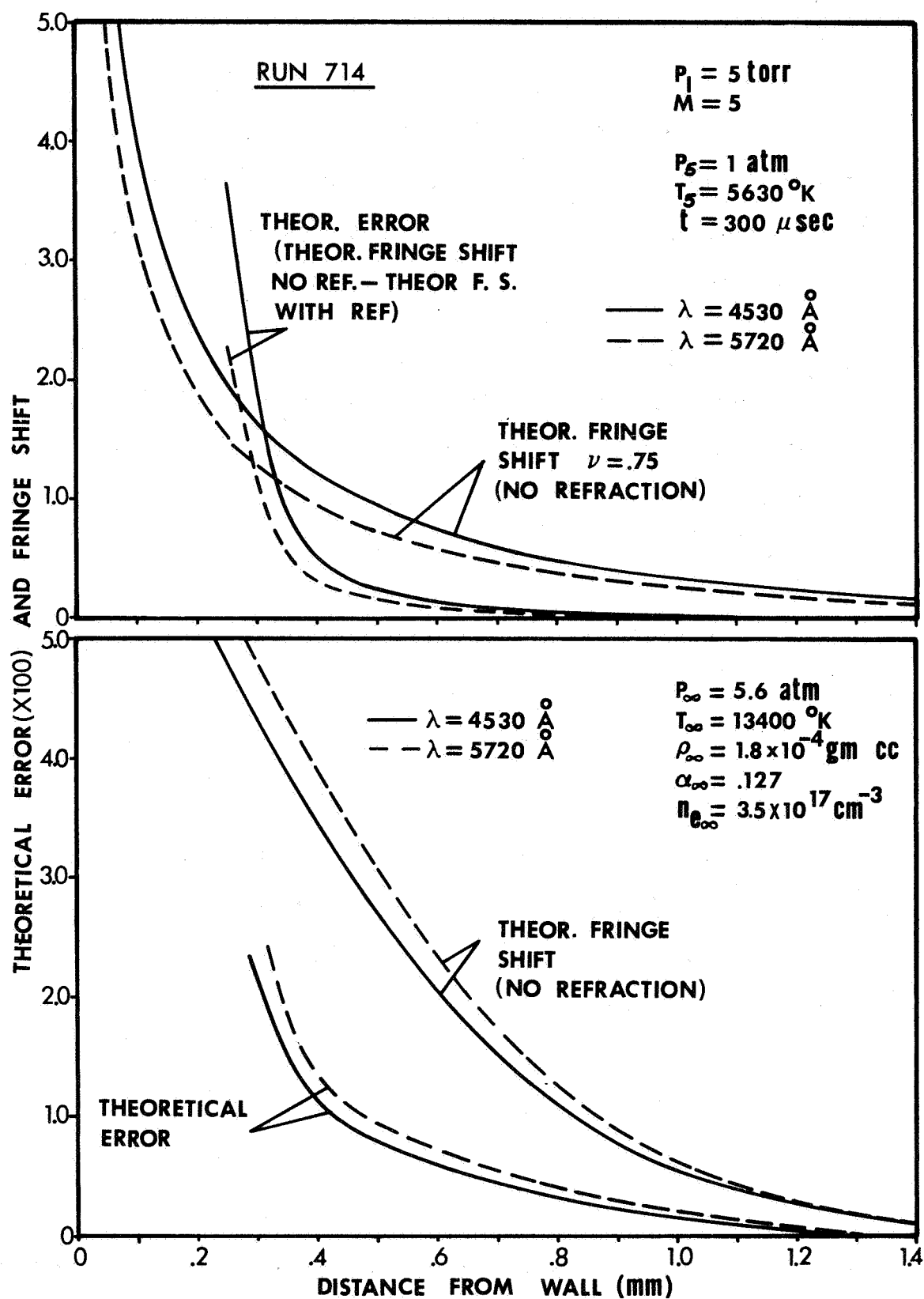


Figure 41. Theoretical fringe shift error in end-wall boundary layer measurements.

$$S = \frac{L}{\lambda} A(\lambda) \rho_1 \left[ \left( \frac{\rho'}{\rho_1} \right) - \frac{n'_e}{\rho_1} B(\lambda) \right] \quad \text{A.16}$$

Substituting equation A.15 into A.14 and equating the result to A.16 for each of two wavelengths results in

$$(\rho' - \rho) + B_{1,2}(n_e - n'_e) = -\frac{2\delta}{L} [\rho - B_{1,2} n_e] + \frac{2}{L} \int_0^\delta (\rho_{B.L.} - B_{1,2} n_{eB.L.}) dx$$

Subtracting these two equations and letting

$$n_{eB.L.} = r_1(x) n_e$$

$$\rho_{B.L.} = r_2(x) \rho$$

we have

$$\frac{n_e}{n'_e} = \left[ 1 - \frac{2\delta}{L} + \frac{2}{L} \int_0^\delta r_1(x) dx \right]$$

$$\frac{\rho}{\rho'} = \frac{1 + B_1 \frac{n'_e}{\rho'} \left[ \frac{n_e}{n'_e} \left( 1 - \frac{2\delta}{L} \right) - 1 + \frac{2}{L} \frac{n_e}{n'_e} \int_0^\delta r_1(x) dx \right]}{\left[ 1 - \frac{2\delta}{L} - \frac{2}{L} \int_0^\delta r_2(x) dx \right]}$$

Now if one assumes a parabolic boundary layer as follows

$$r_1(x) = \left(\frac{x}{\delta}\right) \left[2 - \left(\frac{x}{\delta}\right)\right]$$

$$r_2(x) \cong \left(\frac{T}{T_w} - 1\right) \left[1 - 2\left(\frac{x}{\delta}\right) + \left(\frac{x}{\delta}\right)^2\right] + 1$$

where  $T_w$  is the wall temperature and where the reasonable assumption has been made  $\rho/\rho_w \cong T/T_w$ . The above ratios of true to indicated properties become

$$\frac{n_e}{n'_e} = \left[1 - \frac{2}{3}\left(\frac{\delta}{L}\right)\right]^{-1}$$

and

$$\frac{\rho}{\rho'} = \frac{1 - \frac{B_1 n'_e}{\rho'} \left[1 - \left(\frac{n_e}{n'_e}\right) \left(1 - \frac{2}{3} \frac{\delta}{L}\right)\right]}{\left[1 + \frac{2}{3} \frac{\delta}{L} \left(\frac{T}{T_w} - 1\right)\right]}$$

These equations clearly indicate the expected results that the measured or indicated  $n_e$  and  $\rho$  are respectively too low and too high.

If one assumes a boundary layer thickness of 1 mm and the indicated conditions at 100  $\mu$ sec after reflection for  $P_1 = 5$  mm,  $M = 12.0$ , the resulting errors are  $n_e/n'_e \sim 1.02$  and  $\rho/\rho' \sim .80$ . While the error in the measured electron concentration is negligible, the error in density is quite

large. However, the above assumption regarding the density ratio,  $\rho/\rho_w$  was conservative as was the parabolic distribution assumption for the boundary layer profile, so the actual errors are somewhat less than this. As discussed in Chapter IV, this source of error was not actually accounted for in reducing the data because of the unknown effects of bifurcation and side-wall, boundary-layer developments.

The direct effects of the side-wall boundary-layer on the end-wall, thermal-layer measurements were estimated by Bunting<sup>(10)</sup> and found to be negligible relative to the uncertainty in fringe shift measurement; therefore, no additional calculations will be done here.

## APPENDIX B

### CALCULATION OF REFLECTED SHOCK EQUILIBRIUM PROPERTIES

The analysis described here for the calculation of the equilibrium, thermodynamic properties behind the reflected shock corresponding to frozen conditions behind the incident shock is unrealistic in view of the results of Chapter IV. The basic procedure, however, is typical of the kind of calculations that have often been relied on to provide the boundary conditions for other end-wall experiments and similarly, were first performed in this investigation to provide an estimate of the expected properties as a function of the initial conditions. An exact solution or one more closely matching the actual flow field was not undertaken here, although such a study in connection with the present data might well yield valuable information on the kinetic rate processes, which would obviously have to be included.

The analysis proceeds by assuming a constant reflected shock speed of sufficient strength to bring the fluid behind it to rest. The conservation equations then yield the following jump conditions:

$$u_{F5E} = \left[ \frac{\eta_{2F} - 1}{\gamma_{5E} - \eta_{2F}} \right] u_S$$

$$\frac{p_{5E}}{p_1} = 1 + \gamma_1 M_S^2 \frac{(\eta_{2F} - 1)(\gamma_{5E} - 1)}{(\gamma_{5E} - \eta_{2F})} \quad \text{B. 1}$$

$$\frac{h_{5E}}{h_1} = 1 + (\gamma - 1) M_S^2 \frac{(\eta_{2F} - 1)(\gamma_{5E} - 1)}{\eta_{2F} (\gamma_{5E} - \eta_{2F})}$$

where the density ratio,  $\eta_{2F}$ , is given by  $\eta_{2F} = \rho_{2F} / \rho_1$  and where  $\gamma_{5E} = \rho_{5E} / \rho_1$ . It is assumed that no reactions are taking place behind the incident shock. Since only the initial pressure, enthalpy, shock speed, and ratio of specific heats are known, two more equations are necessary to determine the five unknowns,  $P_{5E}$ ,  $h_{5E}$ ,  $U_{F5E}$ ,  $\eta_{2F}$  and  $\gamma_{5E}$ . These can be provided by the specification of a thermal and caloric equation of state. However, such a specification introduces two additional unknowns, namely, the temperature and degree of ionization. A determinate system is then obtained by introducing the Saha equation expressing the relationship between the temperature, density, and degree of ionization when the fluid is in thermodynamic equilibrium and all species are at one temperature.

The thermal and caloric equations of state are taken as

$$P_{5E} = (1 + \alpha_{5E}) \gamma_{5E} \rho_1 R_A T_{5E} - \Delta P \quad B.2$$

and

$$h_{5E} = \frac{P_{5E}}{\rho_1 \gamma_{5E}} + e_{trans} + e_{ioniz.} + e_{elec. exc.} \quad B.3$$

The pressure correction term arises because of the coulomb interactions in the plasma and is given by

$$\begin{aligned} \Delta P &= \frac{e^3}{24\pi \epsilon_0^{3/2} K^{1/2} m_A^{3/2}} \frac{(2\alpha_{5E})^{3/2} (\rho_1 \gamma_{5E})^{3/2}}{T_{5E}^{1/2}} \\ &= \frac{\alpha_{5E} (\rho_1 \gamma_{5E})}{3} \Delta I \end{aligned} \quad B.4$$

where  $\Delta I$  is the Debye-Hückel correction to the ionization potential given by

$$\Delta I = \frac{e^3 (2\alpha_{5E})^{1/2} (\rho_1 \gamma_{5E})^{1/2}}{4\pi \epsilon_0^{3/2} (m_A k T_{5E})^{1/2}} \quad \text{B. 5}$$

These corrections to the plasma properties result from a consideration of the coulomb or polarization energy released to the plasma through the tendency of the charged particles to surround a particle of unlike charge. Such a "space charge" effect occurs over distances on the order of a Debye length and the energy that would have been required to ionize the particle is essentially decreased by the potential energy stored in these field effects. The derivation of the above expressions gives rise to its own validity criterion, namely, that the following inequality be satisfied<sup>(36)</sup>

$$n_e \leq \frac{1}{2\pi} \left( \frac{\epsilon_0 k T}{e^2} \right)^3$$

For  $kT \sim 1 \text{ eV}$  this reduces to  $n_e \leq 10^{20} \text{ cm}^{-3}$ , which is obviously satisfied for the present experimental conditions. A considerable body of literature has been published on the subject of potential lowering and the somewhat related problem of truncating the classically divergent electronic partition functions. (See for example reference 37.) Unfortunately, no new insight is provided in this report since the details of the plasma equations and the experimental results are somewhat clouded by their coupling to the rather complicated flow field behind the reflected shock. As a matter of interest, however, the calculations for the reflected shock properties were performed with no plasma corrections, with the above Debye-Hückel theory, and with the following correction of Ecker and Weizel<sup>(38)</sup>



$$\Delta I = .264(10^{-10})(\alpha_{5E} \rho_1 \gamma_{5E})^{1/3} + .725(10^{-8}) \frac{(\alpha_{5E} \rho_1 \gamma_{5E})^{1/2}}{T_{5E}^{1/2}} \quad \text{B.6}$$

(erg)

In using this expression, no pressure correction was included in the calculations. The results, given later in this appendix, show that greatest differences from no potential lowering result from the Ecker-Weizel formulation, as expected.

Before returning to equation B.3, it is noted that the form of the Saha equation used in the analysis is

$$\frac{\alpha^2}{1-\alpha} = m_A \left( \frac{2\pi m_e k}{h^2} \right)^{3/2} \frac{2T^{3/2} [4 + 2\exp(-\frac{2062}{T})]}{\rho} \exp\left[-\frac{(I-\Delta I)}{KT}\right] \quad \text{B.7}$$

where all units are consistent and  $I = 15.75$  ev. It should be apparent to the reader that only the low lying levels of the argon ion are being considered in the electronic partition functions. Therefore, it is a simple matter to show that equation B.3 may be written

$$h_{5E} = \frac{P_{5E}}{\rho_1 \gamma_{5E}} + \left\{ \frac{3}{2} (1 + \alpha_{5E}) R_A T_{5E} \right\} + \left\{ \frac{\alpha_{5E}}{m_A} (I - \Delta I) \right\}$$

B.8

$$+ \left\{ \frac{\alpha_{5E} R_A T_{5E} 4124 \exp(-\frac{2062}{T_{5E}})}{4 + 2 \exp(-\frac{2062}{T_{5E}})} \right\} \quad \left( \frac{\text{erg}}{\text{gm}} \right)$$

Equations B.1, B.2, B.4, B.5, B.7, and B.8 now form a determinate system of equations for the unknowns when the simple jump conditions across

the incident shock for a perfect gas are included. The equations are obviously transcendental and must be solved by an iterative approach. To simplify the numerical calculations, the inverse problem was solved; that is, an initial pressure  $P_1$  and temperature  $T_1$  and final temperature  $T_{5E}$  were specified. A value of  $\mathcal{P}_{5E} = P_{5E}/P_1$  was then guessed as a trial value which subsequently yielded a value for  $\alpha_{5E}$  from an iterative solution of the Saha equation (Newton-Raphson technique). Substituting  $P_1$ ,  $\alpha_{5E}$  and  $T_{5E}$  into an algebraic solution for  $\mathcal{P}_{5E}$  obtained from the remaining equations yields a new value of  $\mathcal{P}_{5E}$  which is then compared with the trial guess. This procedure was repeated until the change in  $\mathcal{P}_{5E}$  over the previous trial was less than .0001.

These calculations were repeated for a range of temperatures and initial pressures and the results plotted as shown in figures 42 and 43 where the equilibrium temperatures and electron concentrations are given as a function of incident shock Mach number. It can be seen by a comparison of figure 43 with figure 28 that even the Ecker-Weizel ionization potential lowering does not achieve agreement of the present "quasi-steady" theory with experiment. Figure 43 shows an increase of approximately 10% in the electron concentration for the Ecker-Weizel correction over no potential lowering. The difference for the Debye-Hückel theory is somewhat less than this. It is also interesting to note that the coulomb energy correction in equation B.8 is less than .01 of the total internal energy of the argon plasma for the range of conditions displayed here.

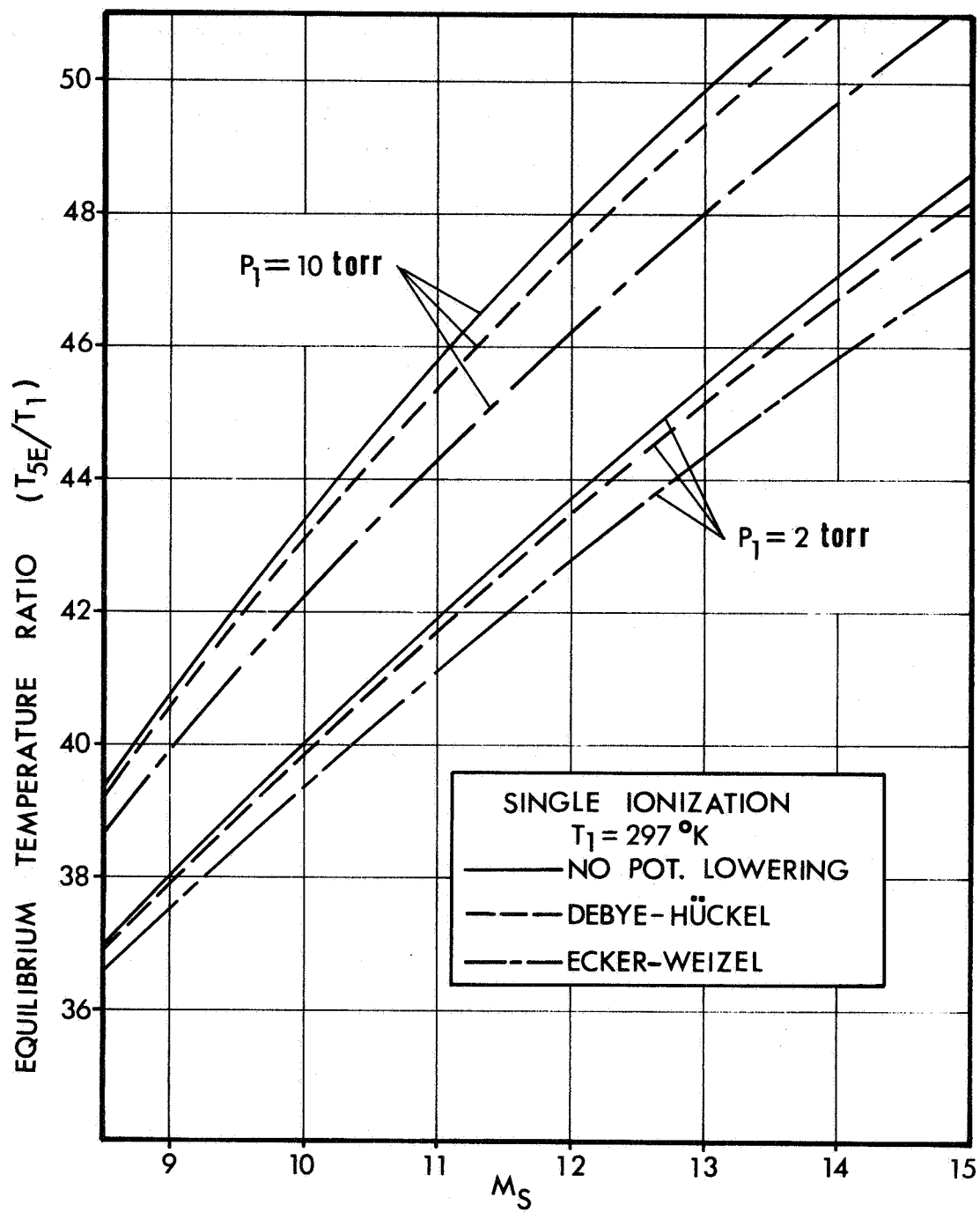


Figure 42. Equilibrium reflected shock temperature ratios from "quasi-steady" theory using various corrections to ionization potential (argon).

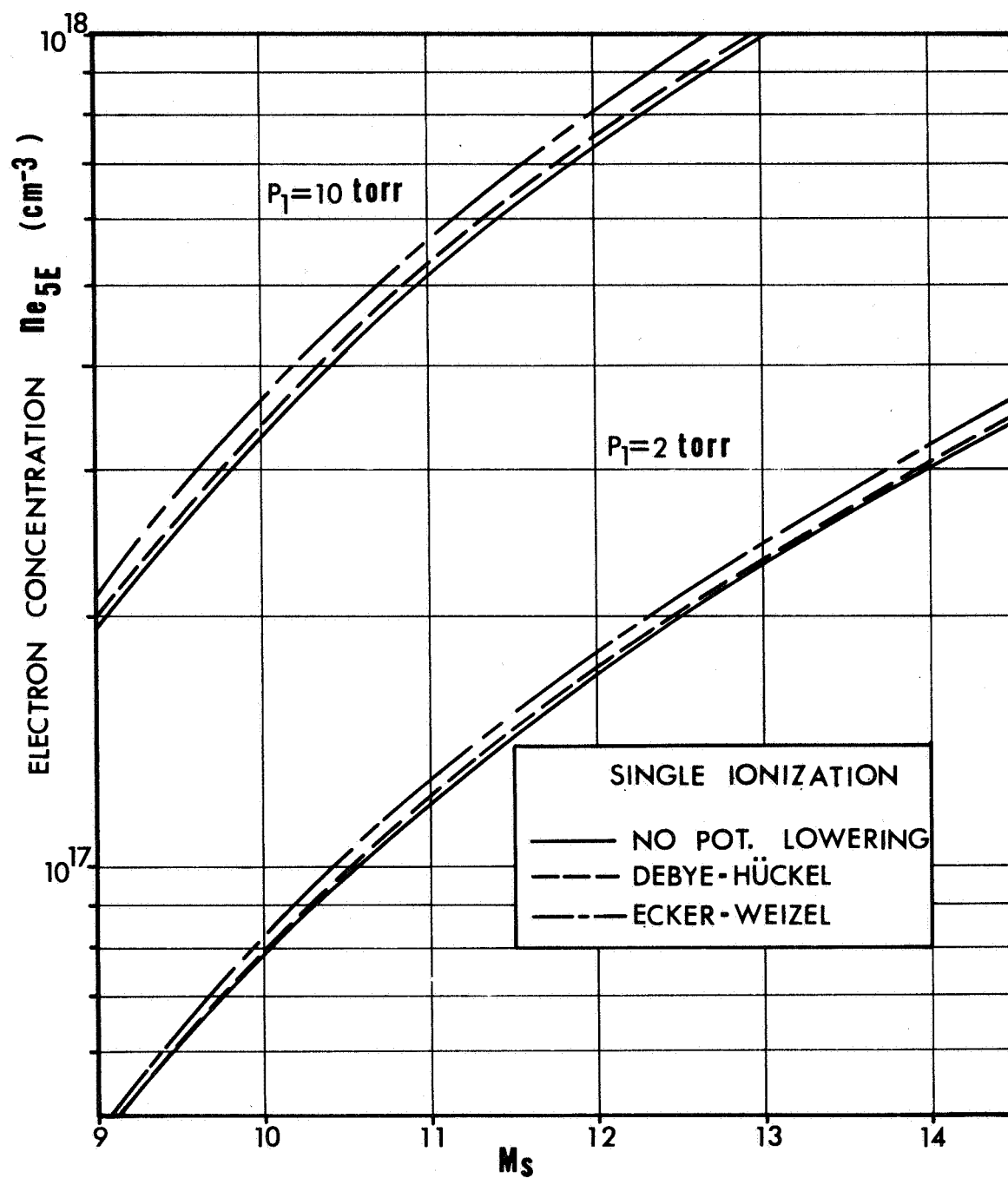


Figure 43. Equilibrium reflected shock electron concentrations from "quasi-steady" theory using various corrections to ionization potential (argon).